

12

LEVEL II

90

AFGL-TR-81-0207
ENVIRONMENTAL RESEARCH PAPERS, NO. 748



AD A109928

Atmospheric Infrared Radiance Variability

Editors
C. H. HUMPHREY
R. M. NADILE
C. R. PHILBRICK
D. R. SMITH

DTIC
SELECTED
JAN 22 1982
S D
B

27 May 1981

This research was partially supported by the Air Force In-House
Laboratory Independent Research Fund

Approved for public release; distribution unlimited.

OPTICAL PHYSICS DIVISION PROJECT 2310
AIR FORCE GEOPHYSICS LABORATORY
HANSCOM AFB, MASSACHUSETTS 01731

AIR FORCE SYSTEMS COMMAND, USAF



0120 82059

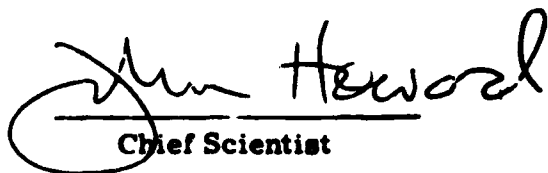
DTIC FILE COPY

1/81

This report has been reviewed by the ESD Public Affairs Office (PA)
and is releasable to the National Technical Information Service (NTIS).

This technical report has been reviewed and
is approved for publication.

FOR THE COMMANDER


Chief Scientist

Qualified requestors may obtain additional copies from the
Defense Technical Information Center. All others should apply to the
National Technical Information Service.

97-11-1948

Unclassified

SECURITY CLASSIFICATION OF THIS PAGE (When Date Entered)

REPORT DOCUMENTATION PAGE		READ INSTRUCTIONS BEFORE COMPLETING FORM	
1. REPORT NUMBER AFGL-TR-81-0207	2. GOVT ACCESSION NO. A1-A2	3. RECIPIENT'S CATALOG NUMBER 57422	
4. TITLE (and Subtitle) ATMOSPHERIC INFRARED RADIANCE VARIABILITY		5. TYPE OF REPORT & PERIOD COVERED Scientific, Interim.	
7. AUTHOR(s) Editors: C.H. Humphrey* C.R. Philbrick R.M. Nadile D.R. Smith		6. PERFORMING ORG. REPORT NUMBER ERP No. 748	
9. PERFORMING ORGANIZATION NAME AND ADDRESS Air Force Geophysics Laboratory (OPR) Hanscom AFB Massachusetts 01731		8. CONTRACT OR GRANT NUMBER(s)	
11. CONTROLLING OFFICE NAME AND ADDRESS Air Force Geophysics Laboratory (OPR) Hanscom AFB Massachusetts 01731		10. PROGRAM ELEMENT PROJECT, TASK AREA & WORK UNIT NUMBERS 61102F 66900707 2310G411 II.R81/9F	
14. MONITORING AGENCY NAME & ADDRESS (if different from Controlling Office)		12. REPORT DATE 27 May 1981	
		13. NUMBER OF PAGES 119	
		15. SECURITY CLASS (of this report) Unclassified	
		15a. DECLASSIFICATION/DOWNGRADING SCHEDULE	
16. DISTRIBUTION STATEMENT (of this Report) Approved for public release, distribution unlimited			
17. DISTRIBUTION STATEMENT (of the abstract entered in Block 20, if different from Report)			
18. SUPPLEMENTARY NOTES *Visidyne, Inc., Burlington, MA 01803 This research was partially supported by the Air Force In-House Laboratory Independent Research Fund; part of the work was performed under contract F19628-79-C-0005 with Visidyne, Inc.			
19. KEY WORDS (Continue on reverse side if necessary and identify by block number) Infrared Atmospheric structure			
20. ABSTRACT (Continue on reverse side if necessary and identify by block number) Data concerning the spatial and temporal inhomogenities of atmospheric density and composition and their implication concerning the atmospheric infrared radiance are reviewed. Preliminary estimates of the variability in the radiance are presented. In addition, the range of scale sizes from small-scale variations is also considered.			

DD FORM 1 JAN 73 1473

Unclassified 390863
SECURITY CLASSIFICATION OF THIS PAGE (When Date Entered)

1/2

1/2

Contents

1. INTRODUCTION	5
2. CURRENT HIGH ALTITUDE INFRARED RADIANCE MODEL - T. C. Degges	9
3. MODELS OF THE VARIABILITY OF ATMOSPHERIC PROPERTIES - C. H. Humphrey and C. R. Philbrick	25
4. EFFECTS OF ATMOSPHERIC VARIABILITY ON INFRARED RADIANCE PREDICTIONS - T. C. Degges	53
5. ATMOSPHERIC STRUCTURE - C. H. Humphrey, C. R. Philbrick, S. M. Silverman, T. F. Tuan, M. Anapol, and J. B. Kumer	73
6. SUMMARY AND RECOMMENDATIONS	117

Accession
NO.
Dist
PER CALL JC
Dist
A

3/4



1. Introduction

Direct measurements of the infrared radiance from the upper atmosphere and, especially, of the variability in this radiance are very limited. Furthermore, almost no data exists on the variations of the infrared emissions with geophysical parameters, such as latitude or magnetic activity, or with localized dynamic effects. Thus, to obtain estimates of the infrared radiance of the atmosphere, one must rely on computer models. The computer model currently being used to predict the infrared radiance at high altitude is a modified version of the one described by Degges and Smith¹ (1977). This model is intended to simulate the radiative properties for average midlatitude atmospheric conditions. In this report we discuss data and supporting phenomenology that are required to upgrade this model to include the variations of the upper atmospheric radiation resulting from changes in geophysical conditions.

The intensity of infrared emissions in the upper atmosphere is dependent on both the density and distribution of specific molecules and the sources that excite the emitting levels of these molecules. At the present time there is insufficient data concerning the density and the distribution of the IR emitting species of the upper atmosphere to be able to fully describe these parameters. However, the

(Received for publication 22 May 1981)

1. Degges, T. C. and Smith, H. J. P. (1977) A High Infrared Radiance Model, AFGL-TR-77-0271, AD A059 242, Final Report, Contract F19628-77-C-0041, Visidyne, Inc., Burlington, Mass.

density and distribution of these species can be estimated with varying degrees of confidence. These estimates are based on calculations, which are supported by measurements, and on models that include the current understanding of the photochemical, excitation, and transport processes in the upper atmosphere. In this report, data that can be related to either the infrared emission or to the species concentrations that produce these emissions are considered.

The long-term purpose of this study is to develop a data base sufficient for the modeling, not only of the IR radiance, but of its variability. Both spatial and temporal inhomogeneities and their magnitudes and frequencies of occurrence are considered. This report represents an effort to clarify and summarize the state of our knowledge at the present time. An attempt has been made to identify those aspects of the problem where additional effort needs to be made.

The variations and structured features observed in the concentrations of the upper atmospheric species may be divided into three general classes. The first general class is the long-term variations of the quiescent atmosphere that are associated with vertical profiles. These variations can be described by the hydrostatic equation and the ideal gas law. From a knowledge of the density, temperature, and composition near the earth's surface, the profiles of the major species can be derived from measured profiles of temperature, turbulent and molecular diffusion velocities, solar radiation dissociation rates, and chemical reaction rates (for example, see Keneshea et al, 1979²). This class of atmospheric variations includes those resulting from atmospheric heating (which depends, in turn, upon solar cycle, latitude, season, and local time). The profiles of this class of variations are described in detail by well-developed empirical models such as CIRA 72, USSA 76, Jacchia 77 (J77), and MSIS 78.

The second and third classes of atmospheric variations are shorter period waves and localized heating events that are superimposed on the smooth diffusive profiles of the first class. The second class includes those short-term wave-like structures that are the fluid responses to the many different types of forces applied to the atmosphere. These result in structure with a wide range of scale sizes, amplitudes, and irregular features that result from wave interference or dissipative breakdown of waves into turbulent eddies. The source of these variations include the diurnal and semidiurnal (and higher order) tidal motion (Chapman and Lindzen, 1970,³ Forbes and Garrett, 1978⁴) and the gravity wave structures that

2. Keneshea, T. J., Zimmerman, S. P. and Philbrick, C. R. (1979) A dynamic model of the mesosphere and lower thermosphere, Planet. Space Sci. 27:385-401.
3. Chapman, S. and Lindzen, R. S. (1970) Atmospheric Tides, D. Reidel, Hingham, Mass.
4. Forbes, J. M. and Garrett, H. B. (1978) Solar diurnal tide in the thermosphere, J. Atmos. Sci. 35:148-208.

are generally propagated from the lower atmosphere into the middle and upper atmosphere (Hines, 1974,⁵ Reber et al, 1975⁶).

The third class of variations includes irregular structures that are due to the deposition of coupled energy from magnetospheric particles and fields. These energy sources provide strong localized heating and thereby produce many types of irregular features in the atmosphere. Such heating may result from direct particle precipitation into the atmosphere from the solar wind or the trapped particle regions of the magnetosphere, such as aurora. However, the largest heating effects result from plasma interactions with the neutral atmosphere when electric and magnetic fields accelerate the ionospheric plasma (Cole, 1971,⁷ Mayr and Harris, 1978⁸). The high-latitude regions are frequently subjected to large-scale Joule heating and to very localized effects, such as the "momentum source" and high structured particle precipitation events. The strongly heated regions may be so perturbed by the energy input that the vertical profiles of individual species can no longer be represented by hydrostatic profiles.

The modeling efforts and experimental data will be reviewed in order, according to the three classes of variations described above. This ordering has the advantage of allowing a continuity of development in the complexity of the atmospheric features. In addition, the variations resulting from each class are generally considered a superposition to the effect of the previous classes. Recently a great deal of attention has been given to determining the atmospheric properties at higher satellite altitudes. However, the regions that contribute most significantly to the infrared emission of interest are from 50 to 200 km. This review will concentrate on satellite and rocket results at these altitudes.

The application of the atmospheric models and measurements to the calculation of infrared radiance will generally take two forms. In the first form, that applies generally to the smooth variations of the first class, an atmospheric profile of temperature and species concentration is used as an input to a model for the infrared radiance (such as the High Altitude Infrared Radiance Model of Degges¹ (Degges and Smith, 1977) described in Chapter 2) and the infrared radiance evaluated. Examples of infrared radiances, based on calculations using the atmospheric

-
5. Hines, C.O. (1974) The Upper Atmosphere in Motion, American Geophysical Union Monograph Ser 18.
 6. Reber, C.A., Hedin, A.E., Pelz, D.T., Potter, W.E. and Brace, L.H. (1975) Phase and amplitude relationships of wave structure observed in the lower thermosphere, J. Geophys. Res. 80:4576-4580.
 7. Cole, K.D. (1971) Electrodynamic heating and movement of the thermosphere, Planet Space Sci. 19:59-75.
 8. Mayr, H.G. and Harris, I. (1978) Some characteristics of electric field momentum coupling with the neutral atmosphere, J. Geophys. Res. 83:3327-3336.

properties described in Chapter 3, are given in Chapter 4. In Chapter 3 various atmospheric models are discussed with a concentration on the J77 model. Examples of the predictions of the J77 model are presented and compared to measurements of the atmospheric properties. In addition, existing data concerning the variability of the minor atmospheric species is also reviewed.

In the second form, where irregular variations are considered, the standard deviation and the auto-correlation function or power spectral density are used to estimate the expected variations in the radiance as discussed in Chapter 5. These estimates require certain assumptions concerning the connection between atmospheric properties and the resultant radiance. In Chapter 5 the sources of the small-scale variability are discussed, experimental data reviewed, and a preliminary summary of the sizes and magnitude of the variability presented. In addition, an example of the use of this material to construct a power spectral density is given, as well as a proposed method of generating a model for the auroral power spectral density for two specified wavelengths in the infrared.

Finally, in Chapter 6, a brief summary of the important problems that must be given further attention and that point the directions for future research are briefly discussed.

References

1. Degges, T. C. and Smith, H. J. P. (1977) A High Infrared Radiance Model, AFGL-TR-77-0271, AD A059 242, Final Report, Contract F19628-77-C-0041, Visidyne, Inc., Burlington, Mass.
2. Keneshea, T. J., Zimmerman, S. P. and Philbrick, C. R. (1979) A dynamic model of the mesosphere and lower thermosphere, Planet. Space Sci. 27:385-401.
3. Chapman, S. and Lindzen, R. S. (1970) Atmospheric Tides, D. Reidel, Hingham, Mass.
4. Forbes, J. M. and Garrett, H. B. (1978) Solar diurnal tide in the thermosphere, J. Atmos. Sci. 35:148-208.
5. Hines, C. O. (1974) The Upper Atmosphere in Motion, American Geophysical Union Monograph Ser 18.
6. Reber, C. A., Hedin, A. E., Pelz, D. T., Potter, W. E. and Brace, L. H. (1975) Phase and amplitude relationships of wave structure observed in the lower thermosphere, J. Geophys. Res. 80:4576-4580.
7. Cole, K. D. (1971) Electrodynamic heating and movement of the thermosphere, Planet Space Sci. 19:59-75.
8. Mayr, H. G. and Harris, I. (1978) Some characteristics of electric field momentum coupling with the neutral atmosphere, J. Geophys. Res. 83:3327-3336.

2. Current High Altitude Infrared Radiance Model

T.C. Degges
Visidyne, Inc.
Burlington, Mass.

The High Altitude Infrared Radiance Model represents the current capability in a continuing program (Corbin et al, 1969,¹ Degges, 1972,² 1974,³ Degges and Smith, 1977⁴) to predict infrared radiance levels in the upper atmosphere for the spectral range from 2.5 to 25 μm . In these predictions emphasis is placed on radiation originating at altitudes between 60 and 500 km. Comparison of the predictions of the computer model with experimental measurements serves to check the adequacy of the infrared model and provides greater understanding of the atmospheric properties that determine the infrared radiation.

1. Corbin, V. L., Dalgarno, A., Degges, T. C., House, F. B., Lilienfeld, P., Ohring, G., and Oppel, G. E. (1969) Atmospheric Radiance Models for Limb-Viewing Geometry in the Five-to-Twenty-five Micron Spectral Region, AFCRL-69-0552, AD 868 194L.
2. Degges, T. C. (1972) A High Altitude Radiance Model, AFCRL-72-0273, AD 745 319, Final Report, Contract F19628-71-C-0156, Visidyne, Inc., Burlington, Mass.
3. Degges, T. C. (1974) A High Altitude Radiance Model, AFCRL-TR-74-0606, AD A008 035, Final Report, Visidyne, Inc., Burlington, Mass.
4. Degges, T. C. and Smith, H. J. P. (1977) A High Infrared Radiance Model, AFGL-TR-77-0271, Final Report, Contract F19628-77-C-0041, Visidyne, Inc., Burlington, Mass., AD A059242.

The principal sources of infrared radiation at altitudes greater than 50 km are water vapor (H_2O), carbon dioxide (CO_2), ozone (O_3), nitric oxide (NO), carbon monoxide (CO), and the hydroxyl radical (OH). The results of the recent SPIRE experiment (Stair et al, 1981⁵) are consistent with this conclusion. While some calculations have been made that include CO; its abundance and altitude variation are uncertain. It is not included in the model. Similarly, while OH is known to be important at wavelengths from the visible through 3.5 μm , it is not presently included. Although the model includes altitude profiles of the species concentrations of H_2O , CO_2 , O_3 , and NO, there is not sufficient knowledge to provide concentration profiles for all latitudes and seasons. The present model approximates average midlatitude conditions.

The radiance model is further limited by the incomplete knowledge of the physical processes that control the population of infrared emitting states of atmospheric molecules. Except for the pure rotational radiation from molecules such as water, the degree of excitation of vibrational levels determines the radiation from infrared emitting molecules. The most important mechanisms for excitation of vibrational and rotational levels are collisional excitation and deexcitation, absorption and reemission of electromagnetic radiation, and exothermic chemiluminescent reactions. In the troposphere and lower stratosphere collisional processes are rapid enough to control the population of vibrational levels. Above 50 km, however, collisional excitation becomes less efficient and radiative processes become important so that the combined effects of collisional and radiative processes must be considered. Below an altitude of about 90 km, molecular nitrogen and oxygen are the most important collision partners. Above this altitude atomic oxygen becomes important in determining the collisional excitation and deexcitation rates.

In determining the effects of radiation on the populations of the vibrational levels of infrared active molecules, it is necessary to separate the radiation due to a single change in vibration quantum numbers from the rest of the radiation field. This can be achieved by assuming that the individual rotational lines of a band have Doppler spectral profiles and do not overlap. This assumption allows the construction of radiative transfer functions that are adequate numerical approximations for the calculation of the absorption of infrared energy from the sun, the earth's surface, and molecules at all altitudes in the atmosphere.

Figure 1 illustrates the geometry employed in the radiance model. A molecule at point P absorbs radiation from three sources: 1) the sun, 2) the lower boundary

5. Stair, A. T., Jr., Nadile, R. M., Ulwick, J. C., Baker, K. D. and Baker, D. J. (1981) Infrared measurements of aurora airglow and the upper atmosphere. Paper presented at AIAA Aerospace Sciences Meeting, Jan. 1981, St. Louis, Missouri, Paper no. AIAA-81-0421.

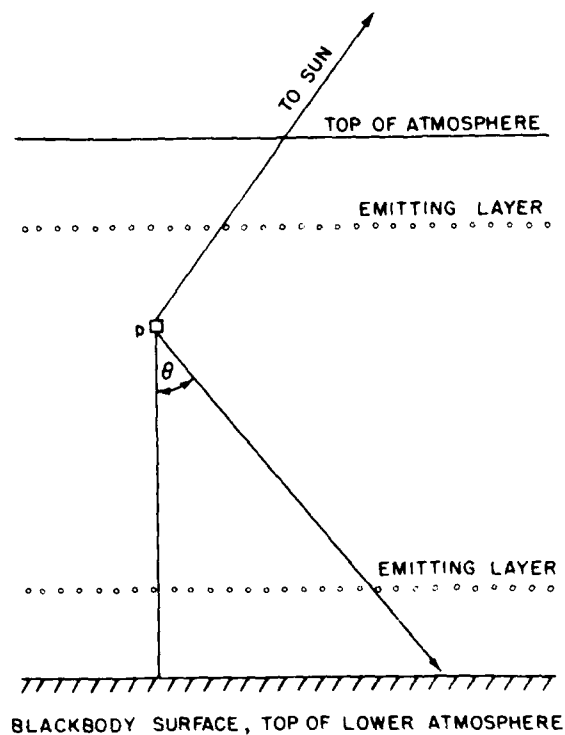


Figure 1. Geometry Assumed in High Altitude Infrared Radiance Model

that radiates as a blackbody, and 3) other molecules between the lower and upper boundaries. Radiative transfer functions are needed to compute the effects of absorption of radiation by other molecules between each of these sources and the molecules at point P. In the absence of collisional excitation and deexcitation, the simplest integral equation that can be written to describe radiative transport in a finite plane parallel atmosphere is

$$J(\tau) = \frac{1}{2} \int_0^{\tau_{\max}} K_1(|\tau-t|) J(t) dt + S(\tau) \quad (1)$$

This equation assumes that there is only one radiative transition involved and the radiation emitted by a molecule after it has absorbed radiation is independent of the direction of incidence of the absorbed radiation. Here τ is a measure of the optical path length in the vertical direction. $J(\tau)$ is a dimensionless measure of

the population of the upper (emitting) molecular state. $K_1(\tau)$ is the radiative transfer function that accounts for absorption of radiation emitted by molecules at a distance τ from the absorbing molecule. $S(\tau)$ is an auxiliary function that includes the effects of radiation originating outside the atmosphere. If there is a blackbody source located at the lower boundary from which the optical path length is measured ($\tau = 0$ at the lower boundary), then

$$S(\tau) = \frac{1}{2} N_0 K_2(\tau) . \quad (2)$$

Here N_0 is the radiance of the lower boundary in arbitrary units, such as $W \text{ cm}^{-2} \text{ ster}^{-1}$, or the spectral radiance in units such as $W \text{ cm}^{-2} \text{ ster}^{-1} (\text{wavelength interval})^{-1}$. $K_2(\tau)$ is the radiative transfer function that accounts for absorption between the lower boundary and a molecule at optical depth τ above that boundary.

When a collimated beam of light is incident on the top of the atmosphere another term must be added to the function $S(\tau)$ in Eqs. (1) and (2). If the flux is incident at a zenith angle whose cosine is μ and has an intensity in arbitrary units, such as $F W \text{ cm}^{-2}$ normal to its direction, the term added to $S(\tau)$ has the form $F M_1(\tau_{\text{max}} - \tau)/\mu$. Here $M_1(\tau)$ is the transmission along an optical path with depth τ .

The starting point of the treatment of radiative transfer for the model is the treatment of a single spectral line. To extend this treatment to a vibration-rotation band the following assumptions are made (in addition to assuming that each line has the same Doppler profile shape):

1. Rotational levels within a vibration level remain in equilibrium with the translational temperature. This is valid up to an altitude of at least 150 km according to Goody (1964).⁶
2. There is complete redistribution of absorbed energy among all rotational levels.
3. The spectral distribution of radiation from a line is independent of the energy of the radiation absorbed by the level.
4. Line strengths are used as if each line were at the band center, neglecting wavelengths variation across a band.
5. There is no overlap of adjacent lines.
6. Temperature variations at different altitudes do not affect the radiative transfer.

These assumptions are introduced to make the computer calculation possible in a reasonable length of time. They do cause the results to be uncertain to factors

6. Goody, R. M. (1964) Atmospheric Radiation, I, Theoretical Basis, Oxford University.

of two and, thus, care must be used in interpreting the results. For example, the sixth assumption results in vibrational populations of CO_2 that are too low above the mesopause (80-90 km) and, consequently, computed radiances in the $15 \mu\text{m}$ region may be low by as much as 50 percent.

In order to simplify the computer programming, a single set of radiative transfer functions is used for all parallel bands of linear molecules and another set is used for perpendicular bands. These functions vary with the rotational temperature. In order to account partially for temperature variation, the program does not use the parameter τ , but rather a derived parameter τ_0 that is the optical thickness at the center of the strongest line in the band. This is either an R branch line for a parallel band or a Q branch line for a perpendicular band.

In practice, rather than formally integrating a modified Eq. (1), including a τ dependent function to account for collisional deexcitation and an additional source term to account for collisional excitation, the computer program sets an initial vibrational population at each altitude and computes (at each altitude) the total radiative excitation that results from the sum of radiation from the earth and lower atmosphere, plus the sun and upper atmosphere. Vibrational populations are then determined by balancing collisional and radiative excitation and deexcitation rates. Total band intensities are computed at an observation point inside or outside the atmosphere by determining the optical path from each altitude to the observation point and integrating the product of local emission rate and the band radiative transfer function $M_1(\tau)$.

The spectral distribution of radiation is determined by finding a mean effective temperature and line-of-sight column density for the radiating molecules, computing intensity of each line in the band with the line function $L(\tau)$, summing the line emission rates, and scaling each line emission rate so that the total band intensity is obtained.

Input data to the computer program include altitude profiles of the temperature and the N_2 , O_2 , O , H_2O , CO_2 , NO , and O_3 concentrations at altitudes between ground level and 700 km. N_2 , O_2 , and CO_2 concentrations below 90 km are computed directly from the temperature profile. The O concentration is based on the U.S. Standard Atmosphere 1976 (USSA 76), but any other source may be used. Depending on time and location O concentrations in the critical region 90 to 120 km may vary by as much as an order of magnitude (Offerman et al, 1981⁷); however, this variation is presently not included in the program. Concentrations of H_2O , NO , and O_3 may be uncertain by factors of two to five or more due to the large expected variability of these species and the inaccuracy of currently available measurements (see Section 3.5).

7. Offerman, D., Friedrich, V., Ross, P. and von Zahn, V. (1981) Neutral gas composition measurements between 80 - 120 km. Planet Space Sci. (in publication).

There have been relatively few measurements of the altitude variation of the concentrations of infrared emitting species at altitudes above 40 km, the limit of direct sampling by balloons. While ozone measurements by different scientists generally agree with each other and with theoretical computations for altitudes up to 100 km (Weeks et al, 1978⁸) and NO profiles appear reasonably consistent between about 80 and 150 km at middle latitudes (Cravens and Stewart, 1978⁹), corresponding data are less abundant for other important species. There are a few cases where indirect data are available, which, when combined with computational models, can yield limits to concentrations. Thus, Anderson (1971a)¹⁰ has been able to put an upper limit on the total OH abundance above 60 km from measurement of its resonance fluorescence. This result allows a computation of possible H₂O profiles between 50 and 100 km using a photo-chemical model that includes vertical transport by eddy diffusion. In a later paper Anderson (1971b)¹¹ gives a measured altitude profile for OH with error limits of a factor of two.

At present, estimates of chemical abundances of minor species important in predicting infrared radiation require the use of photochemical computations. Despite the inclusion of the best estimates of the effects of transport processes such as eddy mixing, these computations must be used with some caution. The current infrared model relies on published measurements and recent calculations to estimate the abundance of infrared emitting species in the atmosphere.

Water vapor abundances are not well known at high altitudes, even in the stratosphere. Direct measurements of water vapor abundances place lower and upper limits of the volume mixing ratio at two and ten ppm in the upper stratosphere. In a recent optical measurements from a balloon Goldman et al (1973)¹² observed the thermal emission from the rotational spectrum near 25 μ m and determined that the volume mixing ratio near 30 km was nearly three ppm.

8. Weeks, L.H., Good, R.E., Randhawa, J.S. and Trinks, H. (1978) Ozone measurements in the stratosphere, mesosphere, and lower thermosphere during Alladdin 74, *J. Geophys. Res.* 83:978-982.
9. Cravens, T.E. and Stewart, A.I. (1978) Global morphology of nitric oxide in the lower E region, *J. Geophys. Res.* 83:2446-2452.
10. Anderson, J.G. (1971a) Rocket-borne ultraviolet spectrometer measurement of OH resonance fluorescence with a diffusive transport model for mesospheric photochemistry, *J. Geophys. Res.* 76:4634-4652.
11. Anderson, J.G. (1971b) Rocket measurement of OH in the mesosphere, *J. Geophys. Res.* 76:7820-7824.
12. Goldman, A., Murray, D.G., Murcray, F.H., Williams, W.J. and Brooks, J.N. (1973) Distribution of water vapor in the stratosphere as determined from balloon measurements of atmospheric emission spectra in the 24-29 μ m region, *Appl. Opt.* 12:1045-1053.

Radford et al (1977)¹³ used ground based microwave soundings to determine mesospheric water vapor concentrations. They obtained 10 ppmV at 50 km with a maximum of 15 ppmV at 60 km. Rogers et al (1977a)¹⁴ have analyzed radiance measurements obtained from the AFGL/DNA ICECAP program to infer an H₂O mixing ratio of 3.5 ppmV between 50 and 70 km during late winter at Fairbanks, Alaska. At present, 5 ppmV is assumed as a reasonable mixing ratio for use in the radiance model. Above 90 km this value is too high because of photodissociation. During summer at high latitudes, a value one tenth of this may be appropriate near the cold mesopause. Figure 2 compares the model calculations of the H₂O radiance at 6.3 μm with the AFGL SPIRE measurements from a rocket payload launched at Poker Flat on 28 September 1977 (Stair et al, 1981⁵). There is good agreement between 60 and 70 km where the model and data overlap. However, the AFGL ELE experiment, launched from White Sands on 6 August 1977 requires that the H₂O concentrations be reduced by a factor of five at 90 km in order to achieve agreement. These differences may simply represent daily, seasonal, or latitudinal variations in the atmospheric water vapor content.

A large number of measurements of NO concentrations are available. Representative midlatitude concentrations are shown in Figure 3 that are based on the twilight measurements of Baker et al (1977)¹⁵ and the calculations of Oran et al (1975)¹⁶. NO concentrations are greater at higher latitudes. The nighttime SPIRE data at 5.4 μm require the use of the higher daytime concentrations of Figure 3, indicating that the production of NO is enhanced at higher latitudes (see Section 3.5).

Calculations of O₃ abundances must take into account lateral transport by winds, as well as vertical transport by eddy mixing and molecular diffusion, in addition to photochemistry. Current photochemical models agree with observations obtained by measuring absorption of solar and stellar ultraviolet radiation and those deduced from measurements of the molecular oxygen 1.37 μm (O₂ (1Δ_g)) infrared atmospheric band. The exact density profile depends strongly on assumed eddy-diffusion coefficients because of the chemistry involving atomic H and O

13. Radford, H.E., Litvak, M.M., Gottlieb, C.A., Rosenthal, S.K. and Lilley, A.E. (1977) Mesospheric water vapor measurements, J. Geophys. Res. 82:472-478.
14. Rogers, J.W., Stair, A.T., Degges, T.C., Wyatt, C.L. and Baker, D.J. (1977) Rocketborne measurement of mesospheric H₂O in the auroral zone, Geophys. Res. Lett. 4:366-368.
15. Baker, K.D., Nagy, A.F., Olsen, R.O., Oran, E.S., Randhawa, J., Strobel, D.F. and Tohmatsu, T. (1977) Measurement of the nitric oxide altitude distribution in the mid-latitude mesosphere, J. Geophys. Res. 82:3281-3286.
16. Oran, J.S., Julieene, P.S. and Strobel, D.F. (1975) Odd nitrogen in the thermosphere, J. Geophys. Res. 80:3068-3076.

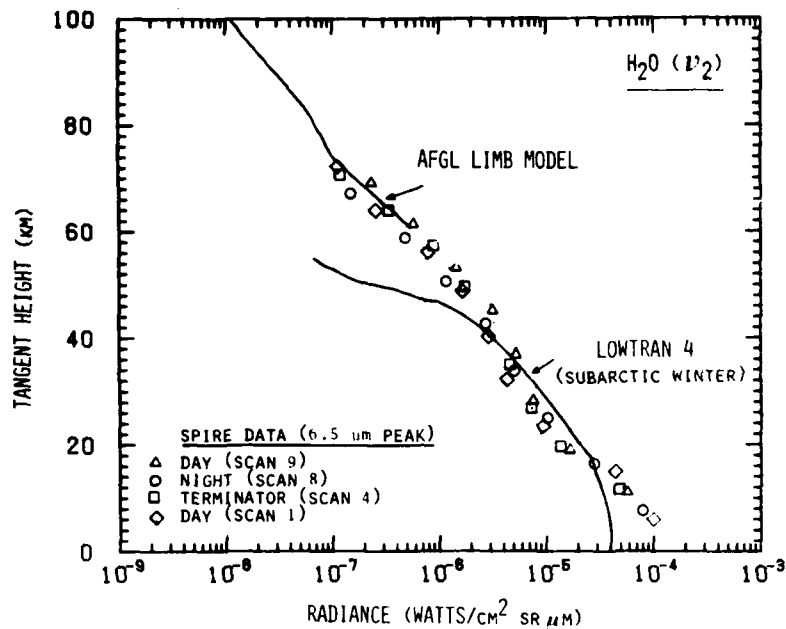


Figure 2. Comparison of SPIRE Water Vapor Measurement at 6.5 μm With Model Calculations

concentrations. O_3 abundances used in the current infrared radiance model are shown in Figure 4. Below 60 km the ozone model in the USSA 76 is used. These profiles rely heavily on measurements by Llewellyn and Witt (1977)¹⁷ and Hays and Roble (1973).¹⁸ The calculations of Thomas and Bowman (1972)¹⁹ have been used as a guide to predict diurnal variations in the O_3 abundances. Diffusive equilibrium is assumed above 100 km.

Figure 5 compares SPIRE measurement data for 9.6 μm O_3 limb viewing radiances and those computed with the O_3 profiles of Figure 4. Such good agreement is to some extent fortuitous. In matching O_3 radiance profiles taken from zenith viewing rocketborne instruments with model predictions, features of the nighttime O_3 concentration profile must be shifted at times by as much as 5 km in altitude. Concentrations may vary by as much as a factor of three.

17. Llewellyn, E. J. and Witt, G. (1977) The measurement of ozone concentrations at high latitude during the twilight, Planet. Space Sci. 25:165-172.
18. Hays, P. B. and Roble, R. G. (1973) Observations of mesospheric ozone at low latitudes, Planet Space Sci. 21:273-279.
19. Thomas, L. and Bowman, M. R. (1972) The diurnal variations of hydrogen and oxygen constituents in the mesosphere and lower thermosphere, J. Atmos. Terr. Phys. 34:1843-1858.

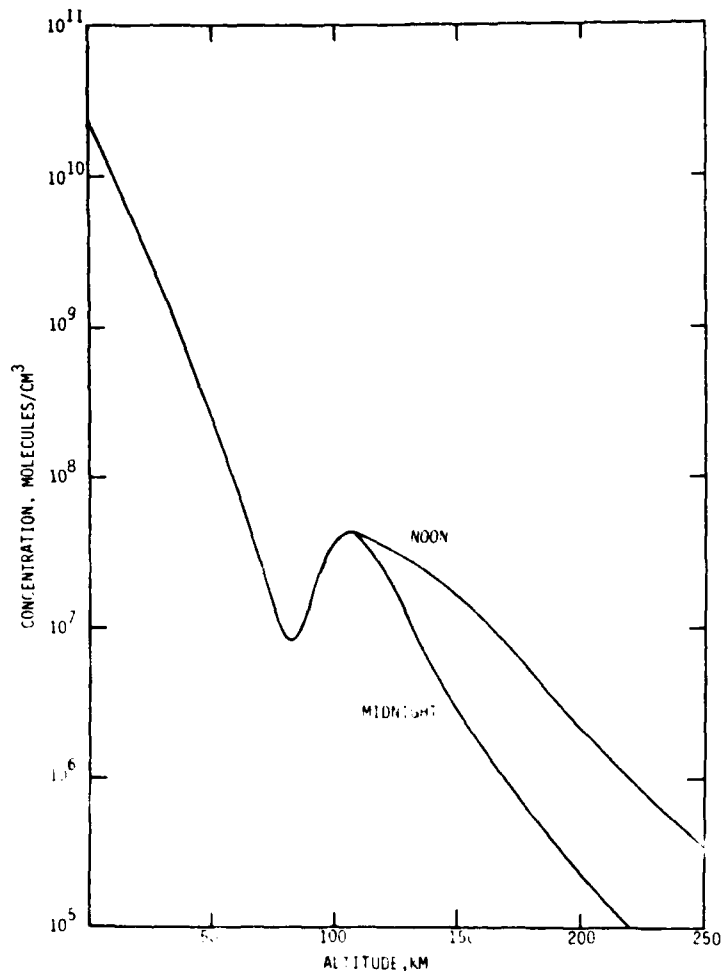


Figure 3. Nitric Oxide Concentration Values Used in the High Altitude Infrared Radiance Model

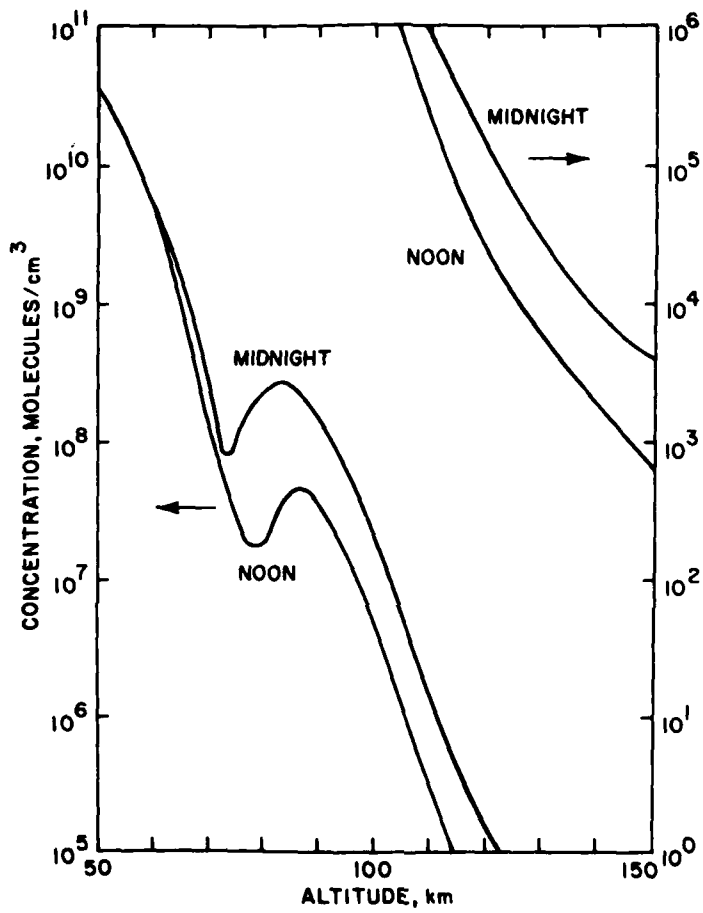


Figure 4. O₃ Concentration Profiles Used in the High Altitude Infrared Radiance Model

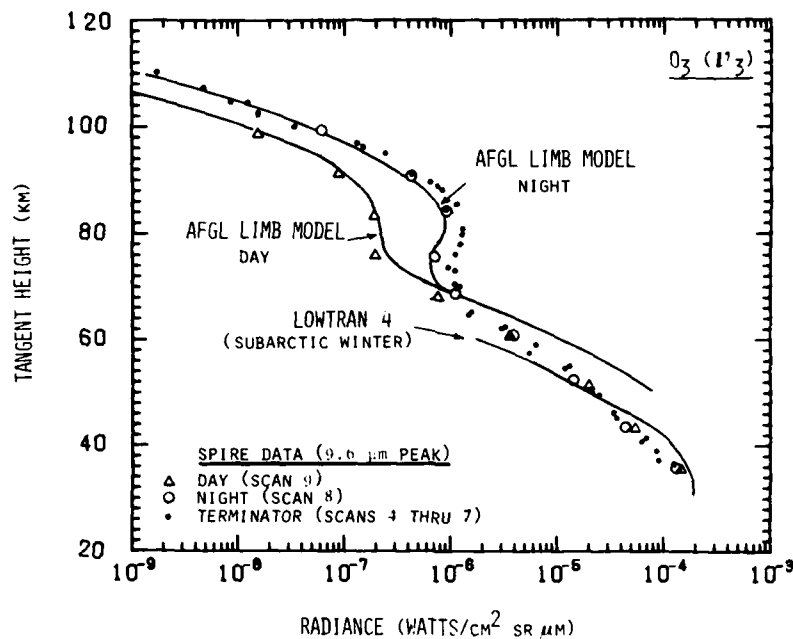


Figure 5. Comparison of SPIRE 9.6 μm Data With Model Calculations

CO_2 is dissociated by solar radiation and lost by reaction with O^+ in the upper atmosphere. Below about 110 km it is well shielded from dissociation by molecular oxygen and, thus, should remain well mixed below 100 km. CO_2 concentrations have been reported for two sets of measurements using mass spectrometers. Philbrick et al (1973)²⁰ presented measurements that showed that the CO_2 was in mixing equilibrium between 85 and 100 km. The measurements by Trinks and Fricke (1978)²¹ indicated that, if the nighttime profile is assumed to be in diffusive equilibrium above 100 km, a calculation that accounts for dissociation and loss of CO_2 by photodissociation and reaction with O^+ gives reasonable agreement for the daytime lower stratosphere. The current model does not include the daytime loss processes implied by the results of Trinks and Fricke (1978).²¹ Complete mixing is assumed up to a level between 90 and 120 km and diffusive equilibrium is assumed above that variable level.

20. Philbrick, C.R., Faucher, G.A. and Trzcinski, E. (1973) Rocket measurements of mesospheric and lower thermospheric composition, Space Research XIII:255-260.

21. Trinks, H. and Fricke, K.H. (1978) Carbon dioxide concentrations in the lower thermosphere, J. Geophys. Res. 83:3883-3886.

Figure 6 compares the measured SPIRE $15 \mu\text{m}$ CO_2 radiance and the model calculations. Agreement is good below 95 km, but above that altitude the measured radiance levels are about twice the model predictions. Part of the discrepancy is due to use of assumption 6 above. Kumer (1979)²² has obtained better agreement by treating the temperature variation near the mesopause, but that analysis still finds the need for another excitation mechanism. Sharma and Nadile (1980)²³ have also analyzed this data. They obtained agreement between the data and predictions by assuming an oxygen concentration with a peak value of $1.7 \times 10^{11} \text{ cm}^{-3}$ at 105 km and a room temperature deactivation rate of CO_2 by oxygen atoms of $5 \times 10^{-13} \text{ cm}^3/\text{sec}$.

Figure 7 shows a comparison of the predictions of the High Altitude Radiance Model and the SPIRE data over the total spectral range measured. In the spectral region from 9 to $17 \mu\text{m}$ the predictions appear to be too low.

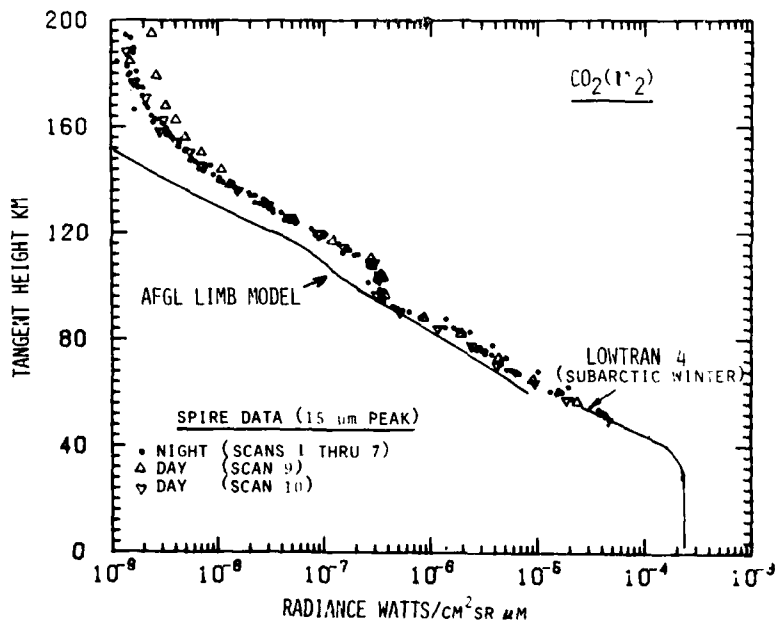


Figure 6. Comparison of SPIRE $15 \mu\text{m}$ CO_2 Radiances With Model Calculations

22. Kumer, J.B. (1979) Private communication.

23. Sharma, R.D. and Nadile R.M. (1981) Carbon dioxide (ν_2) radiance results using a new non-equilibrium model. Paper presented at AIAA Aerospace Sciences Meeting, Jan. 1981, St. Louis, Missouri, Paper no. AIAA-81-0421.

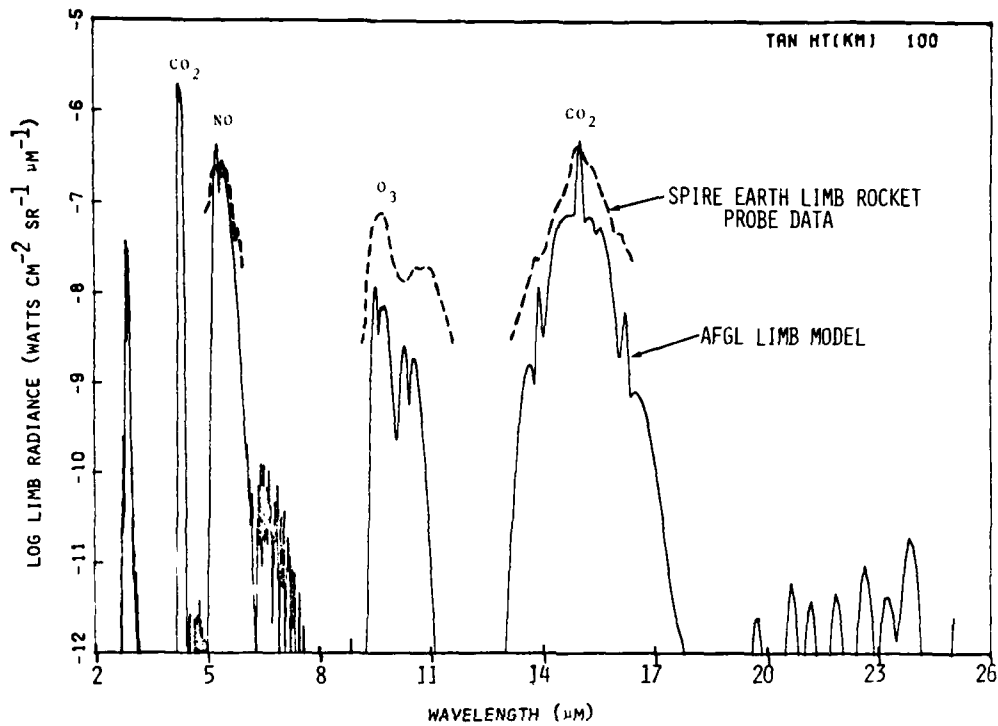


Figure 7. Comparison of SPIRE Measurements at 90 km of the Sunlit Exoatmospheric Limb Viewing Radiance With Model Calculations Under Sunlit Conditions at 100 km

The largest uncertainties in applying the infrared radiance model result from lack of knowledge of the atmospheric temperature and molecular species concentrations. Further uncertainties arise from the fact that not all radiating molecules or possible excitation mechanisms are included in the program. Also, other bands of those molecules that are included may have significant effects. The modeling effort relies on experiments to identify the most appropriate additions for future work.

References

1. Corbin, V.L., Dalgarno, A., Degges, T.C., House, F.B., Lilienfeld, P., Ohring, G., and Oppel, G.E. (1969) Atmospheric Radiance Models for Limb-Viewing Geometry in the Five-to-Twenty-five Micron Spectral Region, AFCRL-69-0552, AD 868 194L.
2. Degges, T.C. (1972) A High Altitude Radiance Model, AFCRL-72-0273, AD 745 319, Final Report, Contract F19628-71-C-0156, Visidyne, Inc., Burlington, Mass.
3. Degges, T.C. (1974) A High Altitude Radiance Model, AFCRL-TR-74-0606, AD A008 035, Final Report, Visidyne, Inc., Burlington, Mass.
4. Degges, T.C. and Smith, H.J.P. (1977) A High Infrared Radiance Model, AFGL-TR-77-0271, Final Report, Contract F19628-77-C-0041, Visidyne, Inc., Burlington, Mass., AD A059242.
5. Stair, A.T., Jr., Nadile, R.M., Ulwick, J.C., Baker, K.D. and Baker, D.J. (1981) Infrared measurements of aurora airglow and the upper atmosphere. Paper presented at AIAA Aerospace Sciences Meeting, Jan. 1981, St. Louis, Missouri, Paper no. AIAA-81-0421.
6. Goody, R.M. (1964) Atmospheric Radiation, I, Theoretical Basis, Oxford University.
7. Offerman, D., Friedrich, V., Ross, P. and von Zahn, V. (1981) Neutral gas composition measurements between 80 - 120 km. Planet Space Sci. (in publication).
8. Weeks, L.H., Good, R.E., Randhawa, J.S. and Trinks, H. (1978) Ozone measurements in the stratosphere, mesosphere, and lower thermosphere during Alladdin 74, J. Geophys. Res. 83:978-982.
9. Cravens, T.E. and Stewart, A.I. (1978) Global morphology of nitric oxide in the lower E region, J. Geophys. Res. 83:2446-2452.
10. Anderson, J.G. (1971a) Rocket-borne ultraviolet spectrometer measurement of OH resonance fluorescence with a diffusive transport model for mesospheric photochemistry, J. Geophys. Res. 76:4634-4652.
11. Anderson, J.G. (1971b) Rocket measurement of OH in the mesosphere, J. Geophys. Res. 76:7820-7824.
12. Goldman, A., Murray, D.G., Murcray, F.H., Williams, W.J. and Brooks, J.N. (1973) Distribution of water vapor in the stratosphere as determined from balloon measurements of atmospheric emission spectra in the 24-29 μm region, Appl. Opt. 12:1045-1053.
13. Radford, H.E., Litvak, M.M., Gottlieb, C.A., Rosenthal, S.K. and Lilley, A.E. (1977) Mesospheric water vapor measurements, J. Geophys. Res. 82:472-478.
14. Rogers, J.W., Stair, A.T., Degges, T.C., Wyatt, C.L. and Baker, D.J. (1977) Rocketborne measurement of mesospheric H_2O in the auroral zone, Geophys. Res. Lett. 4:366-368.
15. Baker, K.D., Nagy, A.F., Olsen, R.O., Oran, E.S., Randhawa, J., Strobel, D.F. and Tohmatsu, T. (1977) Measurement of the nitric oxide altitude distribution in the mid-latitude mesosphere, J. Geophys. Res. 82:3281-3286.
16. Oran, J.S., Julieene, P.S. and Strobel, D.F. (1975) Odd nitrogen in the thermosphere, J. Geophys. Res. 80:3068-3076.

17. Llewellyn, E. J. and Witt, G. (1977) The measurement of ozone concentrations at high latitude during the twilight, Planet. Space Sci. 25:165-172.
18. Hays, P. B. and Roble, R. G. (1973) Observations of mesospheric ozone at low latitudes, Planet Space Sci. 21:273-279.
19. Thomas, L. and Bowman, M. R. (1972) The diurnal variations of hydrogen and oxygen constituents in the mesosphere and lower thermosphere, J. Atmos. Terr. Phys. 34:1843-1858.
20. Philbrick, C. R., Faucher, G. A. and Trzcinski, E. (1973) Rocket measurements of mesospheric and lower thermospheric composition, Space Research XIII:255-260.
21. Trinks, H. and Fricke, K. H. (1978) Carbon dioxide concentrations in the lower thermosphere, J. Geophys. Res. 83:3883-3886.
22. Kumer, J. B. (1979) Private communication.
23. Sharma, R. D. and Nadile R. M. (1981) Carbon dioxide (ν_2) radiance results using a new non-equilibrium model. Paper presented at AIAA Aerospace Sciences Meeting, Jan. 1981, St. Louis, Missouri, Paper no. AIAA-81-0421.

Contents

1. Introduction	25
2. Atmospheric Models	26
3. Atmospheric Measurements Compared with Models	38
4. Geomagnetic Induced Variations of Species Concentrations	42
5. Variations in Concentrations of the Minor Atmospheric Species	42

3. Models of the Variability of Atmospheric Properties

C.H. Humphrey
Visidyne, Inc.
Burlington, Mass.

C.R. Philbrick
Air Force Geophysical Laboratory
Hanscom Air Force Base, Mass.

1. INTRODUCTION

As discussed in Chapter 2, predictions of the infrared radiance are made principally on the basis of theoretical models that utilize observations of the atmospheric temperatures and species concentrations. Extensive measurements of these properties of atmosphere have been carried out over the past ten years using ground-based, rocket and satellite borne instruments. From these measurements a number of models have been developed to describe the behavior of the smooth atmospheric profiles that result from variations in the solar heating, magnetic activity, and motion of the earth.

In this chapter these models and measurements that support these models are reviewed briefly. Special emphasis is given to the *Jacchia 77 (J77)* model as this model has been selected as the basis for updating the high altitude infrared model to include the effects of atmospheric variability. This review will enable us to draw some inferences concerning the variability of the atmospheric infrared radiance that can result from the variations in species concentrations and

temperature. In Chapter 4 initial efforts to include some of the variations represented by these models in the calculation of the infrared radiance are presented.

2. ATMOSPHERIC MODELS

2.1 CIRA 72

In CIRA 72 (COSPAR, 1972¹) the latest internationally adopted model, a mean COSPAR International Reference Atmosphere compiled by K. S. Champion and R. A. Schweinfurth for the altitude range 25 to 500 km is presented. This atmosphere represents average diurnal, seasonal, semiannual, and geomagnetic conditions appropriate to 30°N latitude and a 10.7 cm solar flux of $145 \times 10^{-22} \text{ W m}^{-2} \text{ Hz}^{-1}$. The resultant exospheric temperature is 1000 K. In addition, CIRA 72 presents tables of the atmospheric properties as functions of latitude, time of year for altitudes from 25 to 110 km due to G. V. Groves and tables of atmospheric profiles for altitudes from 110 to 1000 km with exospheric temperatures ranging from 500 to 2200 K, derived from the work of L. Jacchia.² Experimental data that support these models are also discussed, as well as the variations to be expected in these models.

2.2 USSA 76

The U.S. Standard Atmosphere 1976, (USSA 76) (COESA, 1976³) presents a single consistent model of globally averaged values of the atmospheric parameters for altitudes up to 1000 km. This model is assumed to be representative of moderate solar activity. The presentation of this model included a review of some features of the variation of atmospheric properties. Seasonal and latitudinal variations in the mean monthly temperature and density below 90 km are compared with average values of USSA 76 in Figures 1 and 2 and are in general agreement with similar results presented in CIRA 72. Figure 2 shows that variations of as much as 50 percent in density can occur at altitudes at which significant infrared radiation is produced. Such variations in temperature and density can lead to appreciable variations in the infrared radiance. The variation in species concentrations which result from variations in the temperature-height profiles at

1. COSPAR (1972) Committee on Space Research, CIRA 72, Cospar International Reference Atmosphere. Akademie-Verlag, Berlin.
2. Jacchia, L. G. (1977) Thermospheric Temperature, Density and Composition: New Models, SAO Special Report No. 375.
3. COESA (1976) Committee on Extension to the Standard Atmosphere, U.S. Standard Atmosphere Supplements, 1966, U.S. Government Printing Office, Washington, D. C.

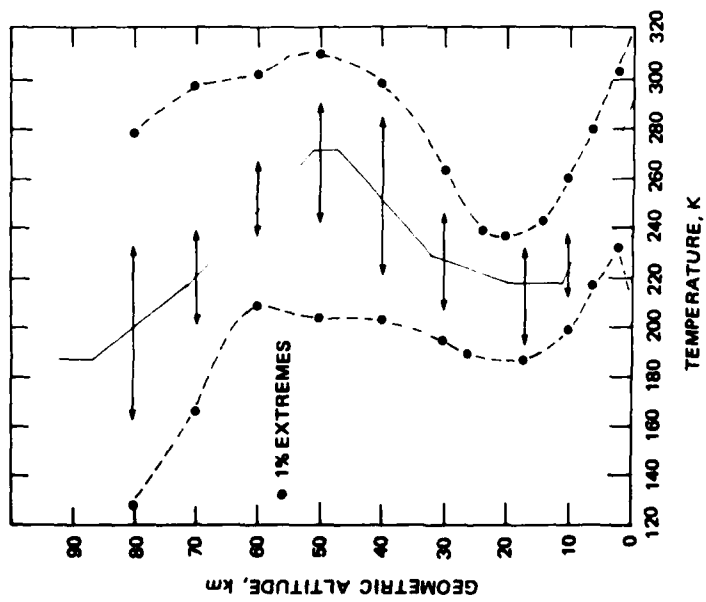


Figure 1. Range of Systematic Variability of Temperature Around the USSA 76 (COESA, 1976³)

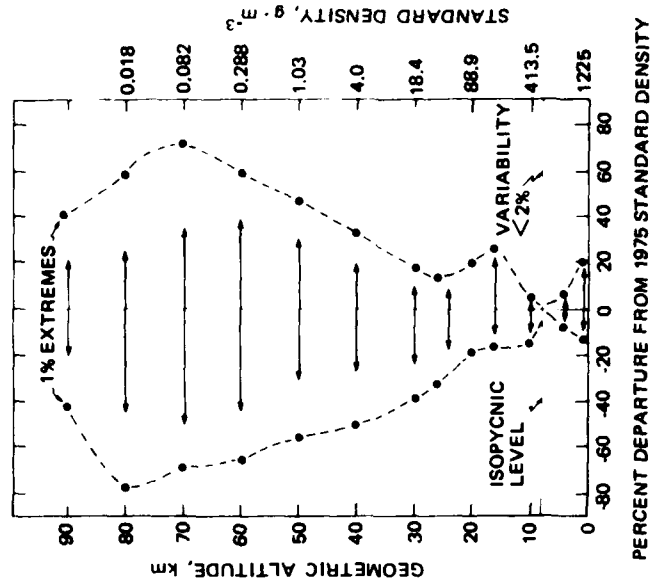


Figure 2. Range of Systematic Variability of Density Around the USSA 76 (COESA, 1976³)

altitudes above 100 km for various degrees of solar and geomagnetic activity are also discussed in USSA 76.

2.3 Air Force Reference Atmospheres

Recently Cole and Kantor (1978)⁴ published reference atmospheres that provide seasonal, latitudinal, and day-to-day variability of the thermodynamic properties of the atmosphere up to an altitude of 90 km. These models expand upon and update information contained in the USSA 76 (COESA, 1976³). Cole and Kantor⁴ present sets of mean monthly reference atmospheres describing seasonal changes in the vertical distributions of temperature, density, and pressure for 15° intervals of latitude between the equator and pole. In addition, they present estimates of the day-to-day variations around the monthly median values of temperature and density. Figure 3 displays the latitudinal variations in average monthly temperature for the months of January and July. From these temperature profiles density profiles can be constructed using the barometric equation. The results of this calculation show density variations similar to those shown in Figure 2.

In arctic and subarctic regions, sudden warmings and coolings of the winter stratosphere and mesosphere produce large changes in the vertical and horizontal structure of the atmosphere, both in the magnitude and in the altitude region of the temperature and density fluctuations. The day-to-day variations in temperature are in some cases as great or greater than the seasonal or latitudinal changes. Although warmings and coolings occur throughout the arctic and subarctic regions, the largest changes generally occur between latitudes 60° and 75°.

2.4 MSIS

The MSIS model (Hedin et al, 1977a,⁵ 1977b⁶) is a global thermospheric model that has been constructed from measurements of the density of N₂ with mass spectrometers on five satellites (AE-B, OGO 6, San Marco 3, Aeros A, and AE-C) and from neutral temperatures inferred from incoherent radar backscatter measurements at four ground stations (Arecibo, Jicamarca, Millstone Hill, and

4. Cole, A. E. and Kantor, A. J. (1978) Air Force Reference Atmospheres, AFGL-TR-78-0051, AD 058 505.
5. Hedin, A. E., Salah, J. E., Evans, J. V., Reber, C. A., Newton, G. P., Spencer, N. W., Kayser, D. C., Alcayde, D., Bauer, P., Cogger, L., and McClure, J. P. (1977a) A global thermospheric model based on mass spectrometer and incoherent scatter data, MSIS 1, N₂ density and temperature, J. Geophys. Res. 82:2139-2147.
6. Hedin, A. E., Reber, C. A., Newton, G. P., Spencer, N. W., Brinton, H. C., and Mayr, H. G. (1977b) A global thermospheric model based on mass spectrometer and incoherent scatter data, MSIS 2, Composition, J. Geophys. Res. 82:2148-2156.

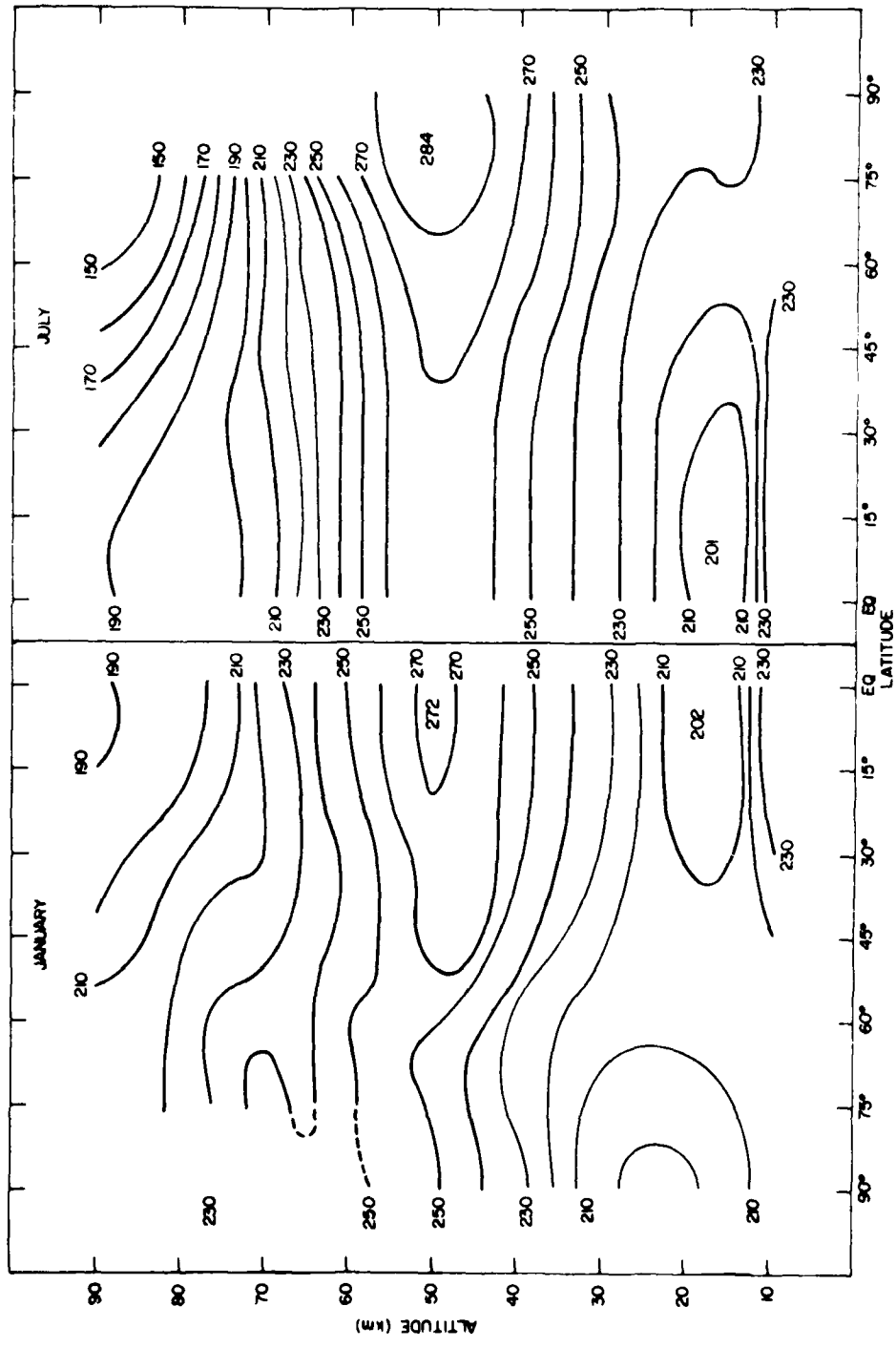


Figure 3. Latitudinal Temperature-height Cross Sections of Monthly Temperatures for January and July (Cole and Kantor, 1978⁴)

St. Santin). The satellite and ground-based incoherent scatter measurements provide unique and complementary information on the structure of the thermosphere. In addition, the MSIS model combines measurements of the densities of O, He, and Ar from neutral-gas mass spectrometers on four satellites and inferred O₂ and H densities from an ion mass spectrometer on the AE-C satellite with the neutral temperature and N₂ density models to produce a global model of thermospheric composition in terms of inferred variations at 120 km. The overall data set of these measurements covers the time period from the end of 1965 to mid-1975. In MSIS the exospheric temperature and other quantities are represented by least squares fits to the data in spherical harmonic expansions. In 1979 the MSIS model was extended to include longitudinal and universal time (UT) variations in thermospheric neutral temperature and composition (Hedin et al, 1979⁷). Terms that depend only on longitude indicate a temperature enhancement at 120 km of about 30°K at a latitude of approximately 70° along the longitude of the magnetic poles. As with the variations with magnetic activity, the extrapolated 120 km variations are generally in phase with temperature variations for N₂, Ar, and O₂ and out-of-phase for He, O, and H. The combined longitude and UT variations reflect the influence of the earth's magnetic field and suggest that the primary variations may be simply represented in magnetic coordinates.

The MSIS model is most representative of magnetically quiet conditions with the best data coverage between altitudes 200 and 600 km and with solar F_{10.7} indices between 75 and 180. The species concentrations should be reasonably valid above 150 km, but below 150 km they are essentially extrapolations from higher altitudes. Temperatures below 200 km may not adequately represent diurnal and semidiurnal variations. The limitations on altitudes make the application of the MSIS model to the calculation of limb viewing infrared calculations very difficult. In addition, the use of spherical harmonic construction of this model make it difficult to join to the lower altitude atmospheric models.

2.5 Jacchia 77 (J77)

The Smithsonian Astronomical Observatory models (Jacchia, 1977²) that describe the thermospheric temperature, density, and composition consist of essentially two parts: 1) the basic static models, that give temperature and density profiles of the atmospheric constituents for any specified exospheric temperature and 2) a set of formulae for correcting the exospheric temperature based on various types of thermospheric variation.

7. Hedin, A.E., Reber, C.A., Spencer, N.W., Brinton, H.C. and Kayser, D.C. (1979) Global model of longitude/UT variations in thermospheric composition and temperature based on mass spectrometer data, J. Geophys. Res. 84:1-9.

The Jacchia models are based primarily on a very large number of satellite drag measurements and on composition measurements from several satellites, OGO-6, ESRO 4, and S3-1. For the basic static models, tables of temperature, species concentrations, pressure and mass density are given for altitudes from 90 to 2500 km and for exospheric temperatures from 500 to 2600 K. The temperature profiles start from a constant value of 188 K at an altitude of 90 km, rise to an inflection point of 125 km, and become asymptotic to an "exospheric" temperature at approximately 500 km. Examples of the resultant temperature profiles are shown in Figure 4. The mass density is assumed to have a constant value of $3.43 \times 10^{-6} \text{ kg/m}^3$ at the altitude of 90 km. The atmosphere is assumed to be composed of N_2 , O_2 , O, Ar, He, and H with constant mixing ratios up to 100 km and with abundances determined by diffusive processes above this height. Number density profiles of the major atmospheric species for two exosphere temperatures are illustrated in Figure 5. The assumption of fixed boundary conditions at 90 km can lead to discontinuities in the density and temperature profiles if the Jacchia model is joined to atmospheric models that describe the mesosphere. Indications of the possible density variability and temperature variability at 90 km are shown in Figures 1, 2, and 3.

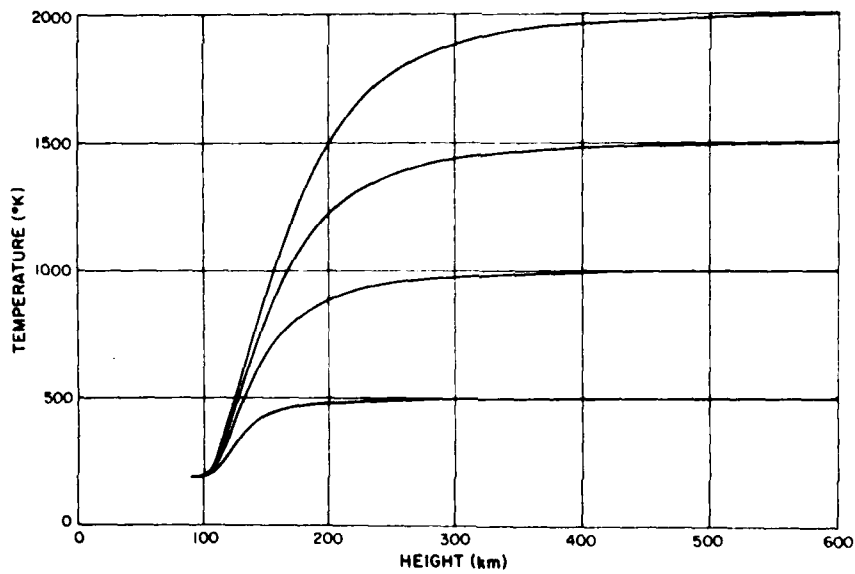


Figure 4. Four Temperature Profiles from the J77 Model (Jacchia, 1977²)

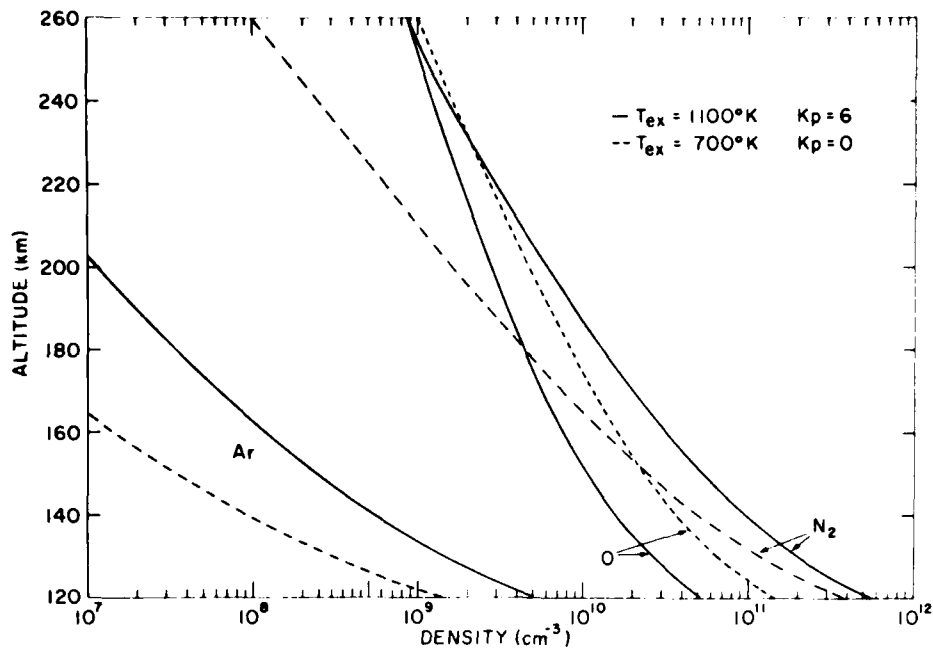


Figure 5. Variations of Atmospheric Species Concentrations at 78° Latitude as Predicted by J77 Model Under Two Conditions of Geomagnetic Activity and Exospheric Temperature

The types of variation that the J77 models attempt to represent can be classified as follows:

1. Variation with solar cycle
2. Variation with changes in activity on the disk of the sun
3. The daily or diurnal variation
4. Variations with geomagnetic activity
5. Seasonal-latitudinal variations
6. The semiannual variation

All these variations are based on parameters that can be predicted with varying degrees of accuracy or can be obtained from observational data. Such static models should be quite adequate to describe the mean conditions when the characteristic time of the variation is much longer than the time scale of conduction, convection, and diffusion processes. The following paragraphs describe how the above variations are incorporated by Jacchia.

The magnitude of the variation of the exospheric temperature is represented as a function of both the instantaneous value of the 10.7-cm solar flux F and the flux averaged over a few solar rotations \bar{F} . The variation of exospheric

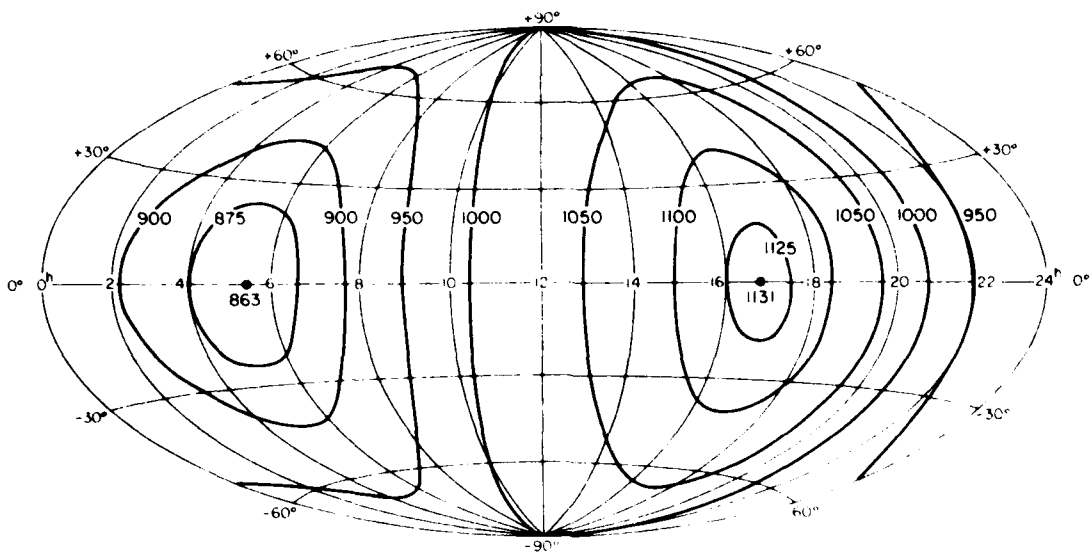
temperature is applied with a time lag that varies from 0.9 days at noon local solar time (LST) to 1.6 days at midnight LST.

The diurnal variation of the exospheric temperature is represented as the sum of two terms, one representing a seasonal-latitudinal variation that is independent of local time and another that is a function of local time. The seasonal-latitudinal (or annual) variation has a maximum value of 15 percent at the poles and is proportional to the declination of the sun and to the sine of the latitude. In Figure 6 the resulting variations of exospheric temperature at the equinoxes and the June solstice are shown for quiet magnetic conditions ($K_p = 0$). This global variation of exospheric temperature, in conjunction with the resulting variation in species concentrations, can produce a variation in the global infrared emission. Examples of such variations are shown in Chapter 4.

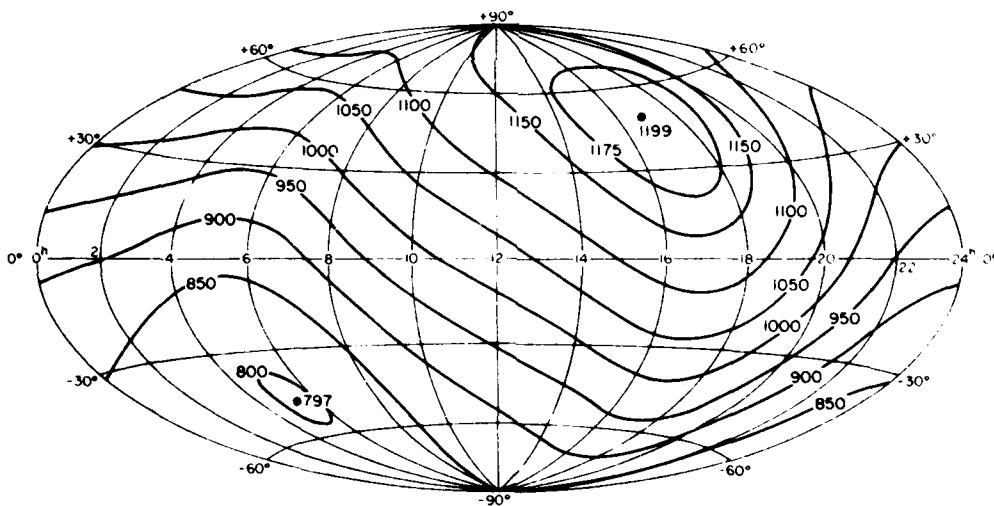
The variation with geomagnetic activity is represented as a temperature increase that is a function of the geomagnetic latitude and the K_p index. The accompanying variation in species concentrations is comprised of three separate components: a thermal component due to the change in scale height induced by the change in temperature, a component due to the change in the altitude of the homopause (the interface between the regimes of mixing and diffusion), and a component due to the "equatorial wave" that results from a density enhancement resulting from convection toward the equator. An example of the resulting change in exospheric temperature is shown in Figure 7, where it is seen that the temperature at the higher latitudes can be significantly changed by magnetic activity. The effective change in the altitude of the homopause included in the model is shown in Figure 8 as a function of K_p for various geomagnetic latitudes. The density variations of four atmospheric constituents as a function of the invariant magnetic latitude for a $K_p = 5$ are shown in Figure 9. The effect of the geomagnetic correction to the J77 model is also shown in the profiles presented in Figure 5.

A recent modification of the J77 model (Philbrick and Gardner, 1980^b) predicts the nighttime altitude profile of CO_2 as a function of latitude and geomagnetic activity. In Figure 10 the variation in this important infrared contributor is shown for low and high latitudes and for a range of geomagnetic activity. These results suggest that particularly significant variations in the infrared radiation from CO_2 may occur with the variation in geomagnetic activity. Calculations of the radiation from CO_2 presented in Chapter 4 demonstrate this effect.

8. Philbrick, C. R. and Gardner, M. E. (1980) Private communication.



a) EQUINOXES



b) JUNE SOLSTICE

Figure 6. Global Distribution of the Exospheric Temperature for Quiet Geomagnetic Conditions ($K_p = 0$). The coordinates are local solar time and geographic latitude (Jacchia 1977²)

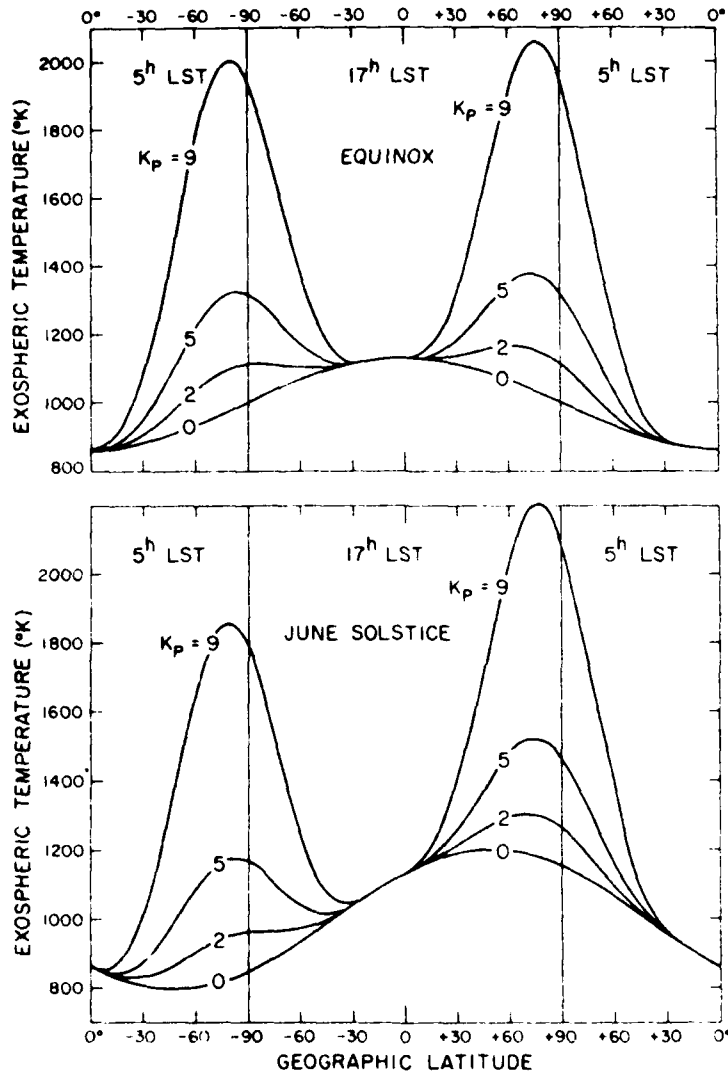


Figure 7. Exospheric Temperature Profiles Along the Complete (360°) Meridional Circle Along Which the Local Solar Time is 17^h in One Hemisphere and 5^h in the Other, for Various Levels of Geomagnetic Activity. Even a moderate level of activity ($K_p \approx 2$) has the effect of shifting the temperature maximum from the equator to the poles at the time of equinoxes (Jacchia, 1977²).

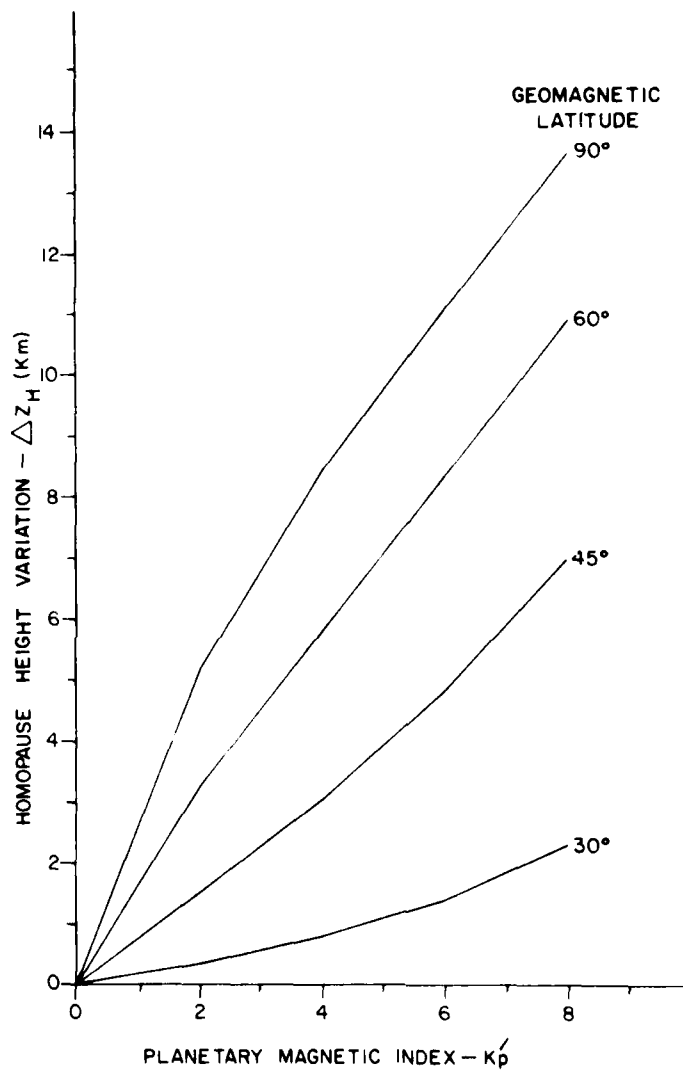


Figure 8. Homopause Height Variation vs K_p for Several Geomagnetic Latitudes (J77 Model)

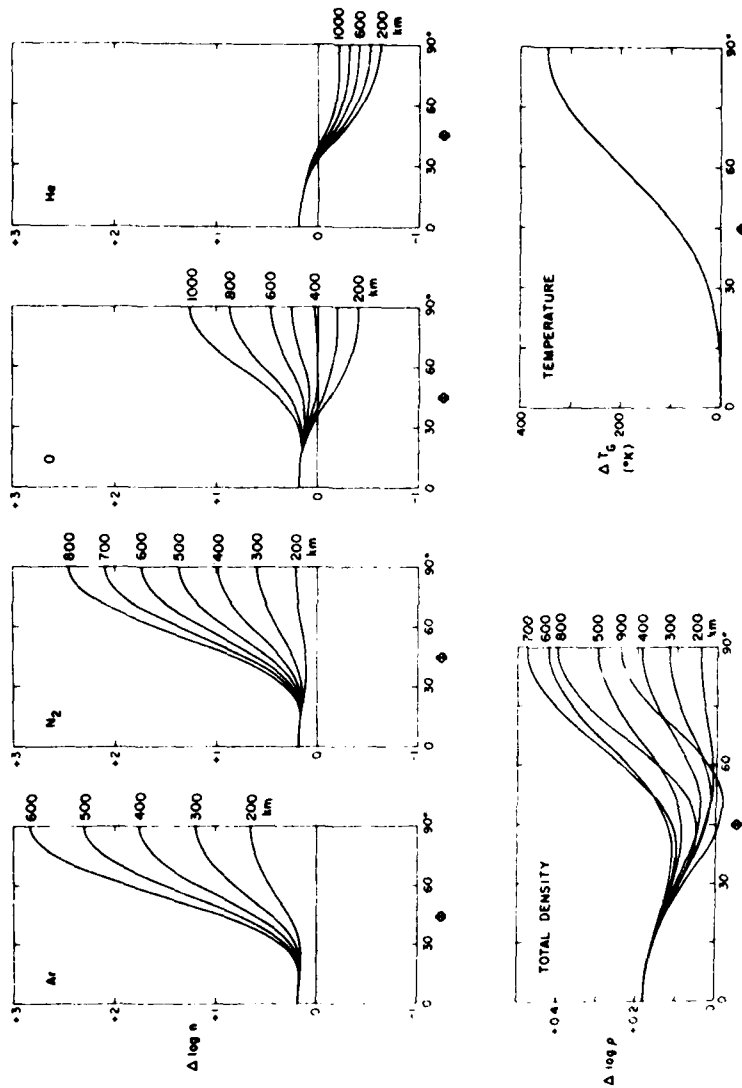


Figure 9. The Density Variation of Four Atmospheric Constituents as a Function of the Invariant Latitude ϕ , for Various Heights When the Geomagnetic Index $K_p = 5$. The curves were computed using a "quiet" ($K_p = 0$) exospheric temperature of 900 K. The diagram in the lower left corner depicts the variation of the total density; that in the lower right corner gives the corresponding variation in the exospheric temperature (Jacchia, 19772)

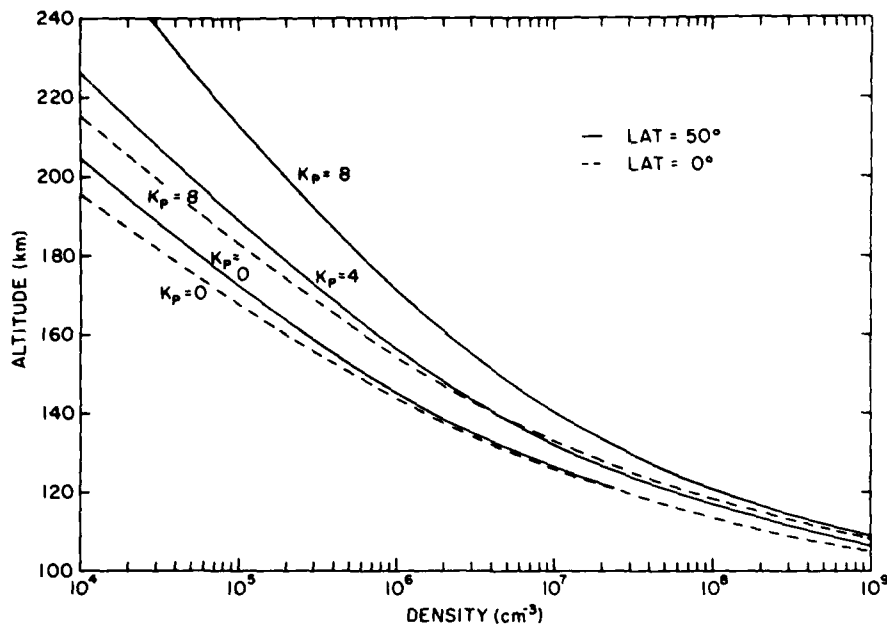


Figure 10. CO₂ Atmospheric Density Predictions Based on the Jacchia Model at Latitudes of 0° and 50° for Nighttime Conditions

3. ATMOSPHERIC MEASUREMENTS COMPARED WITH MODELS

Various measurements have been compared to the predictions of the above models. These comparisons show that the J77 and MSIS models are in general agreement. However, neither provides a completely satisfactory representation of the atmosphere. For example, in Figure 11 altitude profiles of N₂, Ar, O, and O₂ number densities measured during the Aladdin 74 program (Trinks et al, 1978⁹) are compared to the predictions of the J77 and MSIS models. The dip in the densities by a factor of 3 to 5 at 112.5 km is indicative of the variations in the lowest part of the thermosphere. Trinks et al⁹ suggested that this variation could be the superposition of a semidiurnal tidal wave and a gravity wave. This proposition was supported by the temperature-height profile obtained from incoherent-scatter radar measurements.

Figures 12 and 13 show the comparison of model prediction and measurements at higher altitudes. Predictions of the N₂, O, and Ar density models using the J77 and MSIS are compared to measurements made with the S3-1 satellite

9. Trinks, H. and Fricke, K. H. (1978) Carbon dioxide concentrations in the lower thermosphere, J. Geophys. Res. 83:3883-3886.

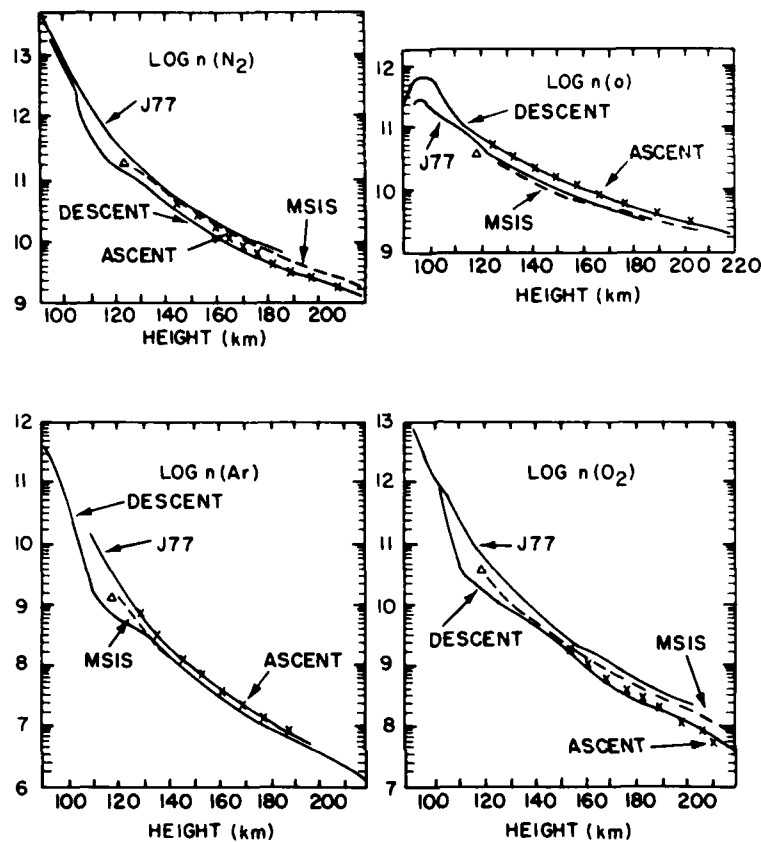


Figure 11. Density-height Profiles of N_2 , Ar, O, and O_2 . The dots and heavy solid curves represent the descent data; the ascent data are given by the dashed curves. The number densities are in units per cm^3 and on a logarithmic scale. Also shown are the predictions of the Jacchia 77 model (J77) and the MSIS model (Hedin, et al, 1977a,⁵ 1977b⁶); the triangles denote rocket averages (Offerman, 1974¹⁰), (Trinks et al, 1978⁹)

(Philbrick and Gardner 1980⁸) for both magnetically quiet and disturbed conditions. The differences between the models and the data show that, while general agreement exists, the observed small-scale variations of the densities are not modeled. It is also evident from these two typical cases that, during a period of higher geomagnetic activity, such as shown in Figure 13, significantly more structure is observed in the profiles.

10. Offerman, D. (1974) Composition variations in the lower thermosphere, *J. Geophys. Res.* 79:4281-4293.

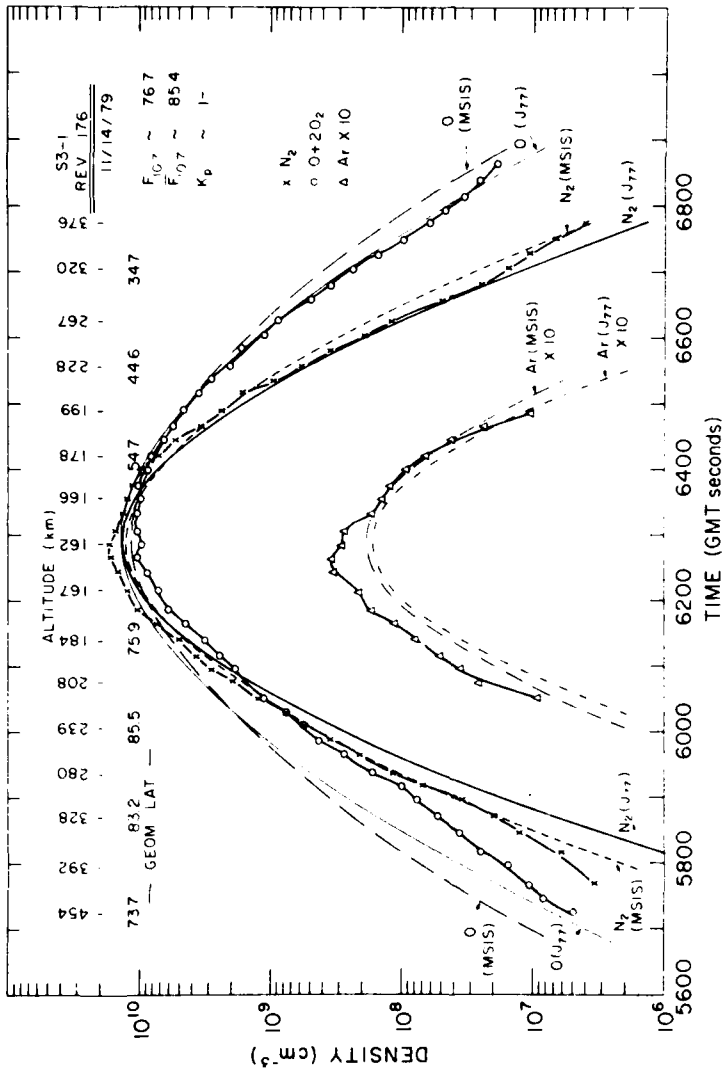


Figure 12. Comparison of Predictions of J77 and MSIS Models for N₂, O, and Ar With Measurement Made During S3-1 Satellite Flight Under Magnetically Quiet Conditions

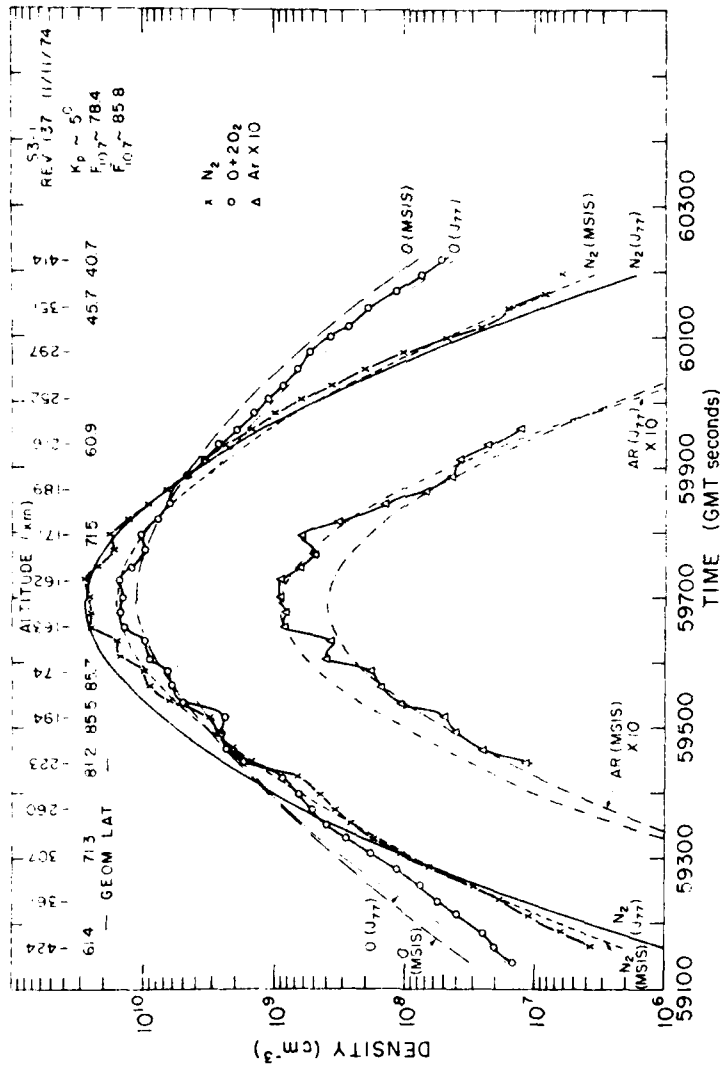


Figure 13. Comparison of Predictions of J77 and MSIS Models for N_2 , O, and Ar With Measurements Made During S3-1 Satellite Flight Under Magnetically Disturbed Conditions

4. GEOMAGNETIC INDUCED VARIATIONS OF SPECIES CONCENTRATIONS

The influence of geomagnetic activity on the upper atmospheric species densities is even stronger than it is upon the total mass density. This effect is due to the difference in diffusion velocities of the various species and results in depletions of those species with mass lighter than the mean molecular weight (see, for example, the predictions of the Jacchia 77 model in Figures 5 and 10). Figure 13 shows that disturbed magnetic conditions ($K_p = 6^+$) can greatly increase N_2 density, Ar density, and the structure in the density profiles.

In Figure 14 the correlation of species concentrations with geomagnetic activity is studied further. It is seen that the Ar/ N_2 ratio, as well as the total density, is strongly correlated with the level of geomagnetic activity. The Ar density is highly correlated with the level of geomagnetic activity whereas, the O density appears to have a weak negative correlation with K_p , about 30 percent change in this case. The large increase in Ar density with K_p is shown further in Figure 15, where measurements made by the S3-1 satellite are plotted versus geomagnetic latitude for two ranges of K_p , $0 \leq K_p \leq 2^+$ and $4 \leq K_p \leq 6^+$. The dependence on geomagnetic activity of CO_2 is expected to be similar to that of Ar due to the nearly equal atomic masses. Thus, the effect of increased geomagnetic activity upon atmospheric infrared radiance should be very important. The influence of photochemical processes on this connection is considered in the next section.

In Figure 16 estimates of the frequency of occurrence of high magnetic activity and of the duration of such increases are shown. These estimates are from the work of Pazick (1976).¹¹ He presented tables of probabilities of geomagnetic activity. In particular, these results indicate that approximately one-sixth of the time K_p will exceed 4 and approximately one-half these disturbances will last longer than one day.

5. VARIATIONS IN CONCENTRATIONS OF THE MINOR ATMOSPHERIC SPECIES

Direct measurements of the minor atmospheric species have been carried out from rocketborne platforms. The results of these measurements make it possible to draw some conclusions concerning the overall variability of the minor species, but few conclusions can be drawn concerning the time dependence of these variations.

11. Pazick, P. M. (1976) Conditional Probabilities of the Geomagnetic Index A_p , AFGRL-TR-76-0034, AD A023 675.

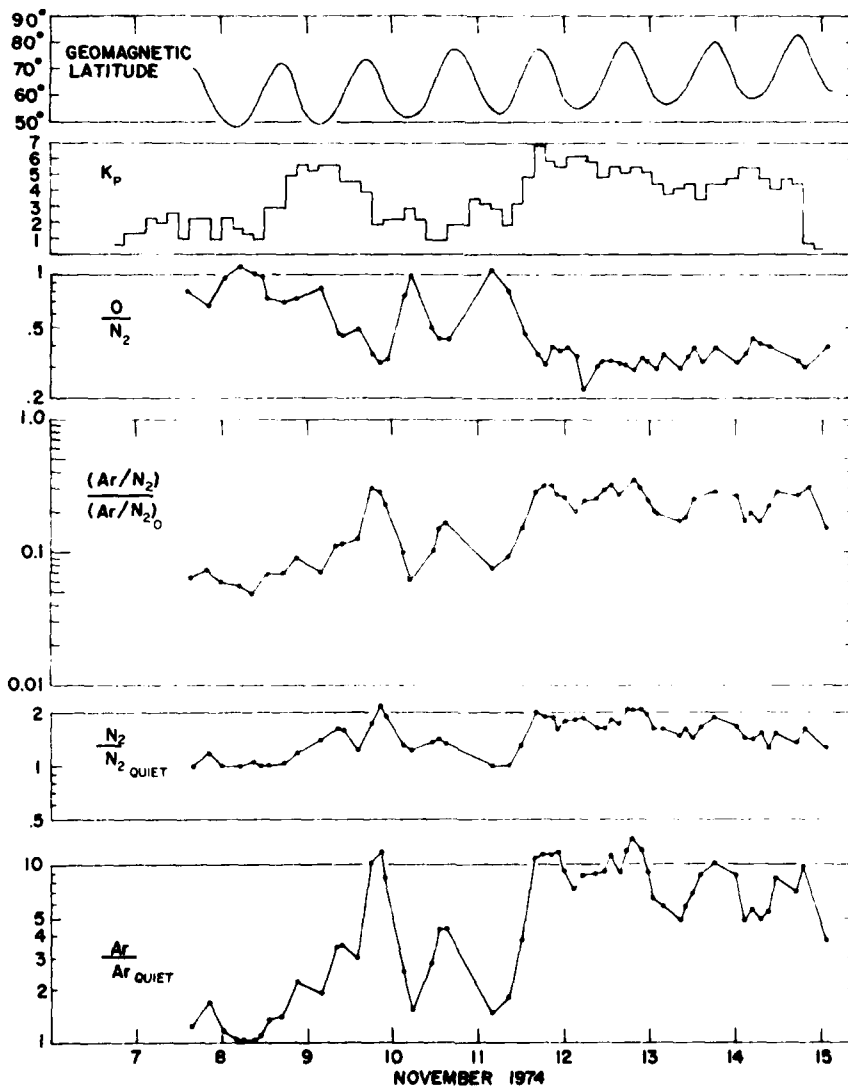


Figure 14. Correlation of Species Concentration at an Altitude of 160 km With Geomagnetic Activity During a Magnetic Storm from 7 November to 15 November 1974

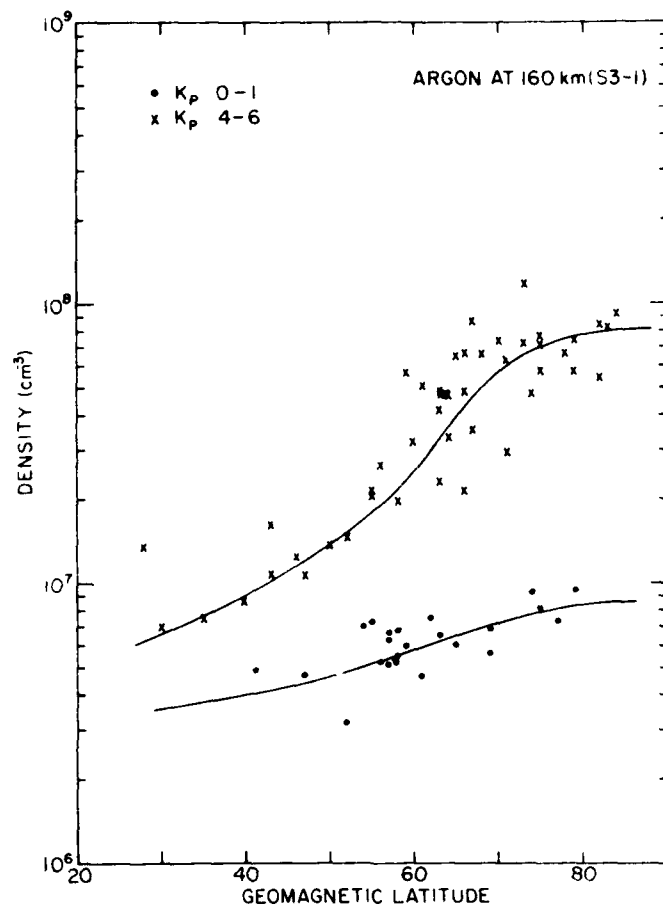


Figure 15. Ar Density at an Altitude of 160 km as a Function of Geomagnetic Latitude for Quiet and Disturbed Magnetic Conditions

Measurements of the density of CO₂ by mass spectrometer (Philbrick et al, 1973¹²) have shown that CO₂ is mixed in its ground level ratio between 85 and 100 km. Measurements of the CO₂ density above the turbopause were performed at night in 1973 by Offermann and Grossman (1973)¹³ and during the day in 1974

12. Philbrick, C. R., Faucher, G. A. and Trzcinski, E. (1973) Rocket measurements of mesospheric and lower thermospheric composition, Space Research XIII:255-260.
13. Offerman, D. and Grossman, K. U. (1973) Thermospheric density and composition as determined by a mass spectrometer with cryo ion source, J. Geophys. Res. 78:8296-8304.

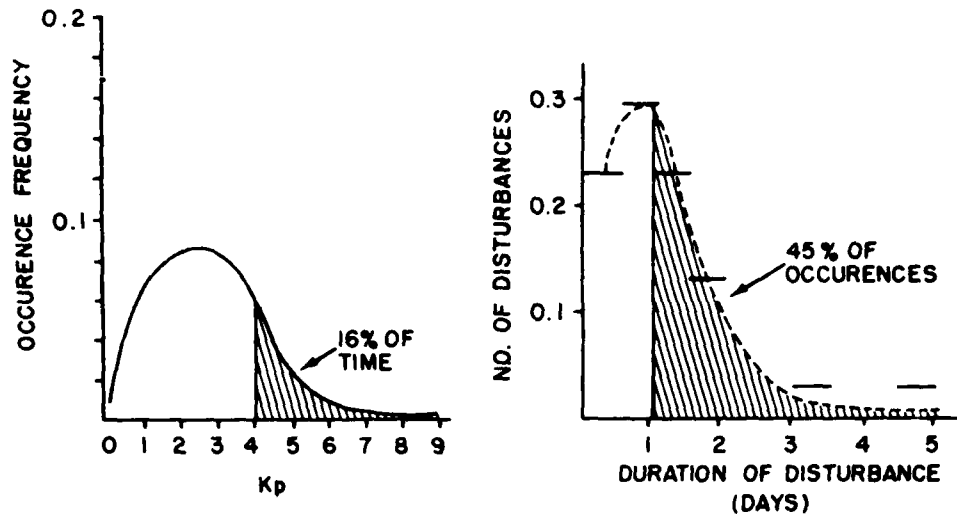


Figure 16. Summary of Disturbed Atmosphere Frequency or Occurrence (geomagnetic disturbances only) for Solar Maximum Years

by Trinks and Fricke (1978).⁹ In Figure 17, these results are plotted as ratios to the Ar density. At night it is found that the CO_2/Ar ratio follows the expected diffusive equilibrium profile, while during the day the ratio decreases from the diffusive profile by a factor of about 3 at 140 km. This result is in agreement with the loss of CO_2 by solar dissociation and reaction with O^+ ions. The fact that the CO_2 density responds in a similar way to the Ar density makes it possible to infer the behavior of fluctuations in the CO_2 density from measurements of the fluctuations in the Ar density, especially at higher altitudes.

A midlatitude model of the ozone density constructed by A. J. Kruger and R. A. Minzner¹⁴ was presented in USSA 76. Figure 18 (a and b) shows the resultant O_3 concentration, as well as the O_3 mass mixing ratio. Expected variations of the density and mixing ratio of O_3 are also shown in these figures. From Figure 18 (a) it is seen that at high altitude the O_3 concentration varies by as much as a factor of three. During the Aladdin program in 1974, measurements of the O_3 density (Weeks et al, 1978¹⁵) were made at altitudes from 19 to 108 km using four different techniques. Results of these measurements are shown in Figure 19 (a, b, and c) for three separate altitude regions. These results are in basic

14. Kruger, A. J. and Minzner, R. A. (1976) A midlatitude ozone model for the 1976 U.S. standard atmosphere, *J. Geophys. Res.* 81:4477-4481.
15. Weeks, L. H., Good, R. E., Randhawa, J. S. and Trinks, H. (1978) Ozone measurements in the stratosphere, mesosphere, and lower thermosphere during Aladdin 74, *J. Geophys. Res.* 83:978-982.

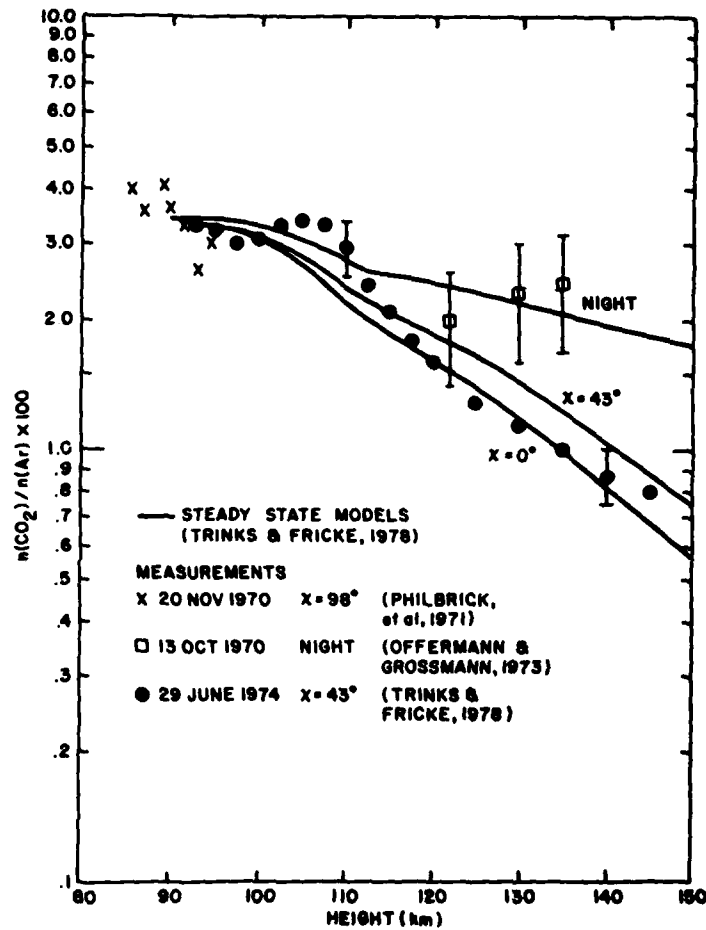
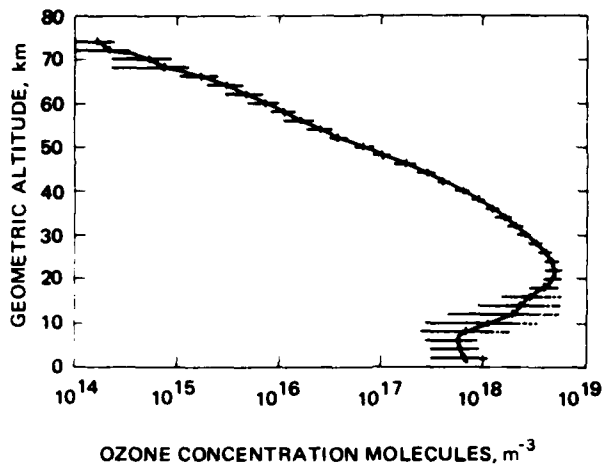


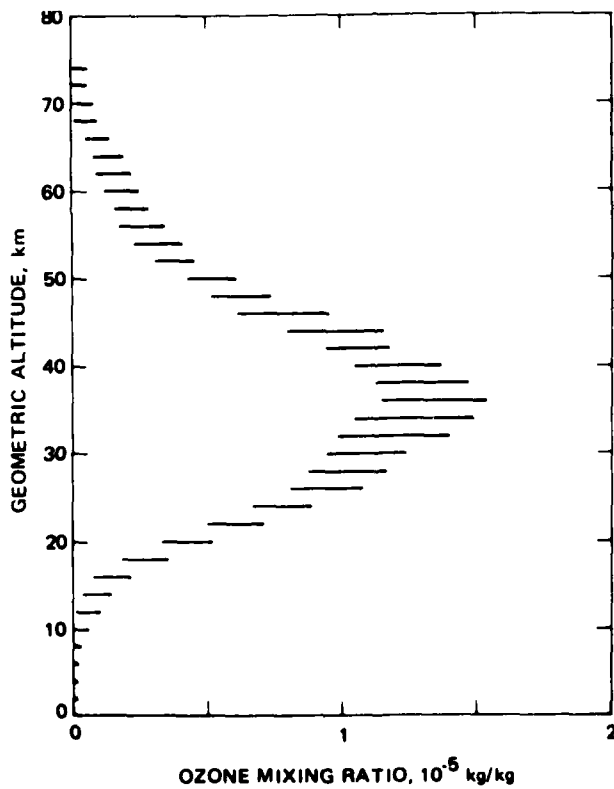
Figure 17. Calculated and Measured $n(\text{CO}_2/n(\text{Ar})$ Ratio for Two Background Atmospheres and Three Solar Zenith Angles. Data are from Trinks and Fricke (1978)⁹ (solid circles), Offermann and Grossmann (1973)¹³ (squares) and from Philbrick et al. (1971).¹⁶ [Source - Trinks and Fricke (1978)⁹]

agreement with the model presented in Figure 18 (a and b). In Figures 19 (a, b, and c) these results are also compared to other models of the O₃ density. These measurements reveal a structured density profile at altitudes above 75 km, particularly for measurements made with the airglow photometer. These variations

16. Philbrick, C. R., Faucher, G. A., and Wlodyka, R. A. (1971) Neutral Composition Measurements of the Mesosphere and Lower Thermosphere, AFCRL-71-0602, AD 739169.



(a) Density as a Function of Height



(b) Mixing Ratio as a Function of Height

Figure 18. Midlatitude Ozone Model (COESA, 1976³)

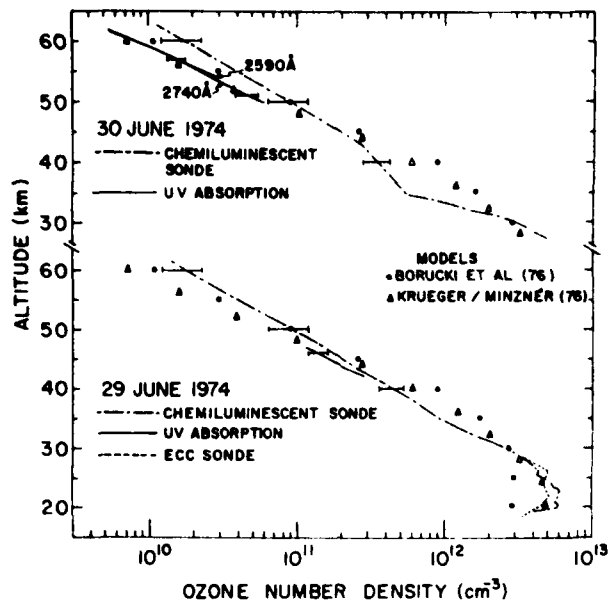


Figure 19a. Chemiluminescent Sonde O₃ Data Compared With UV Results, ECC Sonde, and Models (Weeks et al, 1978¹⁵)

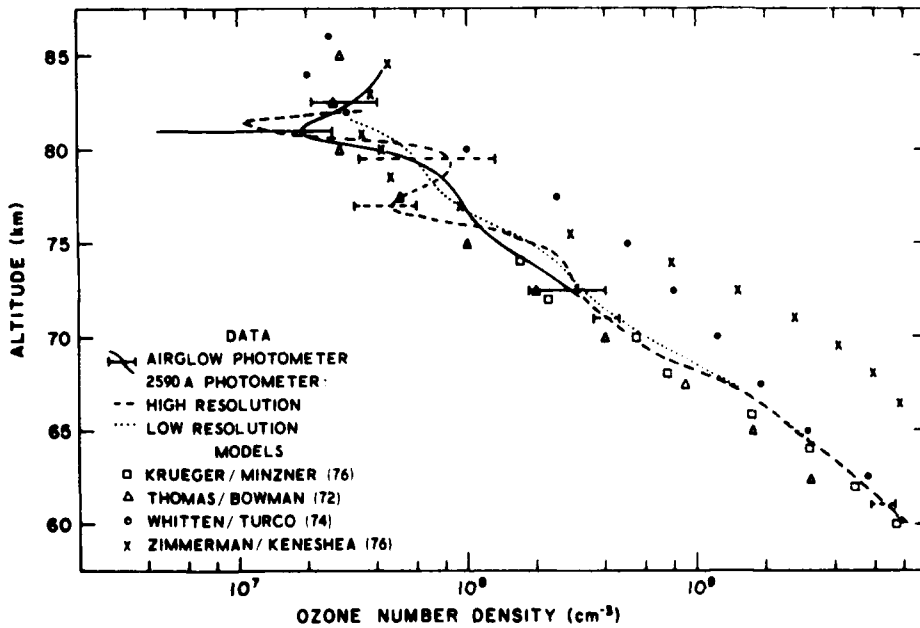


Figure 19b. Comparison of UV and Airglow Techniques for O₃ Determination (Weeks et al, 1978¹⁵)

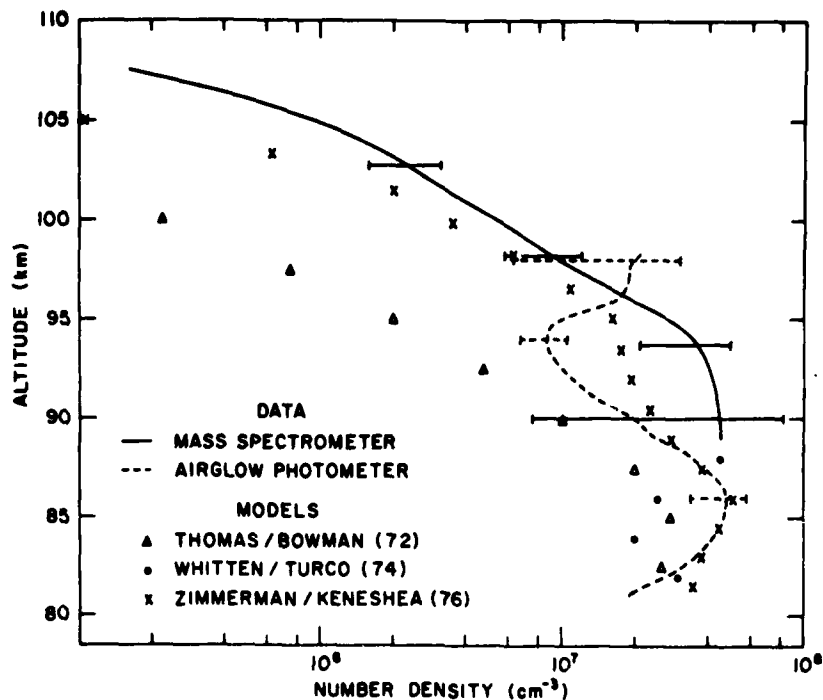


Figure 19c. Comparison of Airglow and Mass Spectrometer Results for O₃ Determination With Some Typical Models (Weeks et al, 1978¹⁵)

appear to have similar scale sizes and amplitudes as those found in the atomic oxygen profiles that are discussed in Chapter 5.

Using resonantly scattered light from thermospheric NO, measurements made aboard the Atmosphere Explorer C satellite have been used to study the dependence of the NO density on latitude, longitude, and magnetic activity. These results have been analyzed by T. E. Cravens and A. I. Stewart (1978)¹⁷ to determine the NO density at an altitude of 105 km. They find that near the equator the density at the peak of the NO concentration is about $2 \times 10^7 \text{ cm}^{-3}$ and varies little with longitude or magnetic activity, except during major geomagnetic storms. As shown in Figure 20, the peak NO densities are typically two to three times larger and more variable at higher latitudes. Cravens and Stewart¹⁷ found an increase in the NO density of as much as 30 percent at a latitude of 40°N and S. In addition to these effects, they found that the NO density at these latitudes doubles during times of high geomagnetic activity at ($K \approx 6$). They also studied the

17. Cravens, T. E. and Stewart, A. I. (1978) Global morphology of nitric oxide in the lower E region, *J. Geophys. Res.* 83:2446-2452.

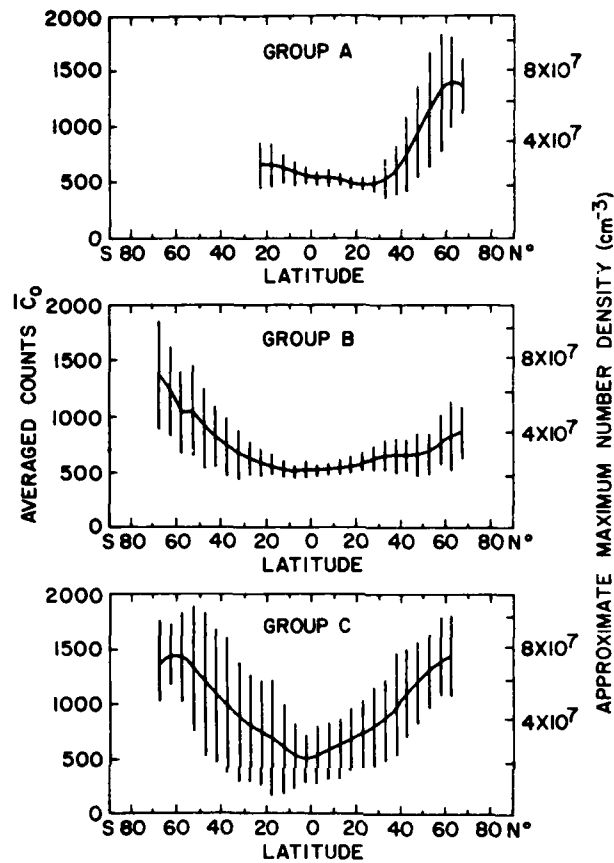


Figure 20. NO Signal from 105 km Zonally Averaged for Each of the Three Orbit Groups as Functions of Latitude. The bars are standard deviations

diurnal and seasonal effects at low latitudes and found that NO increases at the equator by a factor of 2 between sunrise and early afternoon with a small decline near sunset and that the density of NO is higher during the summer than during the winter.

References

1. COSPAR (1972) Committee on Space Research, CIRA 72, Cospar International Reference Atmosphere. Akademie-Verlag, Berlin.
2. Jacchia, L.G. (1977) Thermospheric Temperature, Density and Composition: New Models, SAO Special Report No. 375.
3. COESA (1976) Committee on Extension to the Standard Atmosphere, U.S. Standard Atmosphere Supplements, 1966, U.S. Government Printing Office, Washington, D.C.
4. Cole, A.E. and Kantor, A.J. (1978) Air Force Reference Atmospheres. AFGL-TR-78-0051, AD 058 505.
5. Hedin, A.E., Solah, J.E., Evans, J.V., Reber, C.A., Newton, G.P., Spencer, N.W., Kayser, D.C., Alcayde, D., Bauer, P., Cogger, I. and McClure, J.P. (1977a) A global thermospheric model based on mass spectrometer and incoherent scatter data, MSIS1, N₂ density and temperature, J. Geophys. Res. 82:2139-2147.
6. Hedin, A.E., Reber, C.A., Newton, G.P., Spencer, N.W., Brinton, H.C. and Mayr, H.G. (1977b) A global thermospheric model based on mass spectrometer and incoherent scatter data, MSIS2, Composition, J. Geophys. Res. 82:2148-2156.
7. Hedin, A.E., Reber, C.A., Spencer, N.W., Brinton, H.C. and Kayser, D.C. (1979) Global model of longitude/UT variations in thermospheric composition and temperature based on mass spectrometer data, J. Geophys. Res. 84:1-9.
8. Philbrick, C.R. and Gardner, M.E. (1980) Private communication.
9. Trinks, H. and Fricke, K.H. (1978) Carbon dioxide concentrations in the lower thermosphere, J. Geophys. Res. 83:3883-3886.
10. Offerman, D. (1974) Composition variations in the lower thermosphere, J. Geophys. Res. 79:4281-4293.
11. Pazick, P.M. (1976) Conditional Probabilities of the Geomagnetic Index A_p, AFGL-TR-76-0034, AD A023 675.
12. Philbrick, C.R., Faucher, G.A. and Trzeinski, E. (1973) Rocket measurements of mesospheric and lower thermospheric composition, Space Research XIII:255-260.
13. Offerman, D. and Grossman, K.U. (1973) Thermospheric density and composition as determined by a mass spectrometer with cryo ion source, J. Geophys. Res. 78:8296-8304.
14. Kruger, A.J. and Minzner, R.A. (1976) A midlatitude ozone model for the 1976 U.S. standard atmosphere, J. Geophys. Res. 81:4477-4481.
15. Weeks, L.H., Good, R.E., Randhawa, J.S. and Trinks, H. (1978) Ozone measurements in the stratosphere, mesosphere, and lower thermosphere during Aladdin 74, J. Geophys. Res. 83:978-982.
16. Philbrick, C.R., Faucher, G.A., and Wlodyka, R.A. (1971) Neutral Composition Measurements of the Mesosphere and Lower Thermosphere, AFCRL-71-0602, AD 739169.
17. Cravens, T.E. and Stewart, A.I. (1978) Global morphology of nitric oxide in the lower E region, J. Geophys. Res. 83:2446-2452.

4. Effects of Atmospheric Variability on Infrared Radiance Prediction

T.C. Degges
Visidyne, Inc.
Burlington, Mass.

The infrared radiance model described in Chapter 2 accepts as input data, molecular concentrations, and temperatures at fixed altitudes. The computed radiances depend on the altitude profiles of species concentrations and temperature. Variability in the predicted radiances results from the variability in these atmospheric properties due to changing geophysical conditions. In this chapter we present some preliminary results that show the effects on the infrared radiance of atmospheric variations as described in Chapter 3.

For a radiator such as CO_2 , which is chemically stable except for photodissociation by far ultraviolet sunlight at high altitudes and by ion-molecule reactions with O^+ in the E and F region, temperature is the controlling factor in radiance calculations below 100 km. Above 100 km, where other factors influence concentrations, it is still the radiation received from lower altitudes and the sun that controls the emitted infrared. Given the surface pressure and concentration, the atmospheric temperature profiles determine total atmospheric density and hence CO_2 concentrations. Up to 30 or 40 km, collisional excitation and deexcitation are sufficiently rapid to maintain vibrational levels of CO_2 in thermodynamic equilibrium and local temperatures determine the radiation field. Above 100 km, collisional energy exchange is much slower than radiation exchange. The radiation from the sun and lower atmosphere determines the radiation absorbed and emitted by each

molecule. Between 40 and 100 km, radiation and collisions compete in determining the IR emission. Thus, in this region, the entire temperature altitude profile may be necessary to compute radiation from molecules at a given altitude.

Some of the considerations outlined above are illustrated in Figure 1. This figure shows total band radiance in the CO_2 01101-00001 (or 0110 - 0000) $15.0 \mu\text{m}$ vibration-rotation band. Four different nighttime conditions are illustrated. Three of these use the Spring/Fall Midlatitude Model from the USSA 76 for altitudes below 120 km. The 600 K exospheric model, which represents quiet conditions near solar activity minimum, is further assumed to have a CO_2 homopause (or micropause) altitude of 100 km. The 2100 K exosphere models, typical of quiet conditions near solar activity maximum use homopause altitudes of 110 and 120 km. The fourth set uses a 60°N latitude January atmosphere below 120 km, with a 2100 K exospheric temperature atmosphere above 120 km. The homopause altitude is 120 km. Although the CO_2 density above 120 km for this set is less than that of the corresponding spring/fall model, radiance values are higher because the upper stratosphere is warmer in this mode and the "earthshine" effect (really "stratosphere shine" for this optically thick band) is stronger. The different radiance values for the spring/fall models are due almost entirely to differing CO_2 concentrations at high altitude. A change in homopause altitude from 110 to 120 km approximately doubles concentrations at higher altitudes, while varying exospheric temperatures produce much greater variations in concentrations and hence radiation.

The USSA 76 supplements provide a limited set of reference atmospheres for illustrating global and temporal changes in atmospheric conditions. This set has the advantage that consistent atmospheres are given from the ground up to 100 km. In matching the high altitude parts of the models with the low altitude parts there is no provision for possible temperature and concentration changes below 120 km when exospheric temperatures are varied. There is no provision for including the effects of magnetic activity (storms, ring current, etc.) on atmospheric density, composition, or temperature. As discussed in Chapter 3 the most up-to-date model atmospheres that incorporate such effects are the J77 and MSIS models. These have the disadvantage that they are limited to altitudes above 90 km and cannot be expected to be accurate models below about 140 km, the lower altitude limit for long-lived satellites, the ultimate source of the data used in constructing these models.

In the calculations discussed below, some of the problems inherent in matching the J77 Model to a lower altitude model have been avoided by selecting models from Cole and Kantor's 1978 Air Force Reference Atmospheres that agree closely with the J77 Model's 90 km boundary conditions. Most of the sample radiances have used the September 60°N latitude model, so that some of these calculations may

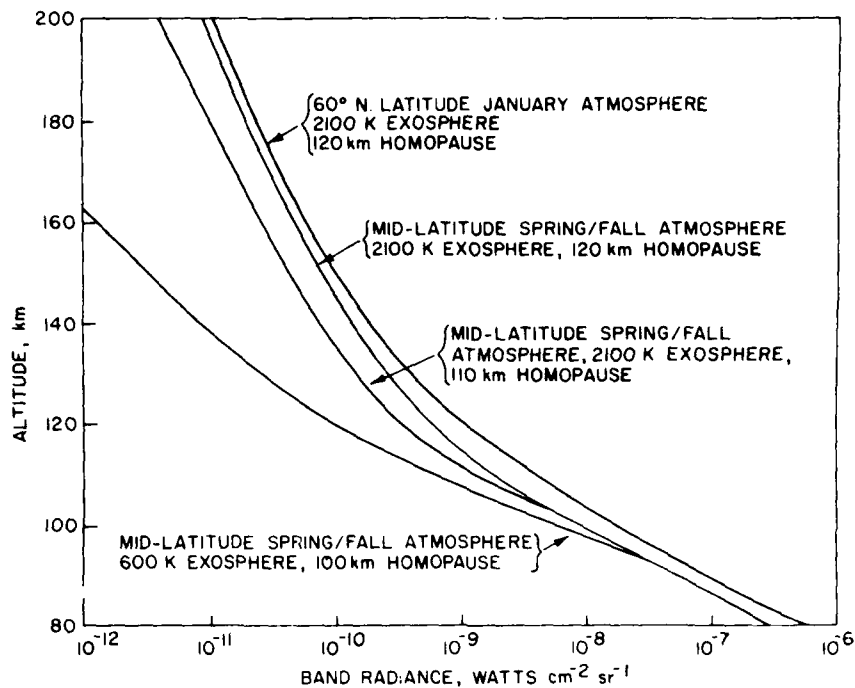


Figure 1. Vertical (upward) Viewing of Radiances in 01101-00001 CO₂ 15 μm Band for Typical Atmospheric Models

also be appropriate to analysis of the AFGL SPIRE probe data. The entire J77 model has not been used but the temperature was taken as the main input to the radiance model and integration is performed upward from the Air Force Reference Atmosphere (Cole and Kantor, 1978¹) to obtain densities. At 90 km, the total mass density from the 60° N latitude model is $3.33 \times 10^{-6} \text{ kg-m}^{-3}$ as compared with $3.43 \times 10^{-6} \text{ kg-m}^{-3}$ for the J77 density. In addition, the Jacchia model assumes a homopause at 100 km. Here the effective homopause level for carbon dioxide is taken as 110 km.

Eight daytime atmospheric conditions for altitudes above 90 km have been selected for use with the September 60° N Cole and Kantor model.¹ These conditions are summarized in Table 1.

The cases with solar flux 300 (the units of solar flux are $10^{-22} \text{ W m}^{-2} \text{ Hz}^{-1}$) were computed at 75° N latitude to obtain a larger effect from the magnetic

1. Cole, A. J. and Kantor, A. J. (1978) Air Force Reference Atmospheres, AFGL-1R-78-0051, AD A058 505.

Table 1. Atmospheric Conditions Used for Calculations of Infrared Radiances

Case	Solar Flux	K _p	Exospheric Temperature, K
A	50	0	626.5
B	100	0	880.3
C	150	0	1081.2
D	200	0	1255.0
E	250	0	1411.5
F	300	0	1555.7
G	300	5	1829.4
H	300	8	2176.8

disturbances. The 60° latitude low altitude model was used in all cases. Plots of band radiances presented here show only conditions A, C, F, G, and H.

The radiance from the three CO₂ bands with band center at 15.0 μm are added together in Figure 2. The 01101-00001 transition is the major contribution to the 15 μm bands and is optically thick in limb viewing up to a tangent height of about 110 km. For this transition the conditions with the warmest thermospheres have sufficiently more molecules at high altitudes so that their radiance values are noticeably higher at tangent heights as low as 60 km, although the composition is identical for all cases at altitudes below 90 km. The other bands do not have noticeable differences below tangent height 80 km. Figures 3 and 4 show total band radiances for the strongest offcenter vibrational-rotational bands included in the model that contribute to the CO₂ 15 μm band complex. Figures 5 through 7 show the spectral radiance from the 15 μm CO₂ bands at tangent heights 100, 140, and 200 km, with 2 percent spectral resolution. At 100 km the cases with no magnetic effects have almost identical radiance curves, while the cases with magnetic effects G and H are brighter.

Figure 8 shows the sum of three bands that radiate at 4.3 μm for cases A, C, F, G, and H. The 00011-00001 transition band is optically thick in limb viewing to about 120 km tangent height. The fluorescent bands are brighter than the fundamental between 60 and 100 km, but rapidly become less important at higher altitudes. Figures 9 through 11 present daytime spectra at 4.3 μm for tangent heights 100, 140, and 200 km. As was the case at 15 μm, the cases without magnetic disturbances are very close together at 100 km tangent height. At higher altitudes

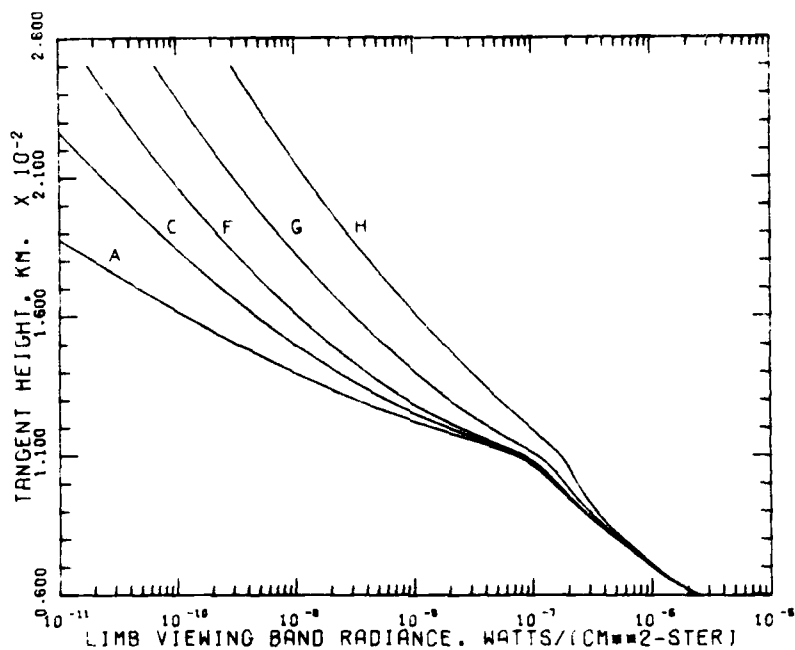


Figure 2. Limb Viewing Radiance Values for CO_2 15 μm Band Complex, Cases A, C, F, G, and H

density differences lead to separation of the curves. Figure 12 shows the radiance values for the 10012-00001 CO_2 band at 2.77 μm .

Figures 13 and 14 present radiances from two important bands of H_2O . These bands are the 010-000 6.27 μm and the 001-000 2.63 μm bands. Figures 15 and 19 compare NO band radiances. Figures 16 through 18 give 5.4 μm NO spectral radiances at tangent heights of 100, 140, and 200 km. NO concentrations are identical for all cases, as are atomic oxygen concentrations. The brightness differences below 140 km tangent height are due to temperature differences that control the rate of excitation by collision with atomic oxygen. The O_3 band radiances at 9.6 μm are shown in Figure 20.

The low altitude atmospheric models available (see Chapter 3, Section 2.3) are models of average conditions, monthly, at a small number of latitudes. There is no model readily available that can follow the daily variations in tropospheric weather and stratospheric circulation patterns. It is possible to simulate variability by adding to the model's smooth temperature profile random temperature excursions. A number of different profiles based on a single temperature profile could then be used to simulate viewing paths through a varying atmosphere.

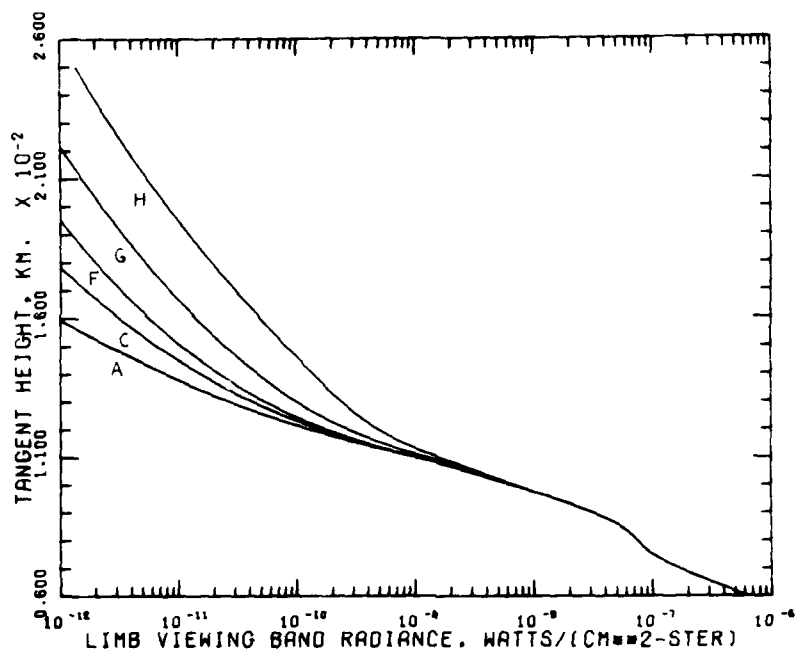


Figure 3. Limb Viewing Radiance Values for the 10002-01101 CO_2 16.2 μm Band, Cases A, C, F, G, and H

The matching of low altitude atmospheric models to high altitude models such as MSIS and J77 requires a procedure to integrate downward from, for instance, 150 km, where the model is reasonably accurate, through the region between 120 and 90 km, where temperature and composition are not known well, to the top of the low altitude model. The problem is in determining a reasonable temperature profile to bridge the gap between 90 and 150 km. In each case, several trials will be required and criteria must be developed to make the downward integration follow a temperature profile that is in accord with what is known about this region. The general technique is available in the algorithms used in analyzing falling sphere data.

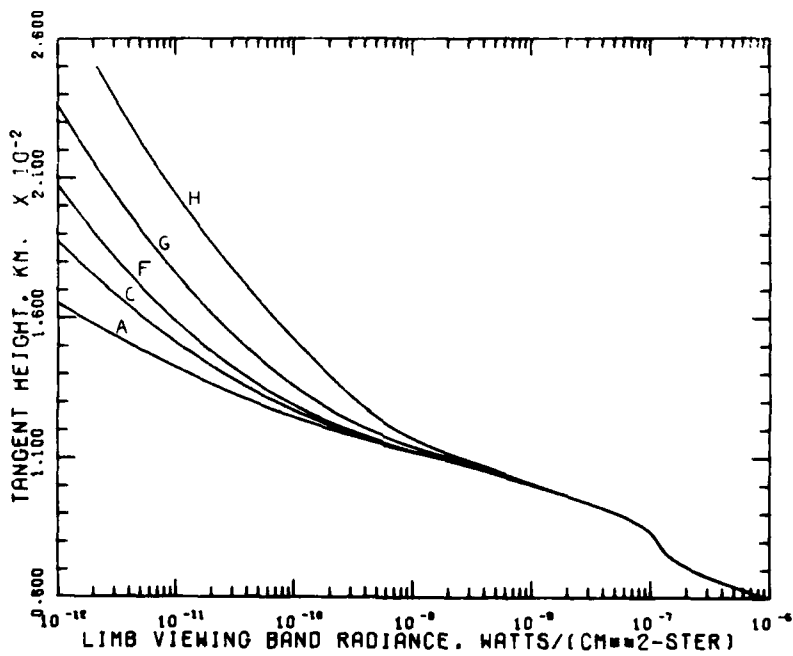


Figure 4. Limb Viewing Radiance Values for the 10001-01101 CO₂ 13.9 μm Band, Cases A, C, F, G, and H

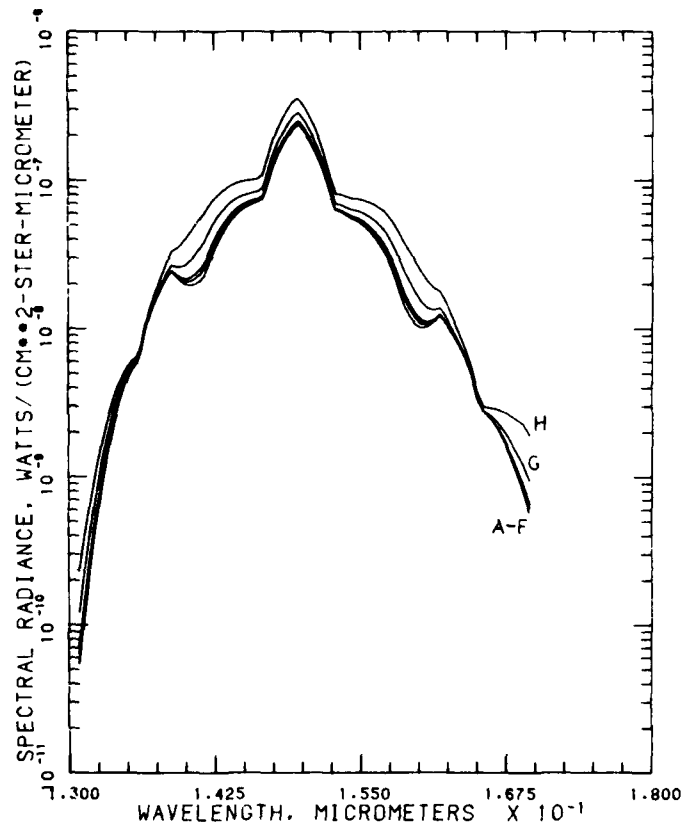


Figure 5. Limb Viewing Spectral Radiances Near 15 μm ,
100 km Tangent Height

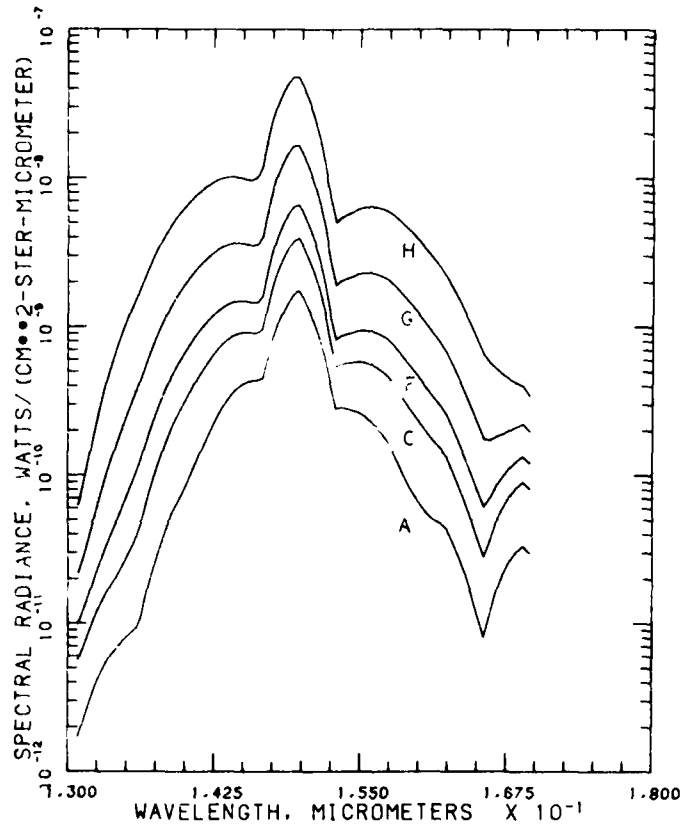


Figure 6. Limb Viewing Spectral Radiances Near 15 μ m, 140 km Tangent Height

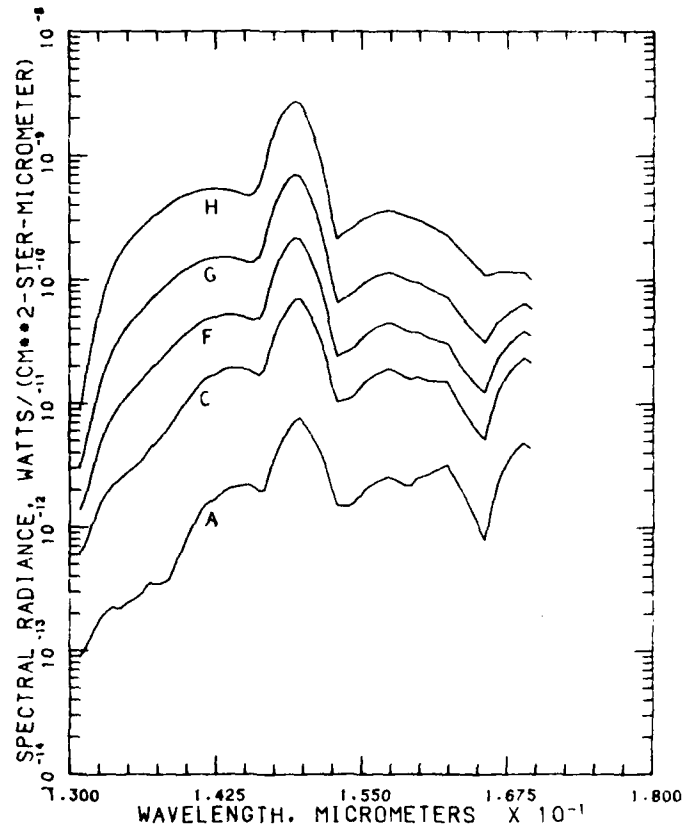


Figure 7. Limb Viewing Spectral Radiances Near 15 μ m Tangent Height

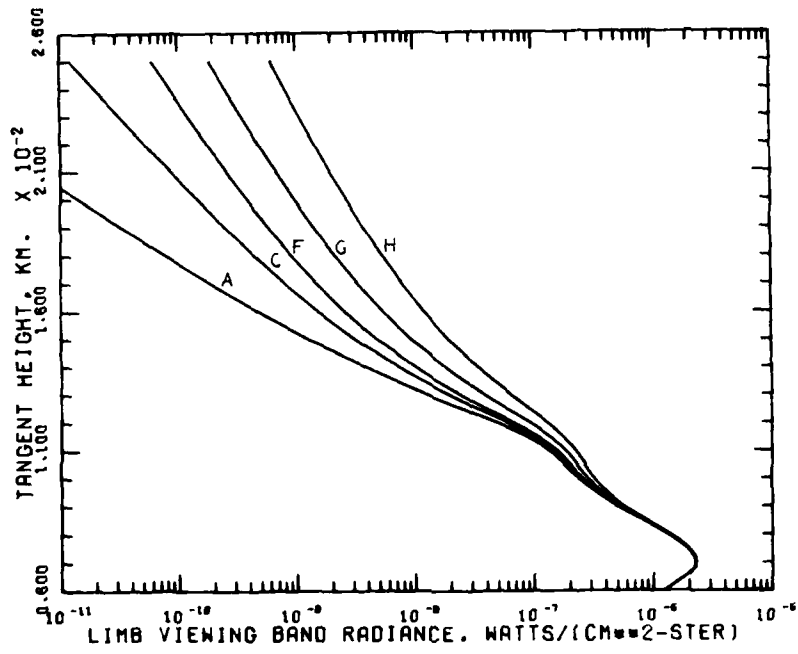


Figure 8. Limb Viewing Radiance Values for CO₂ 4.3 μm Bands, Cases A, C, F, G, and H

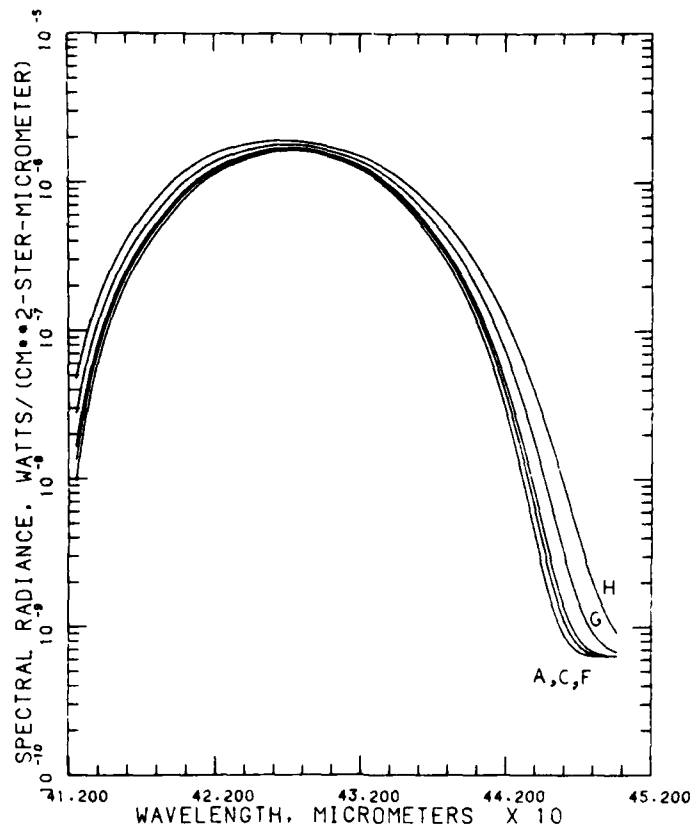


Figure 9. Limb Viewing Spectral Radiances Near 4.3 μ m, 100 km Tangent Height

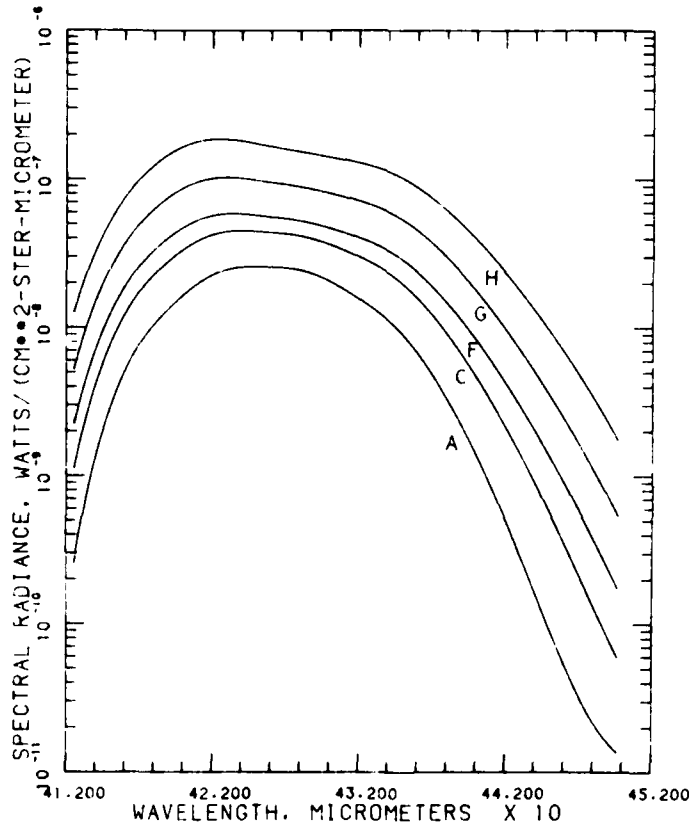


Figure 10. Limb Viewing Spectral Radiances Near 4.3 μm, 140 km Tangent Height

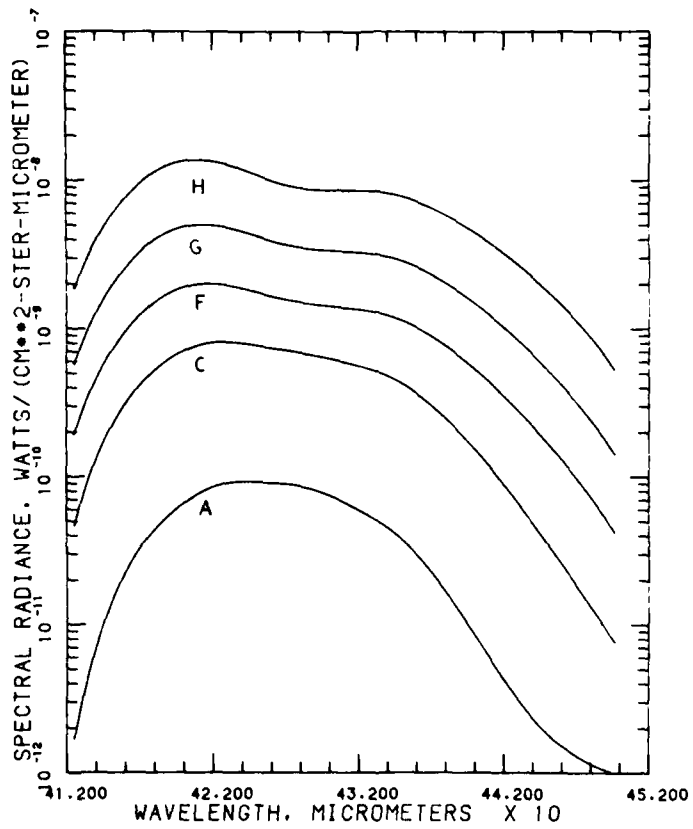


Figure 11. Limb Viewing Spectral Radiances Near 4.3 μm, 200 km Tangent Height

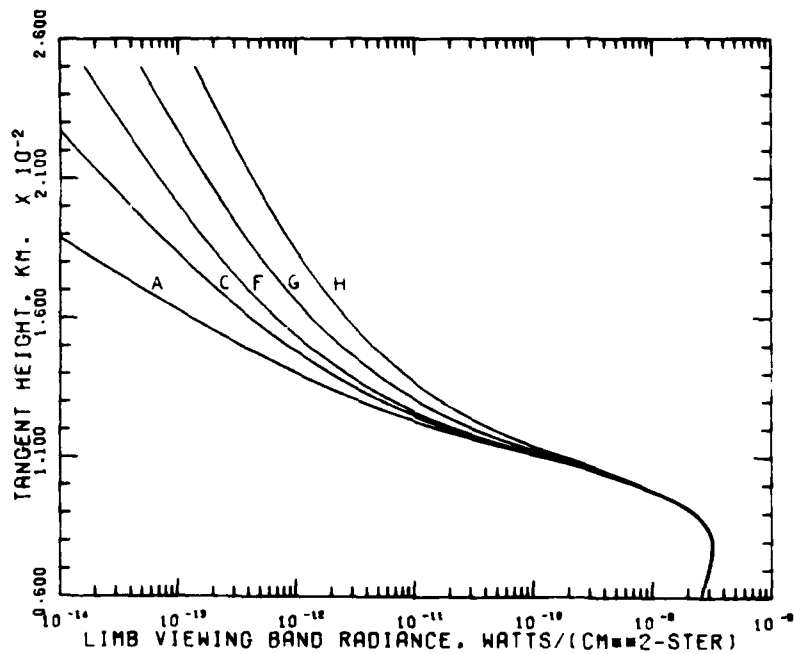


Figure 12. Limb Viewing Radiance Values for the 10012-00001 CO_2 2.77 μm Band, Cases A, C, F, G, and H

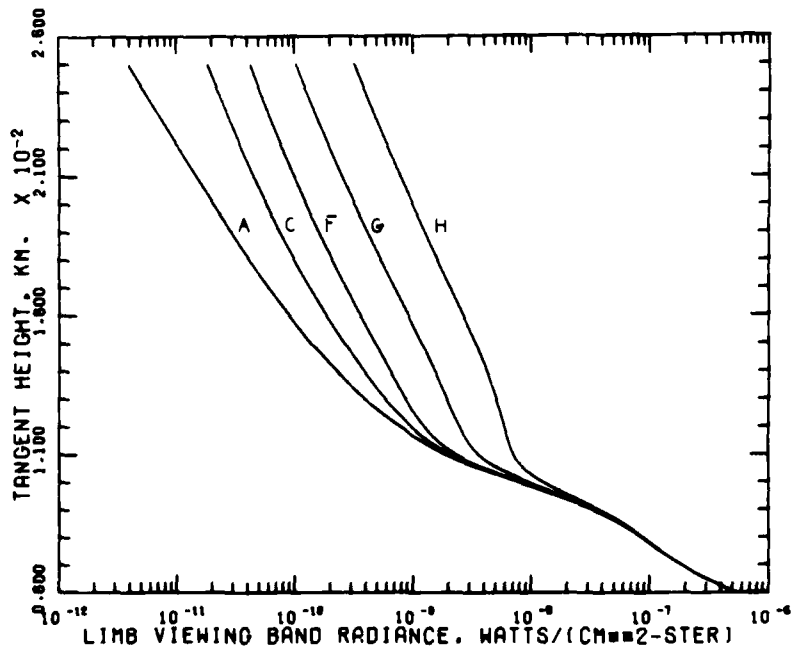


Figure 13. Limb Viewing Radiance Values for the 010-100 H_2O 6.27 μm Band, Cases A, C, F, G, and H

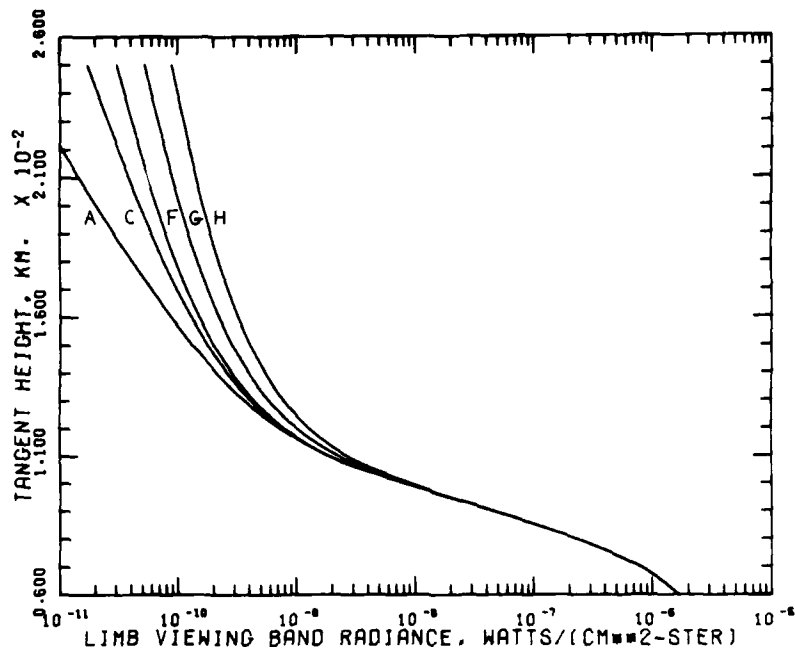


Figure 14. Limb Viewing Radiances for the 001-000 H₂O 2.66 μm Band, Cases A, C, F, G, and H

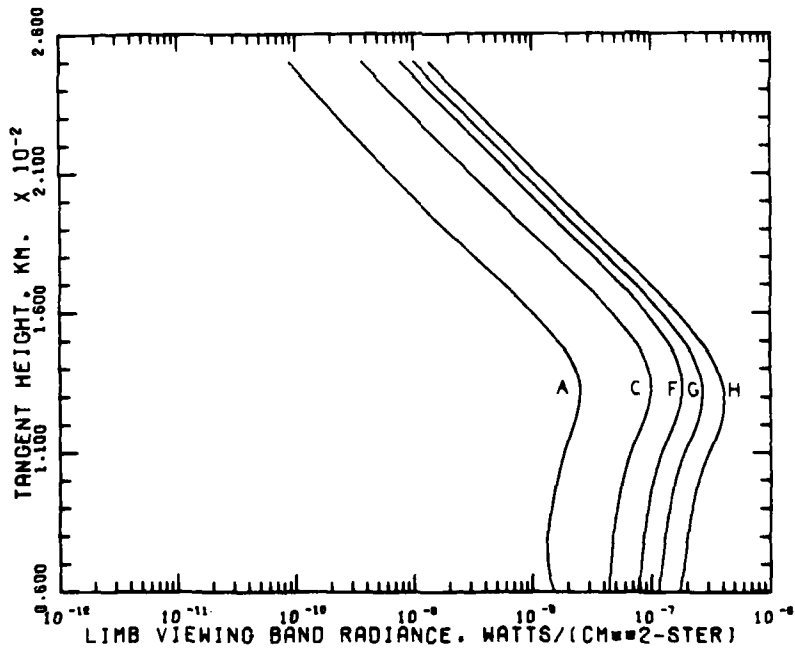


Figure 15. Limb Viewing Radiances for NO 1-0 Fundamental Band, Cases A, C, F, G, and H

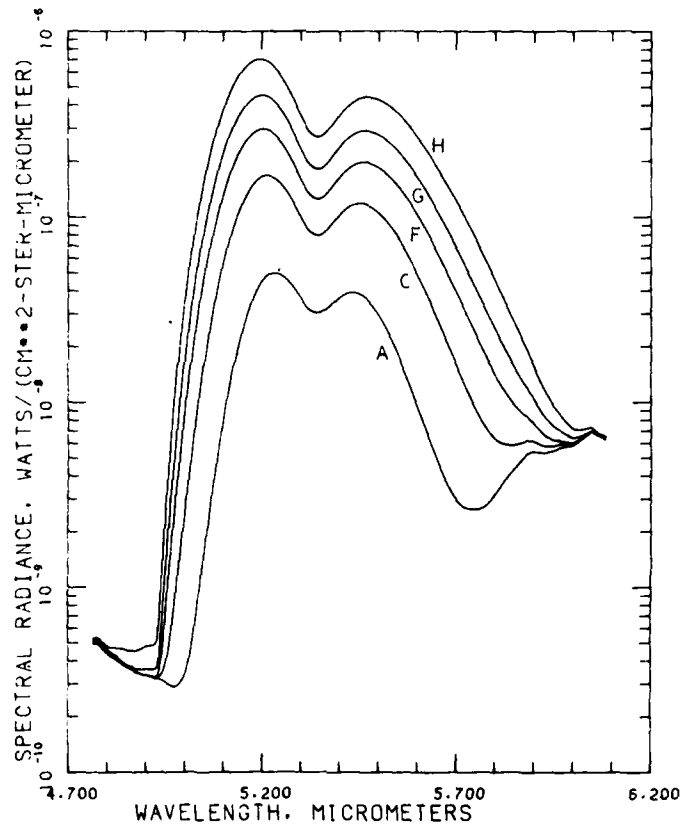


Figure 16. Limb Viewing Spectral Radiances Near 5.4 μ m, 100 km Tangent Height

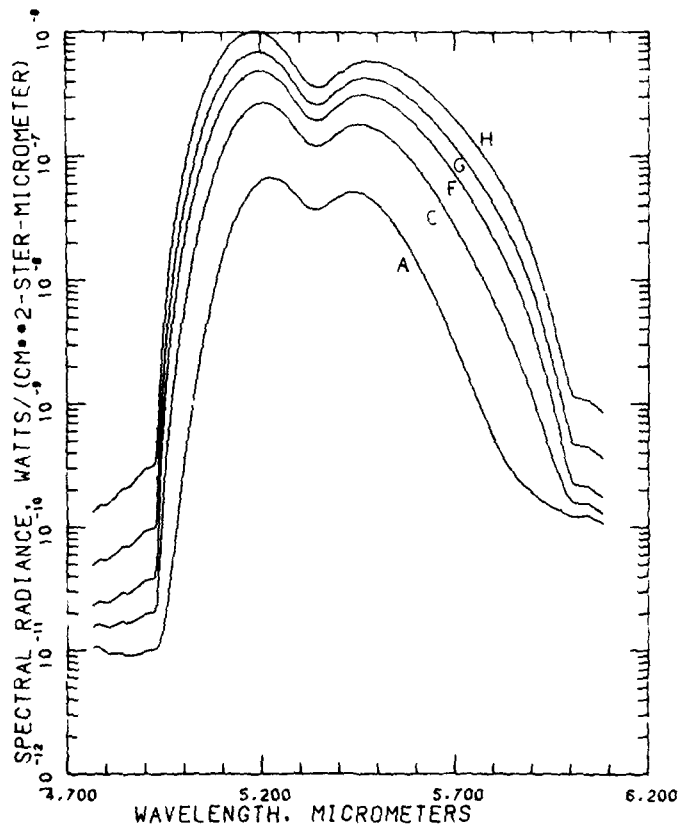


Figure 17. Limb Viewing Spectral Radiances Near 5.4 μm ,
140 km Tangent Height

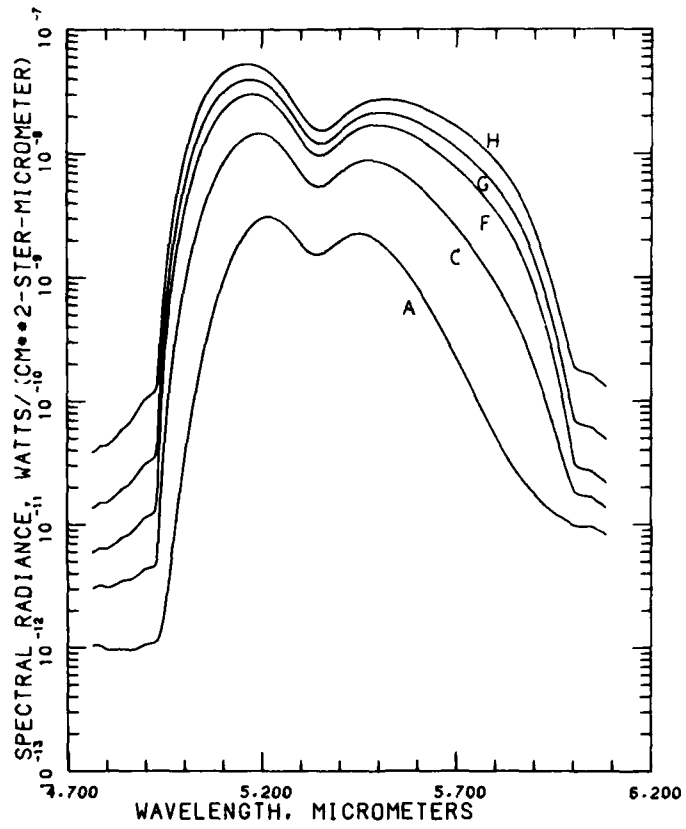


Figure 18. Limb Viewing Spectral Radiances Near 5.4 μm ,
200 km Tangent Height

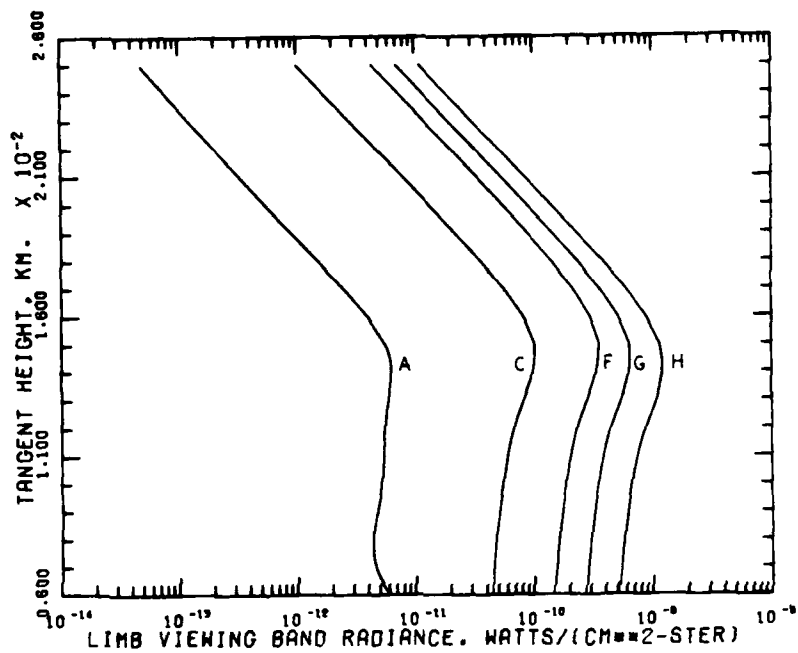


Figure 19. Limb Viewing Radiance for NO 2-0 Overtone Band, Cases A, C, F, G, and H

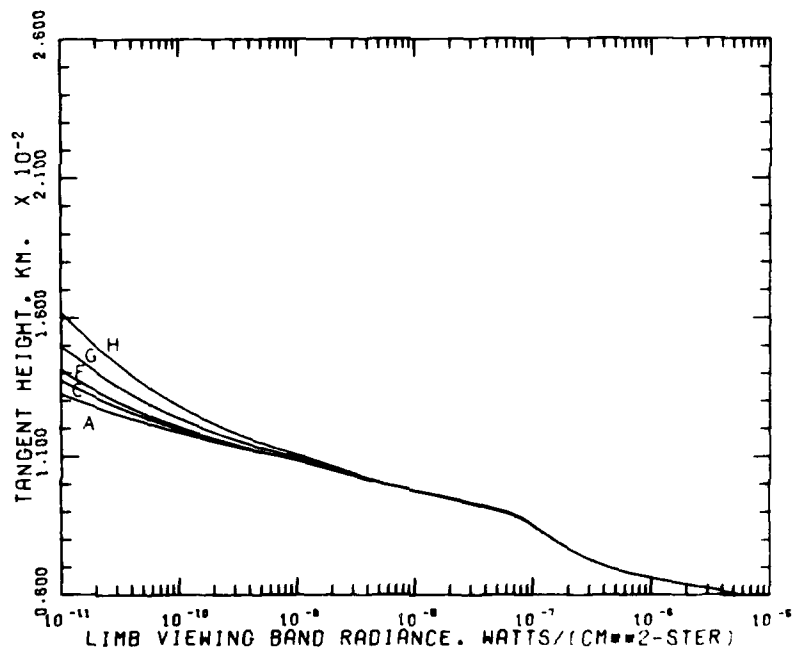


Figure 20. Limb Viewing Radiance for the 001-000 O₃ 9.6 μ m Band, Cases A, C, F, G, and H

Contents

1. Introduction	73
2. Sources of Atmospheric Structure	74
3. Atmosphere Structure Measurements	82
4. Atmospheric Background Clutter Analysis	102
5. Auroral Excitation of Infrared Radiators	104

5. Atmospheric Structure

C.H. Humphrey
Visidyne, Inc.
Burlington, Mass.

C.R. Philbrick
Air Force Geophysics Laboratory
Hanscom Air Force Base, Mass.

S.M. Silverman
Air Force Geophysics Laboratory
Hanscom Air Force Base, Mass.

T.F. Tuan
University of Cincinnati
Cincinnati, Ohio

M. Anapol
S.S.G., Inc.
Waltham, Mass.

J.B. Kumer
Lockheed Missiles and Space Corp.
Palo Alto, Calif.

1. INTRODUCTION

In addition to the long-term variations of the atmospheric species concentrations and temperature described in Chapter 3, the atmosphere is subject to variations that have shorter periods and smaller spatial wavelengths. These variations

in species concentrations and temperature can result in fluctuations of the resultant infrared intensity that can effect the interpretation of infrared measurements. In this chapter we review information concerning these variations and draw some conclusions as to the magnitude and size of the spatial structures as functions of altitude.

A preliminary model for the calculation of the noise (that is, the clutter) created in infrared measuring systems due to the effects of random spatial structures on the radiant intensity is also discussed. In addition, we shall briefly discuss auroral emissions and a model showing how spatial fluctuations in TV all-sky photometric measurements of visible aurora radiation can be used to generate spatial power spectral densities of the auroral infrared radiance.

2. SOURCES OF ATMOSPHERIC STRUCTURE

Dynamic effects such as tides and gravity waves can perturb a "quiet static" atmosphere. The sources of these dynamic effects can be associated with a very large variety of phenomenon, such as absorption of solar radiation by atmospheric species, solar heating of the surface, sunspot variations, magnetospheric substorms, particle events, severe tropospheric disturbances, planetary waves, wind-induced waves from interaction with orographic features, earthquakes, and volcanic eruptions or artificially produced phenomenon such as bomb explosions.

2.1 Tidal Effects

Large-scale tidal oscillations of the atmosphere are produced mainly by the thermal action resulting from the absorption of solar radiation in the stratosphere and lower mesosphere. That the very strong semidiurnal component in the barometric variation was due mainly to the sun's heating was first recognized by Laplace. The present inviscid tidal theory is based on the classical work of Siebert (1954)¹ and Sen and White, (1955),² who were the first to consider atmospheric heating rather than heating by upward eddy conduction from the ground. Siebert found that absorption by H₂O can account for 1/3 of the large semidiurnal component while absorption by O₃ can account for the remaining two thirds. The large semidiurnal component of pressure at the ground level, relative to the diurnal component, and the higher values of the diurnal component in the middle and upper atmosphere are explained on the basis that heating from O₃ absorption does not reach ground.

1. Siebert, M. (1954) Zur theorie der thermischen erregung gezeitenartiger schwingungen der erdatmosphäre. Z. Naturwissenschaften 41:446.
2. Sen, H.K. and White, M. L. (1955) Thermal and gravitational excitation of atmospheric oscillations, J. Geophys. Res. 60:483-485.

For a basic treatment of tidal wave theory the reader is referred to Chapman and Lindzen (1970).³ Recent theoretical advances in tidal wave theory deal mainly with the addition of such effects as mean zonal winds, meridional temperature gradients, composition variations, and hydromagnetic coupling, as well as dissipative effects such as molecular viscosity, thermal conductivity, radiative damping, and ion drag. For a review that considers some of these recent advances see Forbes and Garrett (1978).⁴ The empirical classification of the observed tides, as well as the theoretical treatment, is generally done in the form of harmonic analysis. However, owing to weather and seasonal changes, the dependent variables, such as pressure or temperature, are not quite cyclic on a day-to-day basis. In the thermosphere where ion drag, viscosity, and heat conduction are important, there is no such thing as a pure tidal mode.

The tidal effects on an otherwise unperturbed atmosphere produce inhomogeneities in optical emission and composition of various atmospheric species, some of which can take part in reactions involving infrared radiation bands. The effects on the emission of the green line of atomic oxygen (557.7 nm) were considered by Forbes and Geller (1972)⁵ and Petitdidier and Teitelbaum (1977).⁶ Assuming the Chapman three-body recombination mechanism for molecular oxygen and chemical equilibrium, the green line intensity is proportional to the cube of the atomic oxygen density. Forbes and Geller (1972)⁵ determined the variation of $[O]$ with lunar tide from the continuity equation neglecting production and loss. They concluded that the lunar tide is sufficient to produce a variation in the green line airglow similar to that observed. Petitdidier and Teitelbaum (1977)⁶ considered the effects of solar thermal tides. They assumed that the composition of the atmosphere remains unchanged under the influence of the tidal wave and used a model that assumes a sinusoidal variation of the relative density in terms of time and space. Using a vertical wavelength of 45 km and a period of 12 h, that is, a semidiurnal tide, Petitdidier and Teitelbaum obtained intensity ratios (I_{\min}/I_{\max}) in fair agreement with observed data.⁶ They were also able to fit observed OH experimental data with a semidiurnal tide. This analysis did not give a very sensitive test to the tidal wave theory since they compared only the total column intensity ratios. The formation of OH from the reaction

3. Chapman, S., and Lindzen, R.S. (1970) Atmospheric Tides, D. Reidel, Hingham, Mass.
4. Forbes, J. M. and Garrett, H. B. (1978) Solar diurnal tide in the thermosphere, J. Atmos. Sci. 35:148-208.
5. Forbes, J. M. and Geller, M. A. (1972) Lunar semidiurnal variation in OI (5577A) nightglow, J. Geophys. Res. 77:2942-2947.
6. Petitdidier, M. and Teitelbaum, H. (1977) Lower thermosphere emissions and tides, Planet Space Sci. 25:711-721.



is dependent on the concentrations of the minor species H and O₃ that are influenced by the tidal wave. The assumption that the atmospheric composition is not influenced by the tidal wave is only true for major species.

Diurnal variations in the concentrations of H, He, O, O₂, N₂, and Ar due to energy sources in the lower atmosphere and, in particular the EUV, have been considered by Harris and Mayr (1975,⁷ 1977⁸). Their calculations are based on a two-component model in which the two components are the major species N₂ and O. This treatment assumes, that while the major components may impart momentum to the minor components, the minor components do not physically or chemically affect the major components in any way. Their results show that the most important contribution to the diurnal variation is the thermal expansion followed by wind-induced diffusion that, in fact, dominates the diurnal variation of He and prevails strongly in the variations of O, O₂, and Ar below 200 km.

Forbes (1978)⁹ and Forbes and Garrett (1978)⁴ used a single component N₂ as the major species and all other constituents, that include O, O₂, Ar, He, and H, as minor species. The minor species were coupled to the major species through collision. Special emphasis is placed in their calculations on the diurnal and semidiurnal variations at sunspot maximum and minimum. Their results show that, between the equator and the midlatitude, the diurnal tidal variation in the thermospheric composition depends, at a given height, more strongly on the solar cycle than on the latitudinal position. The opposite is true for the semidiurnal tidal variations, where they find a major dependence with latitude in the semidiurnal amplitude and phase. These effects are presently not modeled in the J77 and MSIS models. Differences in the total density variations between equatorial and middle latitudes are predicted by this theory (Forbes and Marcos, 1979)¹⁰ to be of the order of 20 - 50 percent in amplitude and 3 - 6 h in phase for the semidiurnal component, 0-20 percent in amplitude and 0-6 h in phase for the diurnal component, and 15 km in the altitude of transition from semidiurnal to diurnal

7. Harris, I. and Mayr, H.G. (1975) Diurnal variations in the thermosphere, J. Geophys. Res. 80:3925-3933.
8. Mayr, H.G. and Harris, I. (1977) Diurnal tide, composition, and winds, J. Geophys. Res. 82:2628-2640
9. Forbes, J.M. (1978) Tidal variations in thermospheric O, O₂, N₂, Ar, He and H, J. Geophys. Res. 83:3691-3698.
10. Forbes, J.M. and Marcos, F.A. (1979) Seasonal-latitudinal tidal structures of O, N₂, and total mass density in the thermosphere, J. Geophys. Res. 84:31-35.

predominance. Experimental data that supports their results is presented in the next section.

2.2 Atmospheric Gravity Waves

Gravity waves are atmospheric waves with frequencies lower than the natural oscillation of the atmosphere, the Brunt-Vaisala frequency, that has a period ranging from less than 5 min to 15 min. For a gravity wave the pressure gradient, which may be along any direction, is modified by the influence of gravitational and buoyant forces that are along the vertical direction. Since the frequency of the wave is less than the Brunt-Vaisala frequency, the influence of the gravity and buoyancy forces begin to manifest themselves and the wave is no longer in the direction of the pressure gradient. For a free gravity wave in an isothermal atmosphere an upward transfer of energy (group velocity) is always accompanied by a downward phase propagation and vice versa (Hines, 1960).¹¹

As far as introducing variabilities and inhomogeneties, there are three main features that distinguish gravity waves from the tides. These features are:

1) gravity waves can often have length scales of the order of 6 to 8 km (for example, vertical wavelength) that are considerably less than the length scales of tidal waves, 2) gravity waves can have time scales of the order of 10 min to two or three hours that are considerably less than the time scales of diurnal or semi-diurnal tides, and 3) gravity waves occur randomly, unlike the tides that occur regularly due to solar heating of the atmosphere.

The effects of gravity waves were initially detected in microbarographs at the ground level, airglow measurements from various altitudes in the atmosphere, and ionospheric radar measurements from higher altitudes. Recent techniques allow high resolution in-situ measurements of the effects of gravity waves. The earliest observations were made indirectly through their effects on the ionosphere called traveling ionosphere disturbances (TID). Georges (1968)¹² characterized the spectrum of observed TID into two distinct categories of waves: 1) the large-scale TID's have horizontal phase velocities greater than 350-400 m/sec and horizontal wavelengths exceeding 1000 km and 2) the medium-scale TID's have horizontal phase velocities commonly between 100 and 250 m/sec and horizontal wavelengths of the order of several hundred km's. They occur much more frequently than the large-scale TID's. The significant contribution in establishing that these large-scale TID's are caused by gravity waves was made by Thome (1968),¹³ who

11. Hines, C.O. (1960) Internal atmospheric gravity waves at ionospheric heights, Can. J. Phys. 38:1441-1481.
12. Georges, T.M. (1968) HF Doppler studies of traveling ionospheric disturbances, J. Atmos. Terr. Phys. 30:735.
13. Thome, G.D. (1968) Long-period waves generated in the polar ionosphere during the onset of magnetic storms, J. Geophys. Res. 73:6319-6336.

used the measurements of incoherent radar backscatter from different altitudes in the ionosphere as a function of time.

Gravity waves have also been detected from their effects on airglow emission. Many of the airglow emissions (for example, O 557.7 nm line, OH, etc.) have their peak intensities well below the peak of the ionospheric F-layer. This allows studies to be made over larger altitude ranges whenever the airglow data can be combined with the ionospheric data [for example, Dachs (1968)¹⁴ and Armstrong (1975)¹⁵]. Airglow data showing wave-like structures have been published by numerous people including Silverman (1962),¹⁶ Okuda (1962),¹⁷ and Dachs (1968).¹⁴ Dachs's data (1968)¹⁴ include observations on the O lines at 557.7 nm and 630.0 nm as well as simultaneous observations of various ionospheric parameters such as the altitude of the F2 peak $h'F_2$ and the lowest penetration frequency at the peak f^oF_2 .

The basic paper on gravity-wave theory is due to Hines (1960),¹¹ who assumed an inviscid uniform isothermal atmosphere. Even with such drastic assumptions this treatment provides a reasonably good first approximation for gravity waves with low horizontal phase velocities (less than 150 m/sec). For higher horizontal phase velocities the treatment breaks down as atmospheric structure begins to have an effect. Investigations of the acoustic gravity equations for a more realistic atmosphere show the presence of fully guided modes [Press and Harkrider (1962),¹⁸ Pfeffer and Zarichny (1963),¹⁹ Harkrider and Wells (1968)²⁰] as well as partially guided or leakage modes [Friedman (1966),²¹ Reddy (1969)²²]. The

14. Dachs, J. (1968) Die helligkeiten des nachtllichen luftleuchtens wahrend des sommerflecken minimums nach messungen in Sudwestafrika, Beitr. Phys. d. Atmosphere 41:184-215.
15. Armstrong, E. B. (1975) The influence of a gravity wave on the airglow hydroxyl rotational temperature at night, J. Atmos. Terr. Phys. 37:1585-1592.
16. Silverman, S. M. (1962) Unusual fluctuations of 5577 Å O I airglow emission intensity on October 28-29, 1961, Nature 195:481-482.
17. Okuda, M. (1962) A study of excitation process in night airglow, Sci. Rep. Tohoku Univ. 5th Ser. Geophysics, 14:9-26.
18. Press, F. and Harkrider, D. G. (1962) Propagation of acoustic-gravity waves in the atmosphere, J. Geophys. Res. 67:3889-3908.
19. Pfeffer, R. L., and Zarichny, J. (1963) Acoustic-gravity wave propagation in an atmosphere with two sound channels, Pure and Appl Geophys. 55:175-199.
20. Harkrider, D. G. and Wells, F. J. (1968) Acoustic-Gravity Waves in the Atmosphere-Symposium Proceedings, T. M. Georges, (ed.) U.S. Government Printing Office, Washington, D. C., pp. 299-314.
21. Friedman, J. P. (1966) Propagation of internal gravity waves in a thermally stratified atmosphere, J. Geophys. Res. 71:1033-1054.
22. Reddy, C. A. (1969) Internal Gravity and Acoustic Waves, A Colloquium, NCAR-TN-43, pp. 229-240.

inclusion of dissipation can produce additional partially guided modes [Tuan (1976),²³ Richmond (1978)²⁴]. In general, inhomogeneities can scatter gravity waves and hence, may (although not necessarily) produce additional guided modes.

Both for the case of the tidal waves and gravity waves the theories have been mainly tested against the observed temporal variations in the optical emission. The effect of gravity waves on the atmospheric emission of the O 630 nm and the N 520 nm lines was treated theoretically by Porter, Silverman, and Tuan (1974)²⁵ with satisfactory agreement between theory and experimental data. Spatial inhomogeneities have been observed in OH emission by Peterson and Kieffaber [Peterson and Kieffaber (1973),²⁶ Kieffaber and Peterson (1978)²⁷]. They found well defined OH structures to occur near the time of high lunar tide. Peterson (1979)²⁸ suggested that these structures may have been caused by gravity wave interactions in the OH layer. Gravity wave effects on any optical emission depend on the atmospheric minor constituents redistribution caused by the wave. The major constituents are assumed to move with the wave while the effects of the wave on the minor components are through collisions with the major constituents.

Chiu and Ching (1978)²⁹ have considered the general features that a Hines (1960)¹¹ gravity wave model will have on a minor atmospheric component whose density distribution is in the form of a single layer. Their summary of the conclusions of various authors are 1) the response of the layer to the gravity wave is sharper at the bottom side than at the top side, 2) there is a 180° phase change in the response of the minor constituent in going from the bottom to the top side, and 3) the magnitude of the response depends on the gradient of the unperturbed layer. The sharper the gradient, the sharper becomes the response.

-
23. Tuan, T. F. (1976) Research in Gravity Waves and Airglow Phenomena, AFGL-TR-76-0296, AD A040 414.
- Richmond, A. D. (1978) Gravity wave generation, propagation and dissipation in the thermosphere, J. Geophys. Res. 83:4131-4145.
25. Porter, H. S., Silverman, S. M. and Tuan, T. F. (1974) On the behavior of airglow under the influence of gravity waves, J. Geophys. Res. 79: 3827-3833.
26. Peterson, A. W. and Kieffaber, L. M. (1973) Infrared photography of OH airglow structures, Nature 242:321-323.
27. Kieffaber, L. H. and Peterson, A. W. (1978) Correlation studies of four submicron OH airglow bands during spacelab simulation, J. Atmos. Terr. Phys. 40:1339-1345.
28. Peterson, A. W. (1979) Airglow events visible to the naked eye, Applied Optics 18:3390-3393.
29. Chiu, Y. T. and Ching, B. K. (1978) The response of atmospheric and lower ionospheric layer structures to gravity waves, Geophys. Res. Lett. 5:539-542.

Recently, Hatfield et al (1981)³⁰ studied the variability of the OH emission produced by gravity waves. Their results indicate that structure in the emission profile could occur if the vertical wavelength of the gravity wave is less than the "width" of the emission profile. This corresponds to gravity waves with horizontal phase velocities less than 33 m/sec. Guided modes usually have much greater horizontal phase velocities and hence, much larger vertical wavelength and can only affect the integrated columnar emission as a function of time. Thus, gravity waves can always produce temporal inhomogeneities, but only those with small horizontal phase velocities and vertical wavelength of less than 10 km can produce spatial as well as temporal inhomogeneities.

Further studies on the fluctuation of OH and O₂(¹Σ) airglow have been made by Weinstock (1978).³¹ He found that for O₂(¹Σ) the temperature dependence of the reaction rate constant has a major influence on the temporal inhomogeneities.

Spatial and temporal inhomogeneities can be generated by atmospheric gravity waves if the energy of the waves is dissipated in forming a layer of turbulence [Hodges (1967)³²]. In some cases it is possible to show that large amplitude gravity waves with a Richardson's number less than one-half can parametrically excite Brunt-Vaisala oscillations (Tuan, et al, 1979³³). This means that temporal inhomogeneities of the relatively short time scales of Brunt-Vaisala oscillations (of the order of 4-12 min) are superimposed on inhomogeneities of the larger time scales (or the order of hours) of the gravity wave oscillations.

Gravity waves that are usually present in the middle and upper atmosphere are frequently associated with sources in the lower atmosphere. At times this wave propagation can be effectively cut off from the upper atmosphere by reflection or dissipation processes in the mesosphere. However, sources in the upper atmosphere also exists. An indication of the horizontal and vertical wavelengths of gravity waves in the mesosphere and the lower thermosphere is given in Figure 1 (Philbrick et al, 1978³⁴). Also shown are the viscous dissipation limits for

-
30. Hatfield, R., Tuan, T. F. and Silverman, S. M. (1981) On the effects of atmospheric gravity waves on profiles of H, O₃, and OH emission, J. Geophys. Res. 80:2429-2437.
 31. Wienstock, J. (1978) Theory of the interaction of gravity waves with O₂(¹Σ) airglow, J. Geophys. Res. 83:5175-5185.
 32. Hodges, R. R. (1967) Generation of turbulence in the upper atmosphere by internal gravity waves, J. Geophys. Res. 72:3455-3458.
 33. Tuan, T. F., Hedinger, R., Silverman, S. M. and Okuda, M. (1979) On gravity wave induced Brunt-Vaisala oscillations, J. Geophys. Res. 84:393-398.
 34. Philbrick, C. R., Noonan, J. P., Fletcher, F., Jr., Hanrahan, T., Salah, J. E., Blood, D. W., Olsen, R. O., Kennedy, B. W. (1978) Atmospheric Properties From Measurements at Kwajalein Atoll on 5 April 1978, AFGL-TR-0195, AD A061 083.

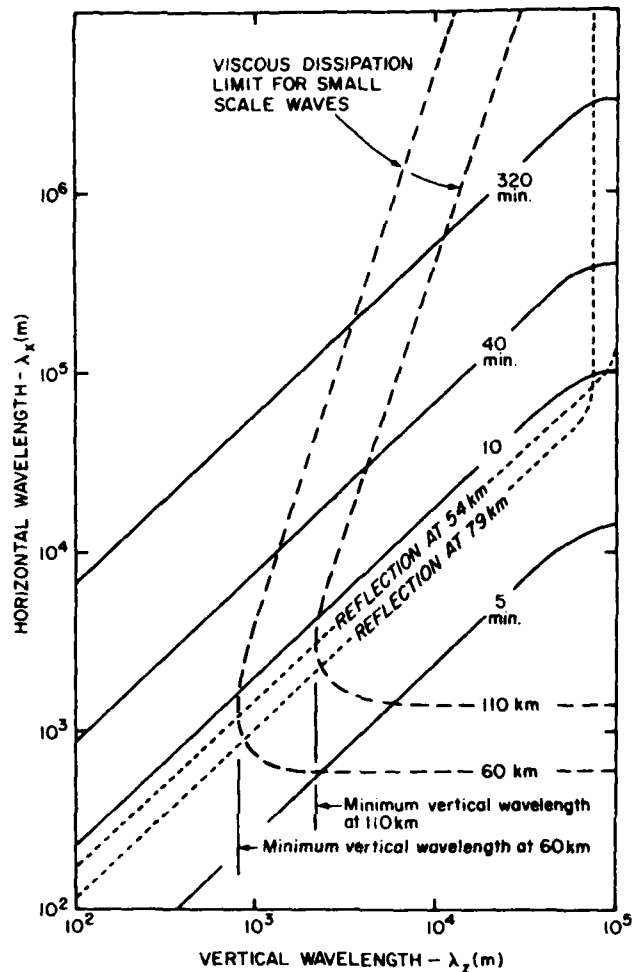


Figure 1. Wavelengths of Propagating Modes Expected in the Mesosphere and Lower Thermosphere From a Reexamination of the Analysis of Hines³⁵ With Inclusion of Eddy Viscosity Contribution. The periods in min are shown as constant period contours (solid lines). The viscous dissipation limit for small-scale waves at 60 and 110 km are shown (dash lines) and represent the limits of the permitted spectrum from effects of viscous damping (modes lying to the left and below these curves are excluded). Modes subject to reflection back toward the ground at heights of 54 and 79 km are indicated (dot lines) and modes lying to the right of these curves cannot proceed from the lower atmosphere (Philbrick et al, 1978³⁴).

35. Hines, C. O. (1974) *The Upper Atmosphere in Motion*, American Geophysical Union Monograph 18.

small-scale waves and the limits for modes subject to reflection back toward the ground. From Figure 1 we see that gravity waves propagating in the region from 60 to 110 km altitude will have wavelengths larger than 1 km at 60 km and larger than 3 km at 110 km.

Gravity waves may be produced by a number of mechanisms including orographic features such as mountain ranges, tropospheric disturbances such as thunderstorms, and localized pressure gradients produced by auroral heating in the mesosphere and lower thermosphere. Studies have been made by Davis and Da Rosa (1969)³⁶ on the frequency of occurrence of gravity waves produced by magnetic storms. The observations for the year 1967 showed a close correlation between the occurrence of TID's and severe magnetic storms ($K_p > 5$). For smaller storms there was far less correlation. These results are in good agreement with those of Georges (1968)¹² and Thome (1968)¹³ who suggested a relationship between enhanced magnetic activity and the occurrence of large-scale TID's.

In general, there has been little investigation on the frequency of occurrence of gravity waves due to other sources. If the theory as advanced by Hodges (1967)³² that gravity waves are an important factor in producing upper atmospheric turbulence is correct, then the frequency of occurrence must be much greater than that from magnetic storms.

3. ATMOSPHERE STRUCTURE MEASUREMENTS

3.1 Tidal Effects

The effects produced by the thermally driven tides in the upper atmosphere present another important consideration. Recently Forbes and Marcos (1979)¹⁰ analyzed total mass density data from the miniature electrostatic accelerometer (Mesa) experiment on the AE-E satellite to determine diurnal and semidiurnal tidal variations in the lower thermosphere (150-245 km) at latitudes less than 20° . The results of the analysis showed that structure changes from predominantly semidiurnal below 180 ± 5 km to predominantly diurnal above this altitude, with no strong dependence on season. These results are in agreement with recent theoretical (Mayr and Harris, 1977,⁸ Forbes, 1978⁹) and observational (Newton et al, 1975³⁷ Sharp et al, 1978³⁸) investigations (see Figure 2). The analysis by Forbes and Marcos showed a substantial summer/winter difference in the phase structure of the semidiurnal component of the total mass density variation.¹⁰ The results indicate that the combination of data from all seasons to determine an

References 36 to 38 will not be listed here. See References, page 114.

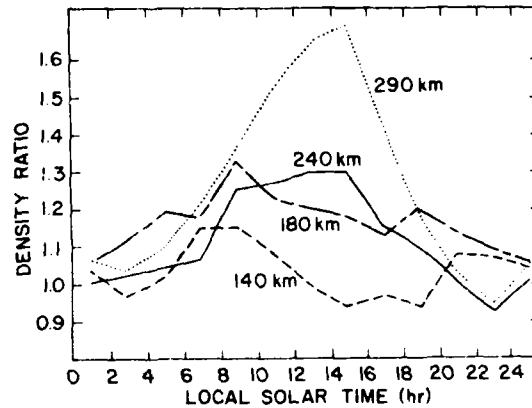


Figure 2. Average Ratio of the Measured Density to the Jacchia (1971) Model Prediction as a Function of Local Solar Time. The local time parameter for the model is taken to be local midnight in all cases, but all other parameters are handled in the manner prescribed in the model formulation. The data are binned at two-h intervals. Each curve includes all altitude increments within the 20 km band centered on the designated altitude (Sharp et al, 1978³⁸)

annual mean semidiurnal amplitude can lead to unrealistically small semidiurnal amplitudes, due to phase cancellation effects.

3.2 Atmospheric Gravity Waves

A few measurements of the total atmospheric density have been made using rocketborne falling spheres with accelerometers that are capable of making measurements with altitude resolution of 100 m. These measurements reveal a high degree of spatial structure in the measured density (see Figures 3 and 4). Figure 3 shows an example of the wave structure observed in the mesosphere and lower thermosphere using a recently developed accelerometer technique (Philbrick et al, 1978³⁴). Small-scale wave structures that are consistent with gravity waves (see Figure 1) are observed to be superimposed on longer wavelength oscillations. The large-scale waves above 70 km altitude in Figures 3 and 4 are presumably due to a combination of large-scale gravity waves of tidal oscillations or possibly artifacts due to the atmospheric model used for comparison. The appearance of the small-scale waves, as shown in these figures, has been observed on all of the half dozen flights that could have detected such waves. Thus, they are expected to be present under most conditions. Figure 4b shows the temperature derived on the

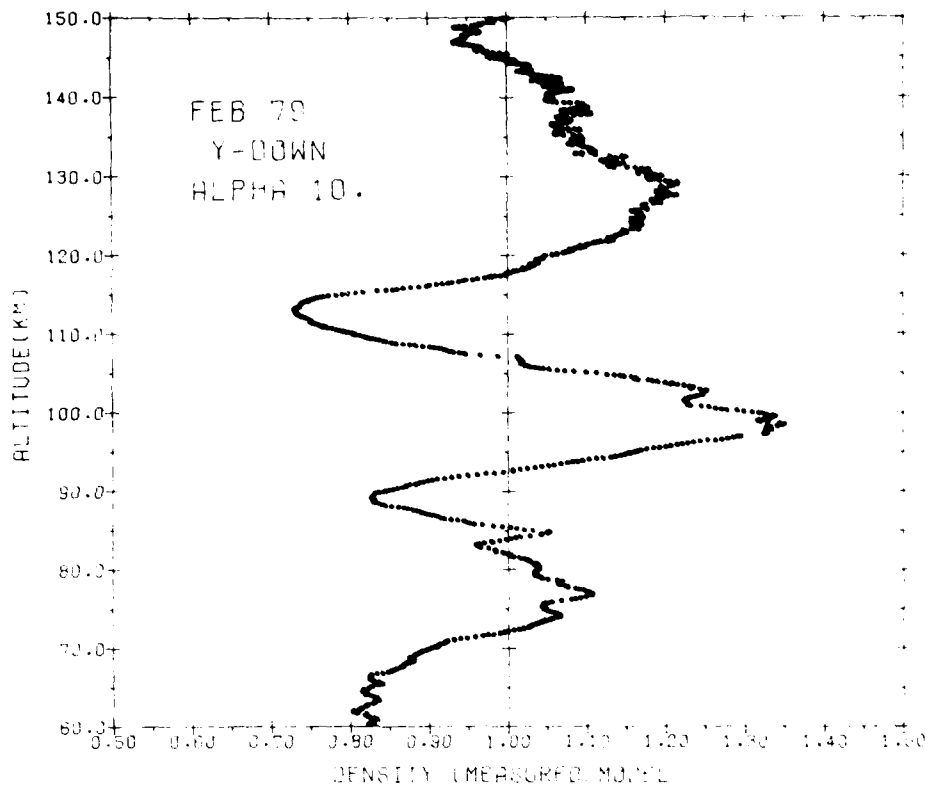


Figure 3. Density Measurements Made on 26 February 1979 are Shown as a Ratio to the USSA 76 Standard Model. Short wavelength (2-4 km) structure features are superimposed on longer-scale waves. The scatter of the measurement points at higher altitudes is due to the telemetry resolution of the data

basis of the density profile of Figure 4a and shows a high degree of vertical structure.

Figure 5 indicates the temporal dependence of the vertical structure (Philbrick et al, 1980³⁹). This figure shows the results of density measurements made at Kwajalein Atoll for two sets of falling sphere flights. The larger waves are seen to be nearly stationary in space (that is, not propagating vertically) over periods of several hours. These measurements were accompanied by simultaneous measurements of the wind velocity that permits a calculation of the Richardson number

39. Philbrick, C.R., Murphy, F.A., Zimmerman, S.F., Fletcher, E.J., Jr., and Olsen, R.O. (1980) Mesospheric density variability, Space Research XX:79-82.

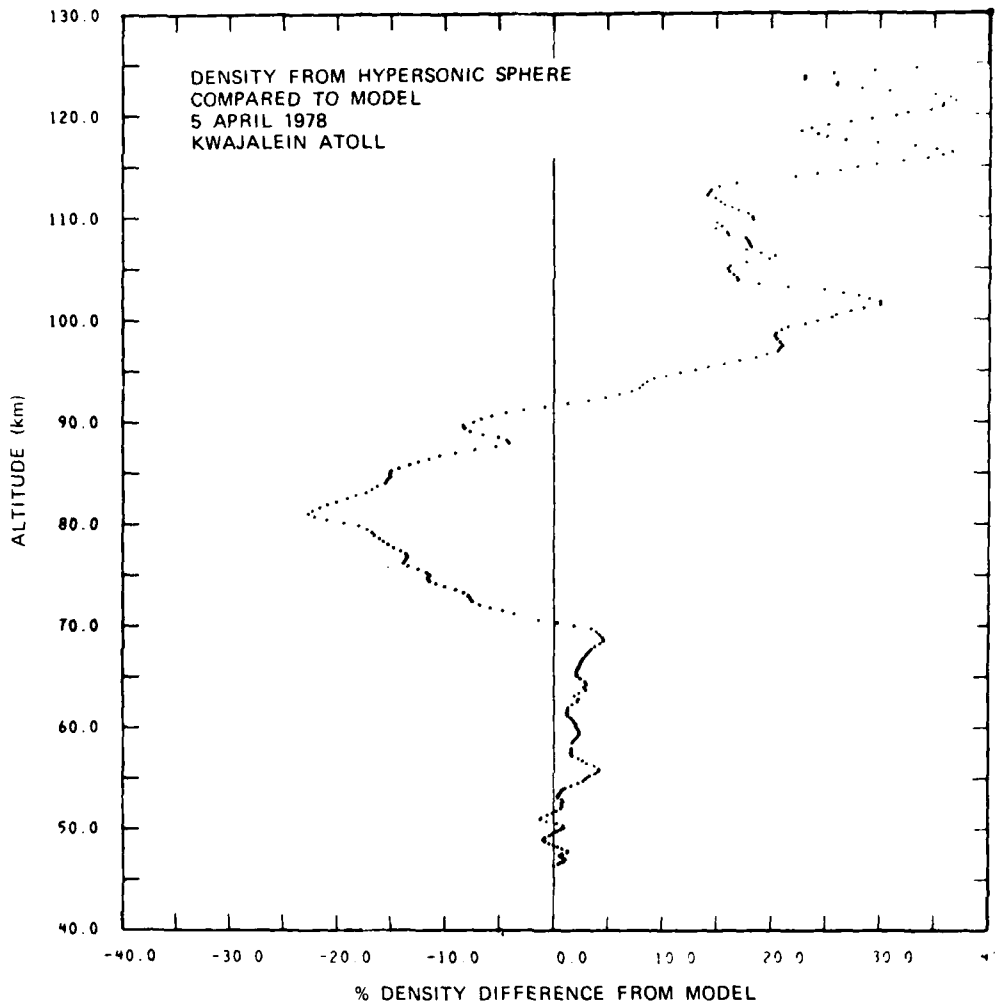


Figure 4a. Hypersonic Sphere Density Results from the Lincoln Laboratory, Analysis of the ALCOR Radar Data Compared to Model. Note the scale sizes of the vertical structure compared to the scales expected based on arguments presented in Figure 1 (Philbrick et al, 1978³⁴)

R_i . The results of this calculation are also shown in Figure 5. These plots show the scale sizes and the dynamically unstable regions ($R_i \leq 0.25$) due to the presence of wind shear. Negative values of the Richardson number exists in regions that are statically unstable because of the local density gradient.

In addition to these total density measurements, several rocketborne mass spectrometers have made measurements in the altitude range from 80 to 120 km.

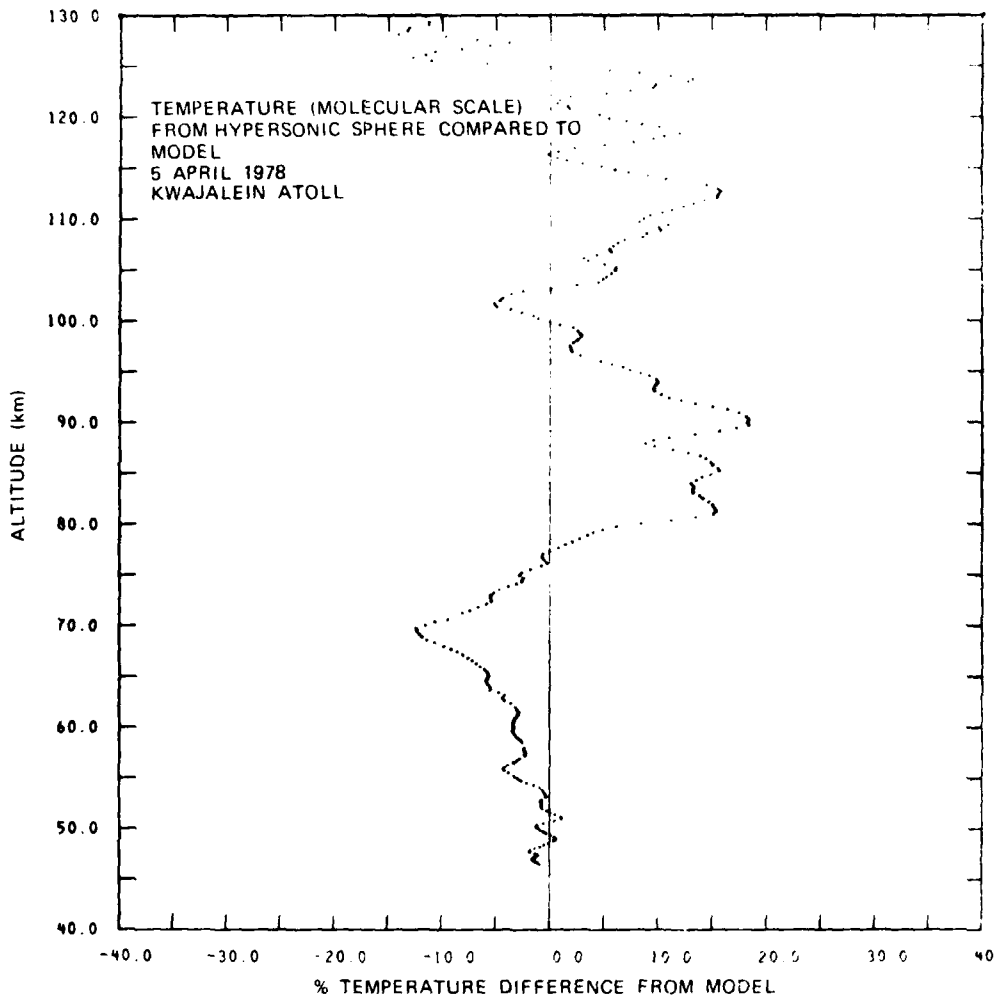


Figure 4b. Temperature from Lincoln Laboratory, Analysis of the Hypersonic Sphere Data Compared to Model (Philbrick et al, 1978³⁴)

Figure 6 shows an example of these measurements (Philbrick et al, 1978³⁴), where vertical wave structures are apparent in the species profiles. The atomic oxygen profile reveals a substantial amount of spatial structure. Similar structure has been observed in most flights. Measurements of the vertical structure of atomic oxygen made at the White Sands Missile Range (WSMR) using resonant

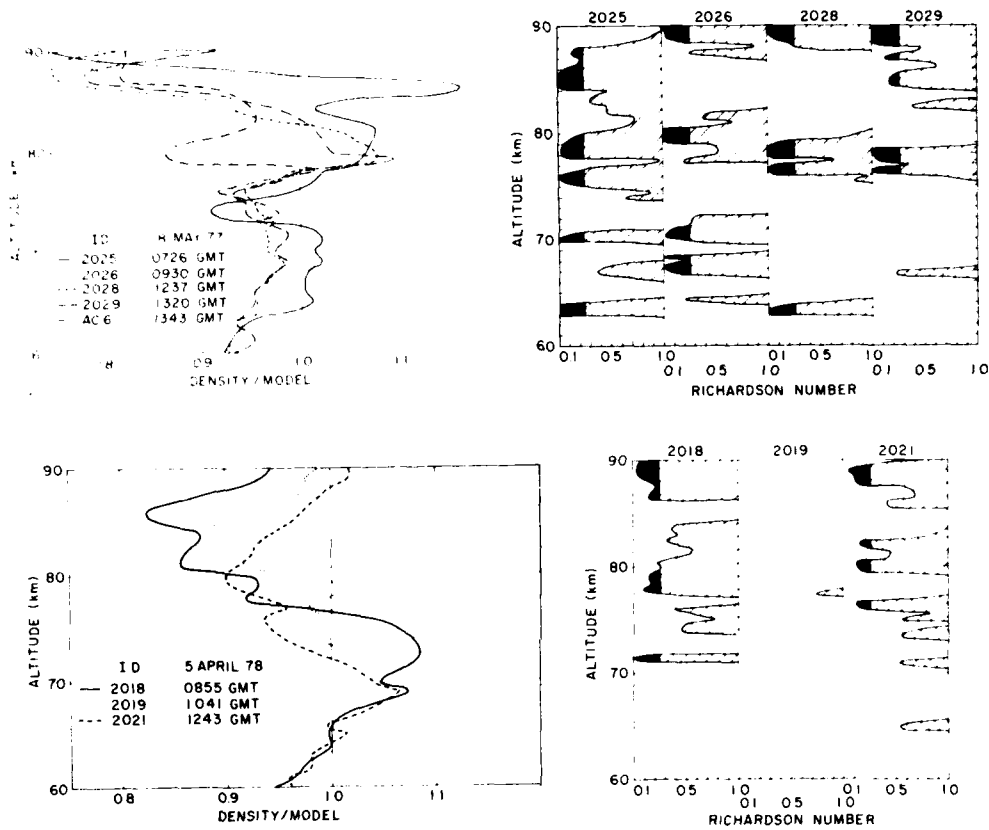


Figure 5. Density Measurements and Richardson Numbers for Falling Sphere Flights at Kwajalein Atoll on 18 May 1977 and 5 April 1978. (a) The density measurements are shown as a ratio to the Cole and Kantor tropical atmosphere for four Robin sphere flights and one accelerometer instrumented sphere (AC-6). (b) The Richardson numbers calculated from the temperature and wind measurements are shown for the range of values $0 < R_i < 1$ with the negative values plotted at $R_i = 0$. (Philbrick et al, 1980³⁹)

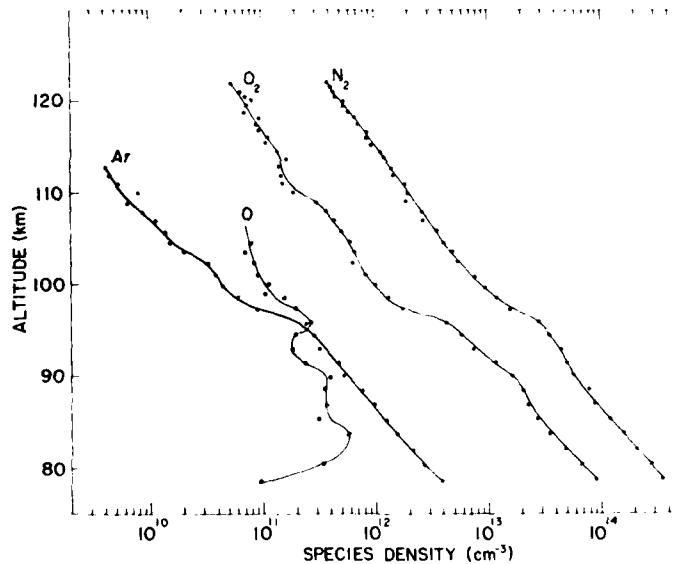


Figure 6. Species Densities vs Altitude Measured by the Mass Spectrometer on 23 January 1976 (Philbrick et al, 1978³⁴)

scattering of light indicates similar spatial structure (Figure 7, Howlett et al, 1980⁴⁰).

Results obtained from a dynamic model of the mesosphere and lower thermosphere (Keneshea et al, 1979⁴¹) are compared in Figure 8 with profile measurements obtained on 20 November 1970. This model requires data on the atmospheric composition and temperature as a function of altitude, as well as the molecular and turbulent diffusion coefficients. The latter are determined from wind trail measurements. The substantial agreement between theory and measurements indicates the importance of considering the atmospheric dynamics. Recent improvements in the Schumann-Runge flux factor would produce less atomic oxygen in the model calculation and improve the agreement between the model and the measured density of this species. The agreement supports the conclusion that atmospheric dynamics can strongly influence the density profile of a minor species such as atomic oxygen in the 80 to 100 km region.

40. Howlett, L. C., Baker, K. D., Megill, L. R., Shaw, A. W. and Pendleton, W. R. (1980) Measurement of a structured profile of atomic oxygen in the mesosphere and lower thermosphere, *J. Geophys. Res.* **85**:1291-1298.
41. Keneshea, T. J., Zimmerman, S. P. and Philbrick, C. R. (1979) A dynamic model of the mesosphere and lower thermosphere, *Planet. Space Sci.* **27**: 385-401.

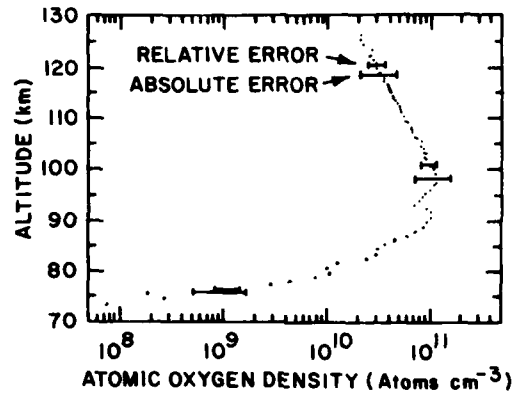


Figure 7a. Atomic Oxygen Density on Ascent Showing an Estimate of Relative and Absolute Errors (Three-sec running average with one point per sec shown) (Howlett et al, 1980⁴⁰)

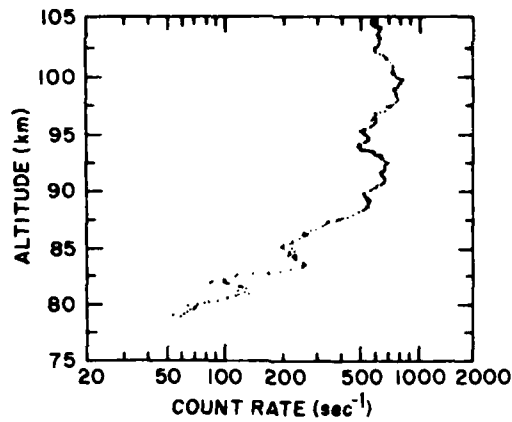


Figure 7b. High-resolution Ascent Data Showing Considerable Structure (One-sec running average with one point per 0.1 sec shown) (Howlett et al, 1980⁴⁰)

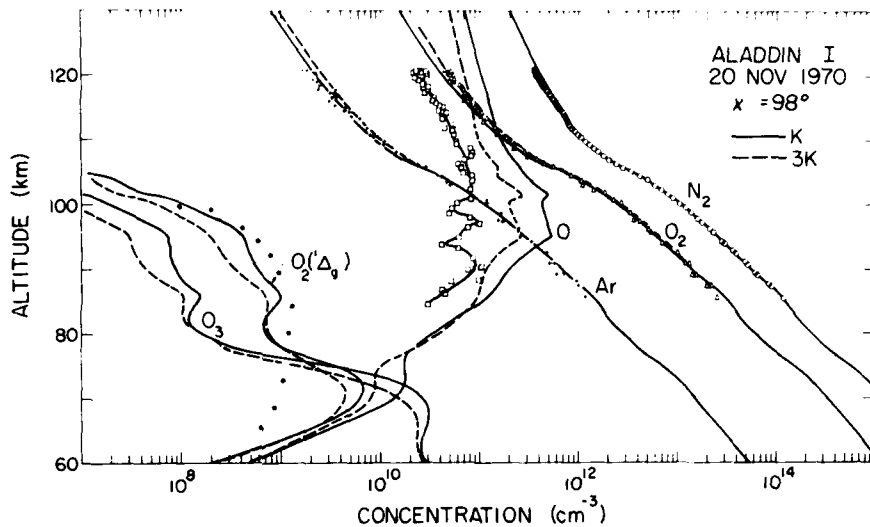


Figure 8. Comparison of Computed Species Profiles for Turbulent Diffusivities K and 3K (solid dashed curves) With Measured Profiles for O (squares), O₂ (triangle), N₂ (circles), Ar (crosses), and O₂(¹Δ_g)(dots)

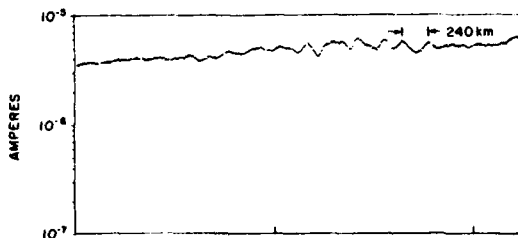
At higher altitudes, satellite measurements show wave-like variations that are thought to be due to gravity waves. In Figure 9, measurements made during flights of the S3-4 satellite (McIssac, 1980⁴²) reveal the presence of these waves with horizontal wavelengths of hundreds of km. These waves are frequently observed at high altitudes and are always present for disturbed periods ($K_p \geq 4$). The structure is strongly correlated with the auroral region and probably associated with pressure gradients created by momentum sources or localized heating in the lower thermosphere or upper mesosphere.

The nature of these waves is shown more clearly in the measurements made using the Nace instruments on flights of the AE-C satellite (Reber et al, 1975⁴³). In Figure 10 the wave structure is clearly revealed. The authors of this study (Reber et al, 1975⁴³) concluded from their analyses of the spatial structure for two orbits that: "This structure exhibits (1) scale sizes from a few tens of kilometers to several hundreds of km, (2) molecular nitrogen density amplitudes of the order of 5-15%, argon amplitudes about half of N₂ amplitudes and generally 180° out-of-phase with the N₂ and Ar, . . . The neutral data are qualitatively consistent

42. McIssac, J. P. (1980) Private communication.

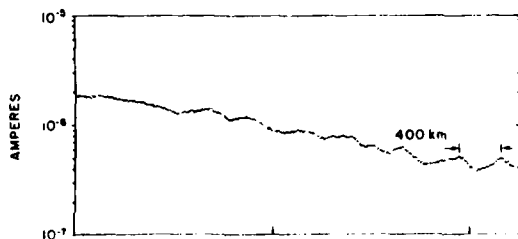
43. Reber, C. A., Hedin, A. E., Pelz, D. T., Potter, W. E., and Brace, L. H. (1975) Phase and amplitude relationships of wave structure observed in the lower thermosphere, *J. Geophys. Res.* 80:4576-4580.

S3-4 NEUTRAL DENSITY MEASUREMENTS
Particle Flux Accumulator Experiment
NEUTRAL DENSITY PHENOMENA – Atmospheric Waves



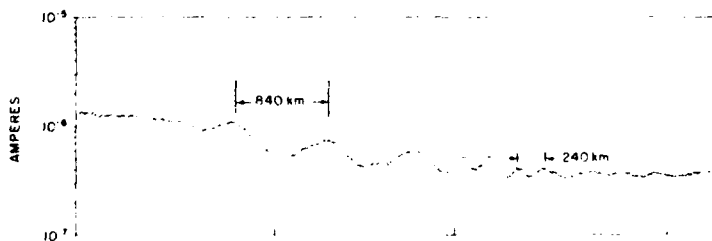
Rev. 900
05/11/78

UT 0419	0423	0427
ALT 210	202	195
LAT 29°	45°	61°
L.T. 2215	2203	2142



Rev. 221
03/30/78

UT 1037	1041	1045
ALT 235	246	252
LAT -64°	-79°	-80°
L.T. 0925	0753	0101



Rev. 217
03/30/78

UT 0314	0318	0322	0326
ALT 232	243	251	252
LAT -62°	-77°	-81°	-68°
L.T. 0930	0819	0142	2323

Figure 9. S3-4 Neutral Density Measurements – Particle Flux Accumulator Experiment Neutral Density Phenomena – Atmospheric Waves (McIssac, 1980⁴²)

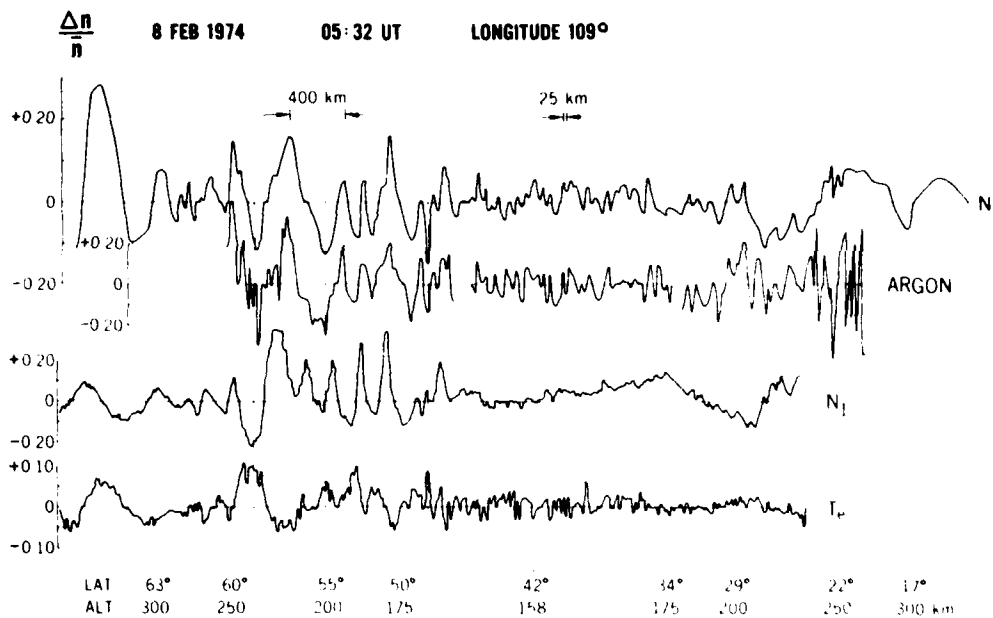


Figure 10. The Structural Variations of Molecular Nitrogen, Argon, Total Ion Density, and Electron Temperature. The relative scale sizes along the satellite trajectory are shown, and again the vertical lines emphasize the phasing between parameters. The entire data set was obtained in 14.7 min at a satellite speed of 8.6 km^{-1} (Reber et al, 1975⁴³)

with a simple picture of wave-like density enhancements in the major species nearly in phase with the vertical component of the perturbation velocity, ..."

Later analysis of the OSS data obtained on the AE-C satellite (Potter et al, 1976⁴⁴) has shown the amplitudes of the waves increase at the high-latitude auroral regions, indicating that the waves were apparently generated by magnetic storm energy deposition and propagate both northward and southward from the region of the auroral electrojet. An example of the OSS results are shown in Figure 11. It is expected that similar wave structure would appear in the infrared radiation due to CO_2 from these regions, as the spatial variations in the CO_2 that result from mass motions are expected to be similar to that of Ar.

The momentum source is one of the features of the thermosphere that manifests itself in significant high-latitude structure during periods of enhanced geomagnetic activity. The momentum source manifests itself by a pressure gradient due to momentum transfer to neutrals from ions accelerated by electric fields.

44. Potter, W.E., Kayser, D.C. and Mauersberger, K. (1976) Direct measurements of neutral wave characteristics in the thermosphere, *J. Geophys. Res.* 81: 5002-5012.

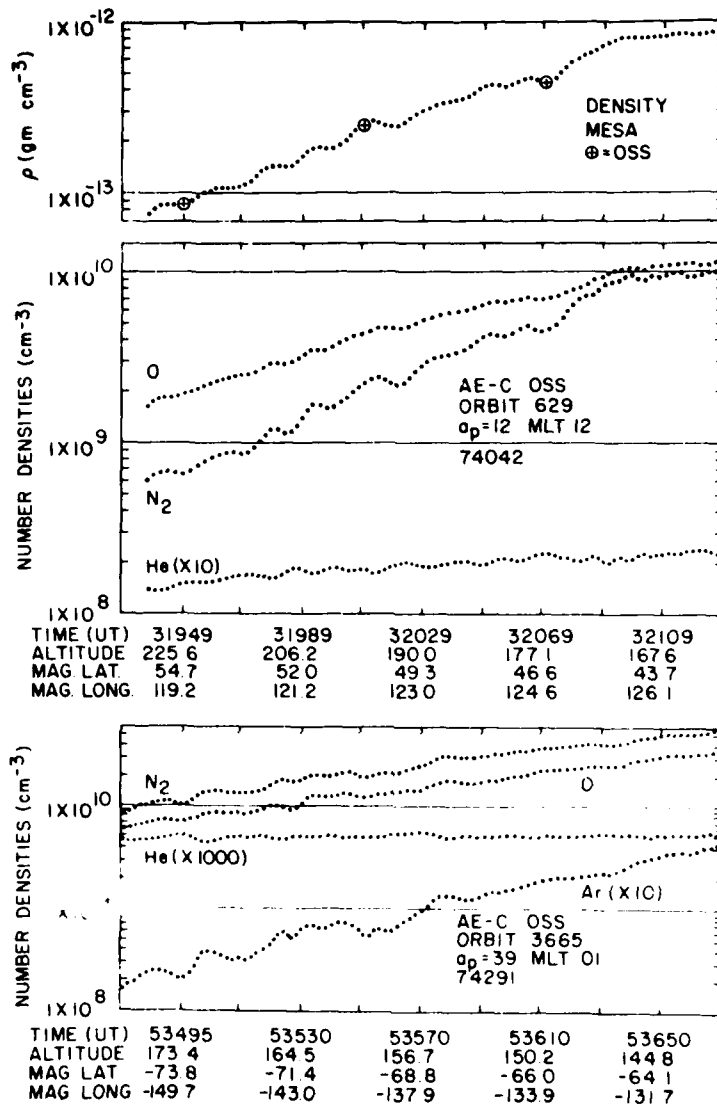


Figure 11. The Center and Bottom Panels Show OSS Neutral Number Densities for Two Elliptical Orbits. The mass dependent wave structure is evident, as is the out-of-phase behavior of He. The top panel shows the total Mesa mass density from orbit 629, that closely follows the OSS N₂ number density in the center panel. The circled pluses shown in the top panel are mass densities calculated from OSS constituent number densities. Altitudes are given in km. The (O) densities represent the total atmosphere oxygen. The universal time (UT) is given in sec after the start of the day

Perturbations in the structure of the neutral atmosphere in narrow latitude bands near the dayside polar cusp have been measured aboard the S3-1 and Esro 4 satellites (Trinks et al, 1978a⁴⁵). Examples of these perturbations are shown in Figures 12 to 14. Figures 12 and 13 present measurements made aboard the S3-1 satellite. These measurements show fluctuation amplitudes of as much as a factor of two in species concentrations and with spatial dimensions of approximately 300 km. Figure 14 presents the measurements made aboard the Esro 4 satellite and indicate similar magnitudes and extents. Trinks et al, (1978b)⁴⁶ discuss these measurements and suggest that thermospheric winds driven by "momentum sources" associated with ion convection are the predominant cause for these disturbances. The narrow spatial structure and in phase response of all species are characteristics associated with the momentum source. These effects are generally superimposed on the thermosphere expansion changes caused by Joule heating. Momentum source disturbances probably generate waves which are propagated to lower latitudes.

3.3 Ionospheric Response to Geomagnetic Activity

Ion densities have been measured on a number of satellite flights. The effects of increased geomagnetic activity on the ionic concentration can be seen by comparing Figures 15 and 16. Figure 15 shows ion species concentrations during a quiet period and displays the typical structure of the F layers. In Figure 16 the normal F₂ layer at high latitudes is severely changed during a period of high geomagnetic activity ($K_p = 6$). In the disturbed region there is a large amount of spatial structure of scale sizes of tens of km. The O⁺ is decreased in the F₂ peak due to the effect of the electric fields that increase the loss rate of the ion molecule reactions with N₂ and O₂. The substantial increase in the N₂⁺ is due to enhanced ionization by the precipitating particles.

3.4 Summary

Measurements of the total density below 90 km reveal substantial structure with scale sizes that are in agreement with theoretical predictions of gravity wave theory and tidal theory. At higher altitudes gravity waves are also apparent but with longer wavelengths (tens of km). Satellite observations reveal wave structure in the species concentrations with scale sizes from tens of km to several hundred

45. Trinks, H., Mayr, H.G. and Philbrick, C.R. (1978a) Momentum source signatures in thermospheric neutral composition, J. Geophys. Res. 83:1641-1646.

46. Trinks, H., Offerman, D., von Zahn, U. and Steinhauer, C. (1978b) Neutral composition measurements between 90 and 220 km altitude by rocket-borne mass spectrometer, J. Geophys. Res. 83:2169-2176.

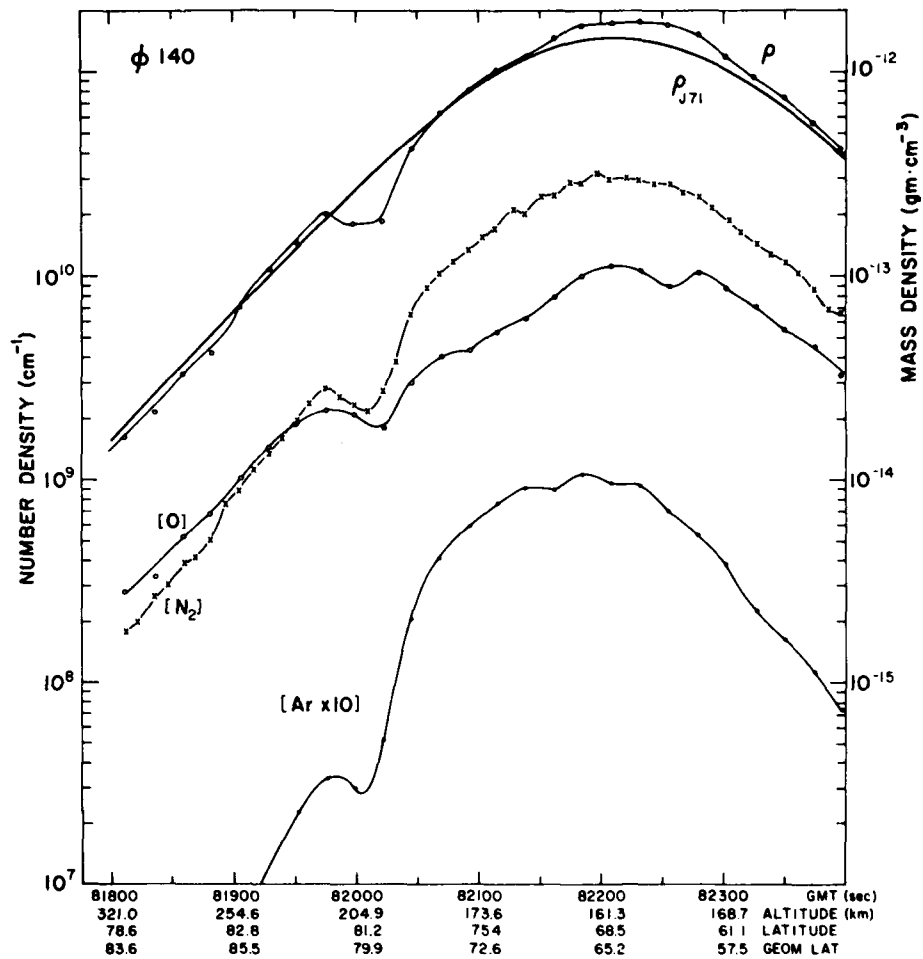


Figure 12. Perturbation in the Structure of the Atmospheric Mass Density and Species Concentrations Measured by Mass Spectrometer During S3-1 Satellite Flight

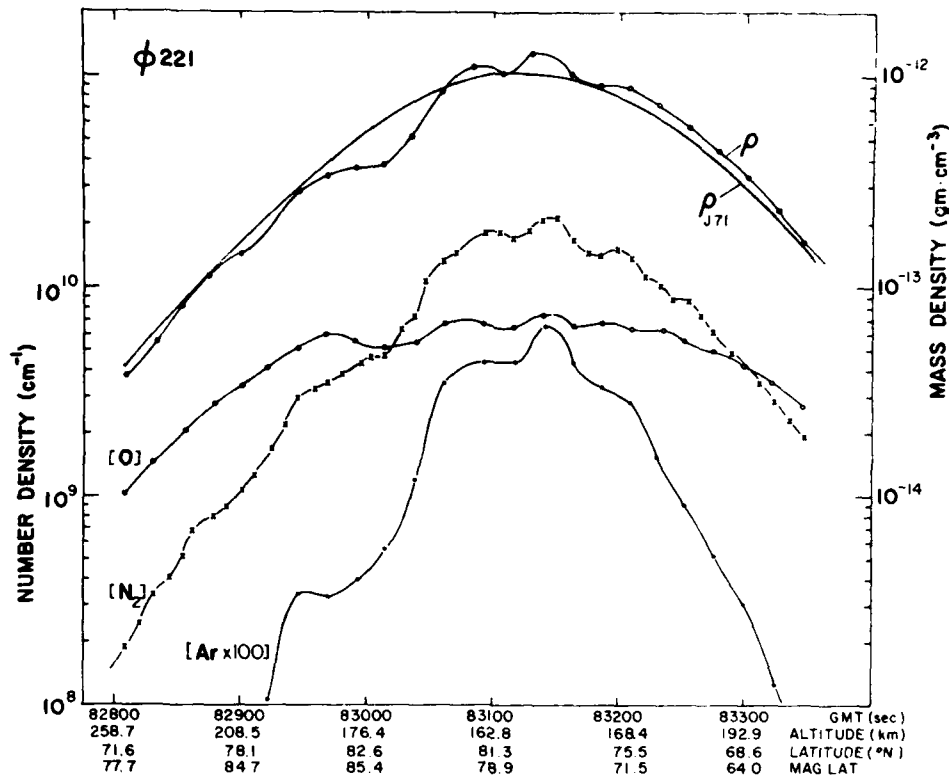
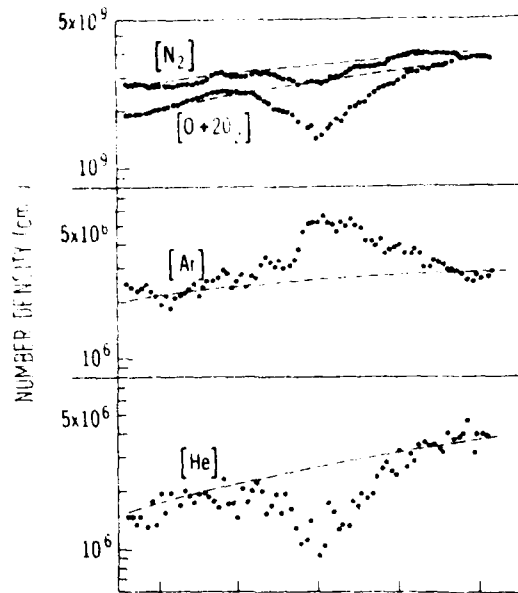


Figure 13. Severe Perturbation in the Structure of the Atmospheric Mass Density and Species Concentrations Measured by Mass Spectrometer During S3-1 Satellite Flight

kilometers. The description of these small-scale features of atmospheric variations would require a great deal of knowledge concerning the sources of the particular disturbance, as well as detailed 3-D calculations of atmospheric motion. This is not feasible at the present time and one must rely on a statistical description of the magnitude, spatial scale-size distribution, and frequency. With such a description it should be possible to evaluate the variability of the resultant infrared radiance.

Figures 17 and 18 give indications of the scales and amplitudes of waves and other structure features that have been observed in the upper atmosphere. In Figure 17 the range of theoretically predicted scale sizes for gravity waves (Hines, 1960¹¹) and tidal oscillations (Forbes, 1978⁹) are shown for both the vertical and horizontal structure. On the outside edge of the figure, several of the structure scales that have been measured (most are from examples shown earlier in this



UT (7 Apr 1974)	10 06		10 11		10 16
LST (hours)	23.7	21.8	12.5	12.2	12.1
HEIGHT (km)	208.7		207.4		210.5
GEOGR LAT N	79	88	81	71	61
GEOGR LONG E	204	176	35	31	29

Figure 14. Ambient Number Densities of Molecular Nitrogen, Total Oxygen, Argon, and Helium from the Esro 4 Gas Analyzer vs Universal Time, Height, and Geographic Coordinates. The disturbance is centered at 1011 UT (Trinks et al, 1978a, 1978b⁴⁶)

chapter) are indicated. There is satisfying consistency between the scales predicted for gravity waves and tidal oscillations and the structure scales that have been measured in the atmosphere. One of the open questions is the minimum scale size to be considered for localized heating, such as auroral arcs and precipitation sources. It may be that the smaller scale sizes needed for consideration in infrared radiance characterization are determined by these excitation mechanisms. In Figure 18 the altitude distribution of the measured scale sizes are given for a number of cases from the results discussed in this report. The amplitude of the structure is indicated by the length of the plotted lines. The interesting point to notice is that at low altitudes, the characteristic scale sizes are typically one to a few km and amplitudes are a few percent. If moving to

S-IV REV. NO. 1581.0
 DAY OF ORBIT 3/9/75

PERIOD
 ALTITUDE: 153.84
 LONGITUDE: 226.56
 LATITUDE: -20.89
 GMT(SEC.): 59251.1 (1627M)
 LOCAL TIME 0733 (M)
 IN SUN FROM 66570 TO 59250.

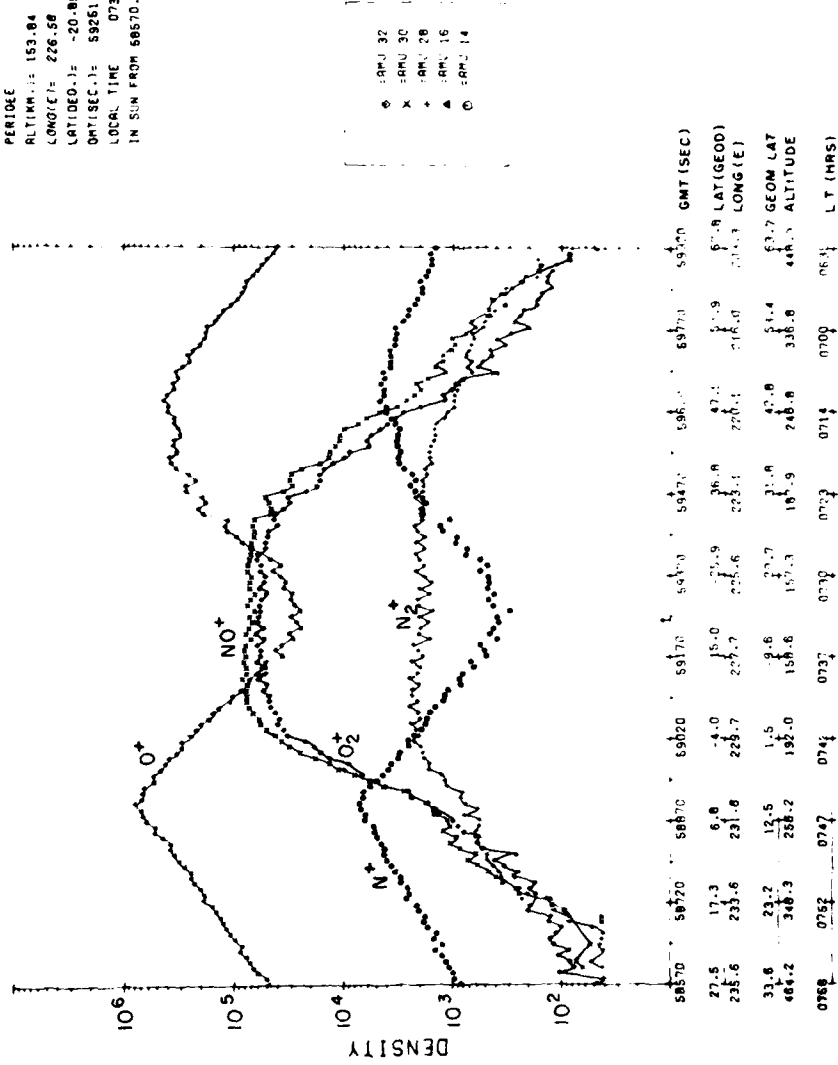


Figure 15. Ion Species Concentrations Measured by MS-IV Satellite During Quiet Magnetic Conditions

MS-IV REV. NO. 1556-2
 DATE: 08B 3.1.75

PERIGEE ALTITUDE: 152-92
 LONGITUDE: 169-08
 LATITUDE: 19-05
 GMT: 73052.7 (2017H)
 LOCAL TIME: 0733 (M)
 IN SUN FROM: 72370 TO 73720

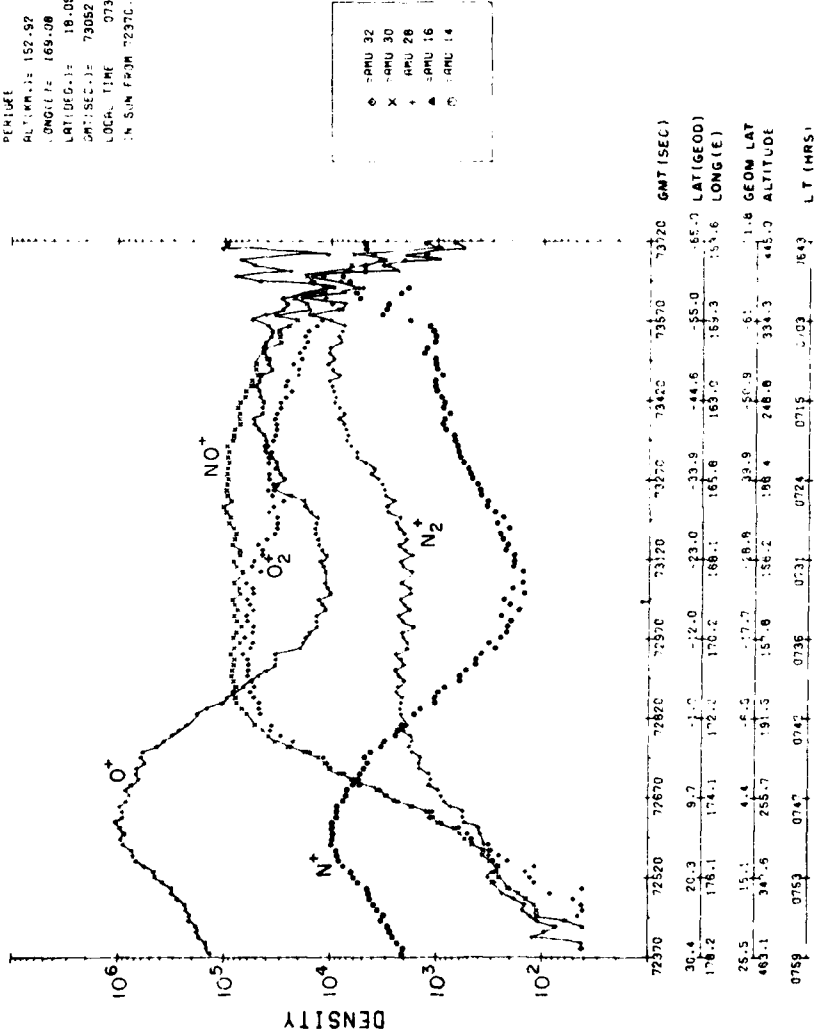


Figure 16. Ion Species Concentration Measured by Instruments Aboard MS-IV Satellite During Disturbed Magnetic Conditions ($K_p = 6$)

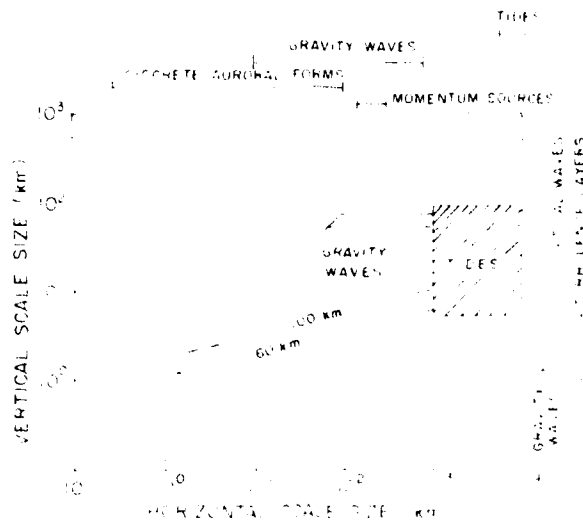
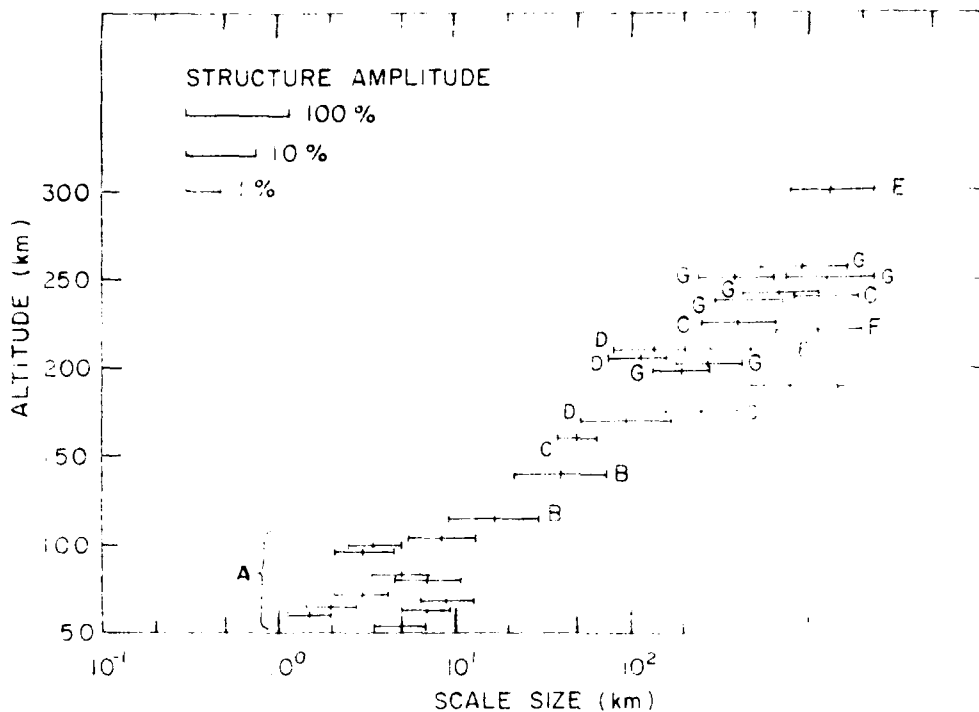


Figure 17. Theoretical Scale Sizes for Gravity Waves and Tidal Oscillations. Outside edges indicate measured scale sizes.

higher altitudes the amplitude and scale size both increase. While it is certainly not a complete picture, it does present an idea of the typical behavior under moderately disturbed atmospheric conditions. These considerations apply to the total density of the atmosphere. The structure and variability of an individual minor species may be substantially greater.

From this review, we conclude that substantial variations occur in the density distribution of the infrared radiating species of the atmosphere, both spatially and temporally. This chapter has only discussed the variations and scales associated with the species concentrations, but the excitation processes may be more important to the radiance under some circumstances. At present it is difficult to determine the full impact of these variations on the resultant infrared radiance. It can be inferred, for example, that the density of CO_2 at 150 km would be expected to increase by more than a factor of ten under high latitude geomagnetic heating. With the calculations discussed elsewhere in this report and with the data presented here these questions can begin to be answered.



- A. Rocketborne accelerometer, Philbrick et al, 1978a⁴⁷
- B. Rocketborne mass spectrometer, Trinks et al, 1978b⁴⁶
- C. AE-C satellite mass spectrometer, Reber et al, 1975⁴³
- D. AE-C satellite mass spectrometer, Potter et al, 1976⁴⁴
- E. S3-1 satellite mass spectrometer, Philbrick, 1976⁴⁸
- F. S3-1 satellite mass spectrometer, Trinks et al, 1978a⁴⁵
- G. S3-4 satellite density gauge, McIssac, 1979⁴²
- H. S3-1 satellite mass spectrometer, Philbrick, 1980⁴⁹

Figure 18. Altitude Distribution of Measured Scale Sizes from Indicated Sources. Amplitude of structures are indicated by length of plotted line. The rocketborne data show vertical structure and the satellite shows horizontal structure

- 47. Philbrick, C.R., Faire, A.E., and Fryklund, D.H. (1978a) Measurements of Atmospheric Density at Kwajalein Atoll, 18 May 1977, AFGL-TR-0058, AD A054 784.
- 48. Philbrick, C.R. (1976) Recent satellite measurements of upper atmospheric composition, Space Research XVI:289-295.
- 49. Philbrick, C.R. (1980) Private communication.

4. ATMOSPHERIC BACKGROUND CLUTTER ANALYSIS

Preliminary calculations (Titus and Anapol, 1979⁵⁰) of the noise or clutter produced by fluctuations in the CO₂ radiation have been made using a model based on satellite mass spectrometer measurements of density variations in the upper atmosphere combined with estimates of the mean radiance along a path obtained from the High Altitude Radiance Model. CO₂ is the dominant radiator throughout much of the infrared, but it is one of the most difficult molecules to measure using mass spectroscopy. Because of this difficulty, CO₂ density data at higher altitudes are almost nonexistent and, therefore, Ar data (Figure 19(a)) was taken to be approximately representative of CO₂. As discussed in Section 3, Reber et al (1975)⁴³ have published spatial density variations for AR at high altitudes (see Figure 10). Using the assumption that the radiance is directly proportional to molecular density, the power spectrum (PSD) of the radiance spatial structure was derived from these data. The correlation length is found to be approximately 10 km and the roll-off of the PSD is f^{-2} (Figure 19(b)) where f is the spatial frequency. Satellite ionosphere density (SRI wideband experiment) measurements at these altitudes and accelerometer and calorimeter measurements appear to confirm these values. The large-scale correlation length of the AE-C mass spectrometer data is approximately 450 km. This length is corroborated by the SPIRE data and S3-1 mass spectrometer measurements.

The impact of radiance structure on a sensor inbedded in the limb is as shown in Figure 19(c). A shell model of radiance is constructed at correlation intervals and the power spectrum calculated for each intersection of the line-of-sight and a shell. The power spectrum is integrated at each range point to obtain the mean square clutter in the sensor passband and these values summed along range to obtain the integrated mean square clutter noise.

Measurements during aurorally active conditions exhibit much larger density variability and smaller correlation lengths. In addition, the fluctuations of Ar were observed to be much larger than those of N. This mass dependence translates into a spectral dependent model of clutter since each species will behave differently. Large radiance enhancements during aurora have been measured at shorter wavelengths and are theoretically expected at longer wavelengths. Therefore (and not unexpected), the impact of the disturbed upper atmospheric conditions will be more severe than the quiescent atmosphere.

50. Titus, J. and Anapol, M. (1979) Private communication.

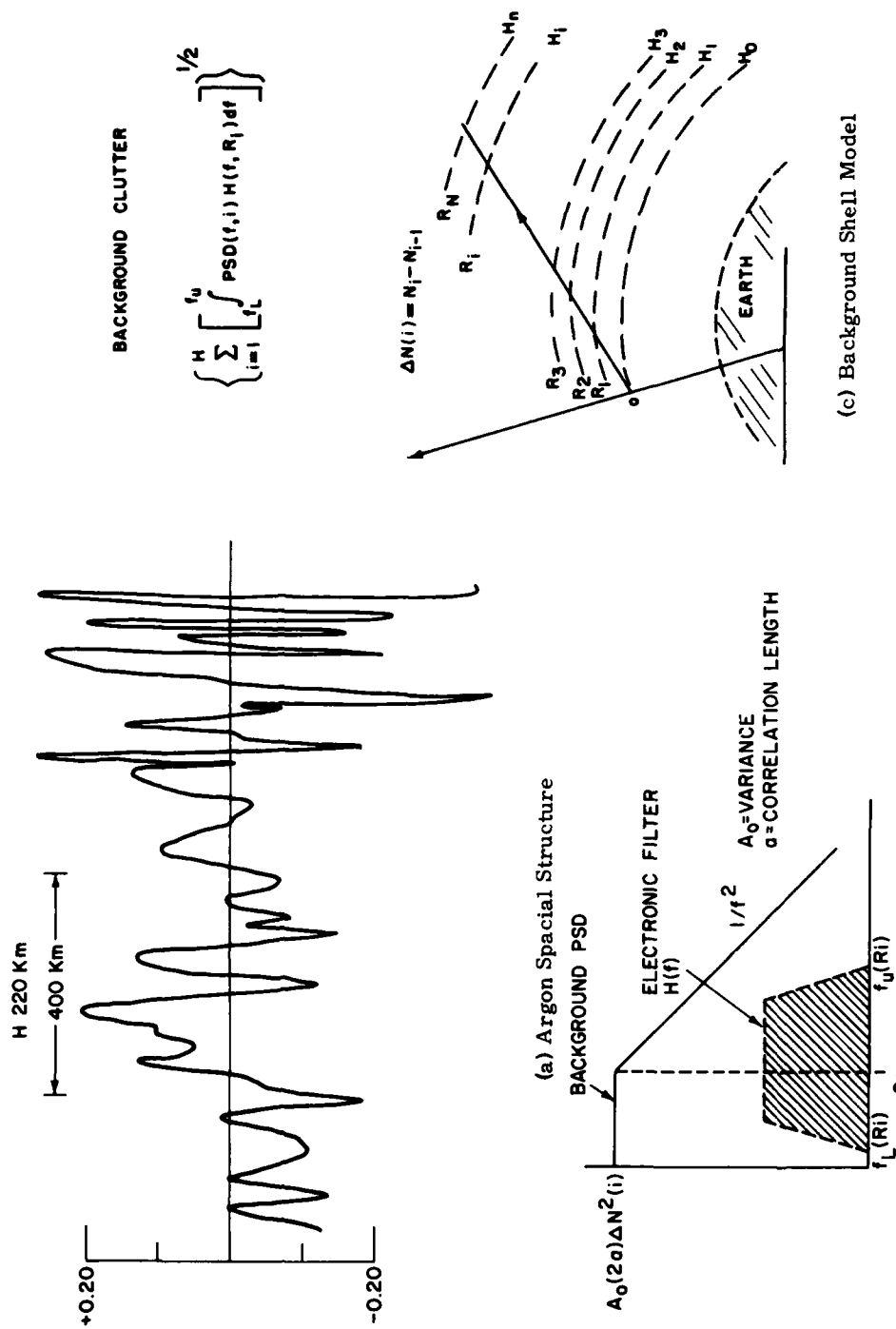


Figure 19. Atmosphere Background Clutter Analysis

5. AURORAL EXCITATION OF INFRARED RADIATORS

Even if the concentration and density distribution of each of the potential infrared emitters were known, the radiance at high latitudes may be difficult to predict because of the fluorescence and direct collisional excitation sources together with localized temperature enhancements. In this section a brief discussion will be given of several sets of information that are related to the energy sources that input to the upper atmosphere. The energy input in the auroral zone may be studied by examining the ionospheric response, particularly the N_2^+ enhancement due to particle ionization and the O^+ depletions due to the electric field produced increases in ion molecule loss reactions. The visible radiation from all-sky cameras on DMSP satellite photographs provide an excellent means of characterizing the location, structure, and intensity of energy deposition. Ground-based video recording systems have also been used to study the auroral characteristics. A recent satellite ultraviolet photometer, Huffman et al, (1979),⁵¹ has also provided nadir looking data on the ultraviolet emission excited in the auroral zones. In Figure 20 measurements of the radiation at 155 nm (the Lyman-Birge-Hopfield band of molecular nitrogen), from a 20° portion of the auroral oval showing arcs and continuous aurora, are presented.

An aurora is a region of considerable variability of luminosity. In spatial extent it may vary in width from the order of km to hundreds of km, and in length in thousands of km. The structure is very heterogeneous and, thus, the aurora is potentially a significant source of fluctuating infrared radiation. Examples which show the variety of auroral forms that may be encountered are shown in Figure 21, from the DMSP satellite system operating in the infrared. The land mass outlined by the lights is the eastern part of the United States.

In addition to the well-known visible aurora, typified by the DMSP photographs, we may have the occurrence of midlatitude auroral red arcs during periods of high magnetic activity. These occur to the south of the southern extension of the visible aurora, Figure 22, (N. B. S., 1962⁵²) have widths of the order of several hundred km, and extend for thousands of km in longitude. These arcs are characterized by a predominance of the 630 nm O line. Their altitudes are typically above 300 km.

In Figure 23 ion concentrations are shown for two satellite flights through auroral disturbances. In both cases the aurora were Class III. The ion concentrations display the high degree of irregularity to be expected under such circumstances.

51. Huffman, R. E., LeBlanc, F. J., Larrabee, J. C. and Paulsen, D. E. (1979) Satellite Atmospheric Radiance Measurements in the Vacuum Ultraviolet, AFGL-TR-79-0151, AD A078 628.

52. N. B. S. (1962) Auroral arcs in mid-latitudes, National Bureau of Standards Technical News Bulletin 46:42-46.

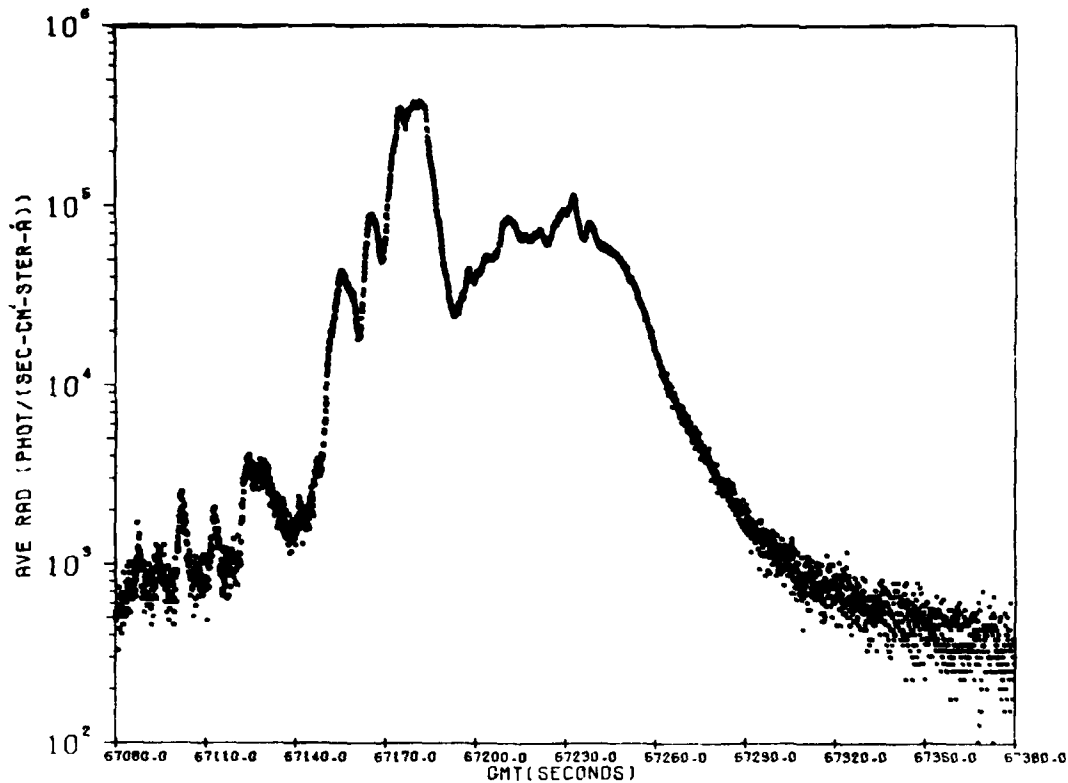


Figure 20. Radiation at 155 nm (Lyman-Birge-Hopfield) for a 20° Portion of the Auroral Oval

5.1 Application of Visible Monochromatic Auroral Imaging Data for Modeling Infrared Radiance

Effective design of sensitive infrared sensors operating in the limb viewing mode requires a statistically significant data base on the auroral infrared earthlimb background. Research that has been performed under the JNA/AFGL auroral measurements program has shown that there are strong auroral emissions near 2.7 and 4.3 μm (Stair et al, 1981⁵). It is possible to develop, to first order, a comprehensive 2.7 and 4.3 μm earthlimb model that is based on an existing all-sky TV data base. The TV data base includes approximately 200 hours of all-sky multispectral image intensified TV imaging data of aurora and airglow that have been taken and stored on video tape in the time period 1972 through 1977. Methods for modeling (blue red input model, BRIM) infrared emissions at 2.7 and 4.3 μm on the basis of ground-based photometric measurements of the aurora in the spectral regions blue (4278Å) and red (6300Å) have recently been developed and verified against infrared data that were obtained simultaneously via rocketborne sensors.



Figure 21. DMSP Infrared Photographs of Various Auroral Forms

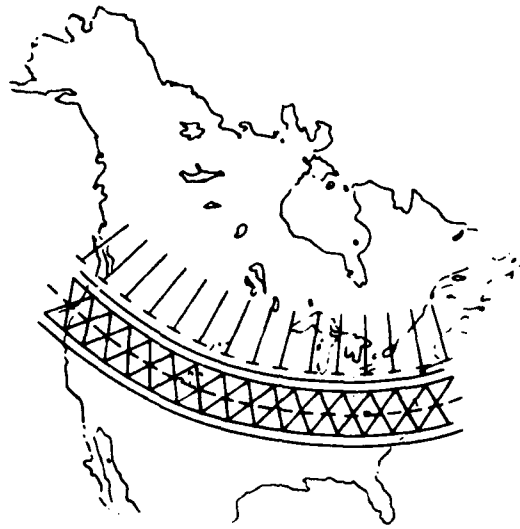


Figure 22. The Red Arc (shaded region) Lies South of the Southern Extension of the Visible Aurora (_)

In this section the use of the BRIM capability to construct images of the infra-red earthlimb radiance from successive pairs of blue and red all-sky TV images is discussed. The images are obtained at a rate of once every 15 sec or faster. The spatial resolution of the TV is such that structure on the scale of several km may be resolved in the radiance images. The all-sky TV coverage has a zenith full cone angle of 160° . This is extensive enough so that images of horizontal extent of up to 700 km and tangent altitude from 40 to 140 km may be constructed. Spatial power spectral densities (PSDs) may be obtained from the images and temporal PSDs may be obtained from a series of images.

Methods inferred from the work reported by Rees and Luckey (1974)⁵³ may be used to approximately construct an energy deposition profile $q(z, t)$ from the TV brightness data measured in narrow spectral bands in the blue (4278Å) and in the red (6300Å) spectral region. The "blue" data $4\pi I_B(t)$ are proportional to the height integrated energy deposition and the ratio I_B/I_R of the blue to red may be associated with the altitude where q is a maximum if one assumes that the energy dependence of the incident electrons takes the form $\phi = \phi_0 E e^{-E/a}$. Kumer (1977)⁵⁴

53. Rees, M.H. and Luckey, D. (1974) Auroral electron energy derived from ratio of spectroscopic emissions, *J. Geophys. Res.* 79:5181-5186.

54. Kumer, J.B. (1977) Further Evaluation of ICECAP Auroral 4.3 μ m Zenith Radiance, Haes Report No. 57 DNA 4260F.

MS-IV REV. NO. 383-0
 ORY OF ORBIT 12/ 2/74

PER. JEE
 ALTITUDE J= 159.57
 LONGITUDE J= 6.08
 LATITUDE J= 66.49
 GMT (SEC.) J= 74071.2 (2034M)
 LOCAL TIME 2106 (M)
 IN SUN FROM 74422. TO 74740.
 IN SHADE FROM 73390. TO 74422.

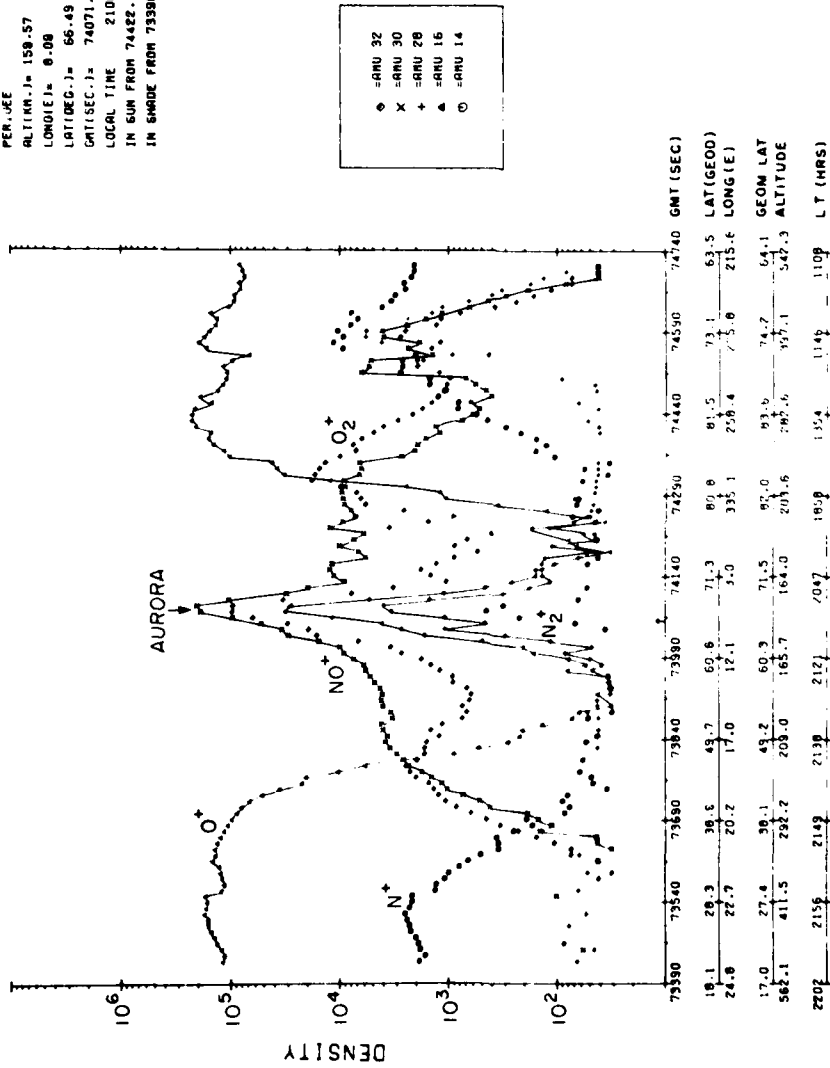


Figure 23. Ion Species Concentrations Measured by Instruments Aboard MS-IV Satellite During Auroral Activity

discussed in detail the BRIM method for approximately constructing a deposition profile $q(z, t)$ from the blue and red brightness data. Examples of the excellent agreements between the up and down leg BRIM calculations for $4.3 \mu\text{m}$ zenith radiance and the data obtained in the case of the an auroral event of 25 February 1974 are shown on Figures 24 and 25. Ground-based photometric red and blue auroral data taken at the point of up-leg and downleg penetration at 80 to 110 km are input to the BRIM model.

The goal is to use a series of TV frames of blue data $4\pi I_B$ to generate a dynamic image of the corresponding infrared earthlimb radiance as it would appear when viewed from a satellite at some considerable distance from the earth. Line-by-line (or selected line) digitization of auroral images and image sequences is accomplished with a system which incorporates a controller that selects the proper TV frame, a digitizer, and an output couple to transfer the digital data stream to digital magnetic tape.

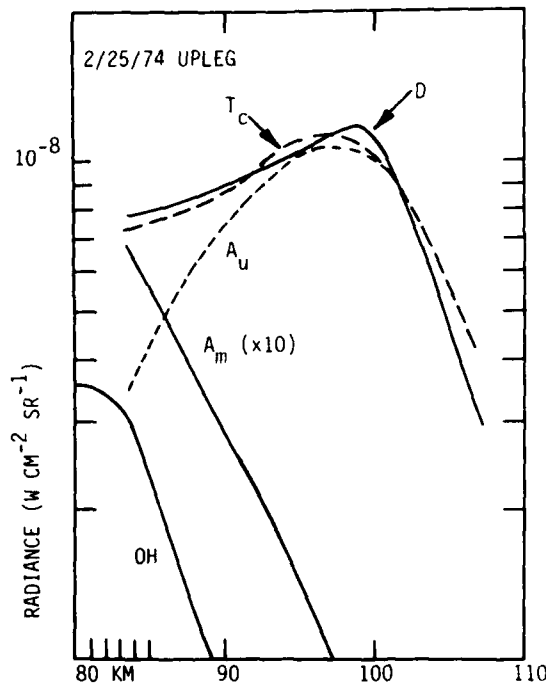


Figure 24. 25 February 1974 Upleg $4.3 \mu\text{m}$ Zenith Radiance Data (curve D) are Compared With Curves A_u , the BRIM Calculation for the Auroral Component of Zenith Radiance; OH, the Calculated Component Due to Vibration Transfer from OH^+ ; $A_m(x10)$, the Ambient Thermal Component Multiplied by a Factor 10 So That It is on Scale; and T_c , the Sum $\text{OH} + A_u + A_m$

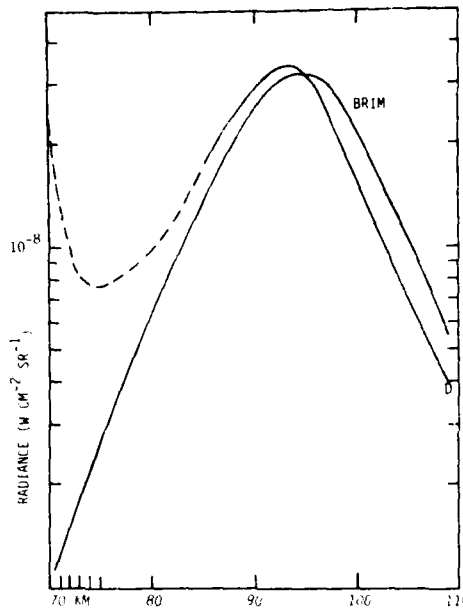


Figure 25. A Comparison of the 25 February 1974 Downleg Data (curve D) and Calculations (curve BRIM) Based on Our BRIM Model

To date Kumer and associates have developed software for the calculation of 2.7 and 4.3 μm earthlimb radiance from digitized blue and red zenith viewing all-sky TV data. Due to the lack of mass digitization of the TV data base at this time a version of the simulated TV data has been utilized to test the software. In this simulation of the earthlimb, radiance is calculated along 51 lines-of-sight with tangent altitude 110 km. The middle line-of-sight passes directly over the zenith of the TV station. The surface projection of this line-of-sight runs from magnetic northwest to southeast and is 30° magnetic south of due magnetic east. The lines-of-sight are parallel, 2 km apart, and tangent at 110 km altitude.

The earthlimb radiance calculations are performed on 50 pairs of simulated blue/red digitized TV data frames. These pairs of frames are spaced in time by 20 sec and thereby define an interval $0 < t < 16.67$ min. The first pair was generated from scanning photometer data. This initial pair is considered to represent a *steady-state* condition that had persisted for many min prior to $t = 0$ min.

At $t = 0$ it is assumed that a multiple arc structure appears in the field of view (FOV) and commences to move across the FOV in the positive direction perpendicular to the lines-of-sight. In the blue and red TV data the multiple arc structure is represented sinusoidally by

$$4\pi I_B = 10 (1 - \cos 2\pi k(x - vt))$$

and

$$4\pi I_R = 4\pi I_B/10,$$

where $k = 0.1 \text{ km}^{-1}$, $v = 7.14 \text{ km/min}$, and the brightness units are kilo-Rayleighs (kR). The structure is assumed uniform along lines parallel to the lines-of-sight.

Results for the earthlimb radiances calculated on the middle line-of-sight (that is, $x = 0$) on the time interval $0 < t < 16.67 \text{ min}$ are shown on Figure 26. One can see the $2.7 \mu\text{m}$ emission tracks the temporal structure of the simulated moving auroral arcs. This results from the fact that the response time of the $\text{N}(\text{2D})$ mechanism for $2.7 \mu\text{m}$ auroral emission, about 0.5 sec at 110 km, is considerably shorter than the period ($\approx 1.67 \text{ min}$) of the simulated aurora. The response time for the CO_2 $4.3 \mu\text{m}$ aurora at 110 km is approximately 16 min, considerably longer than the period of the auroral excitation. This explains the temporal behavior of the auroral CO_2 $4.3 \mu\text{m}$ earthlimb radiance as shown on Figure 26. This radiance asymptotically approaches an equilibrium DC level ($\approx 1.8 \times 10^{-7} \text{ w/cm}^2 \text{ sr}$) near $t = 16.67 \text{ min}$. It also displays a small 1.67 min period ripple in response to the aurora. The amplitude of the CO_2 $4.3 \mu\text{m}$ ripple is about 30 times less than the amplitude of the NO $2.7 \mu\text{m}$ radiance. Also despite the fact that it is well known that the DC level for vertically viewed auroral CO_2 $4.3 \mu\text{m}$ emission is much larger than for NO auroral $2.7 \mu\text{m}$, we see that in viewing on the limb CO_2 $4.3 \mu\text{m}$ self absorption renders the average radiance values about equal for these two emissions.

The steady-state spatial structure at $t = 0$ is shown on Figure 27. The positive gradient results from the north sky position of measurements of an arc of 26 October 1978 with respect to the position of the scanning photometer that obtained the data that are used to generate the first frame pair of simulated digitized TV data.

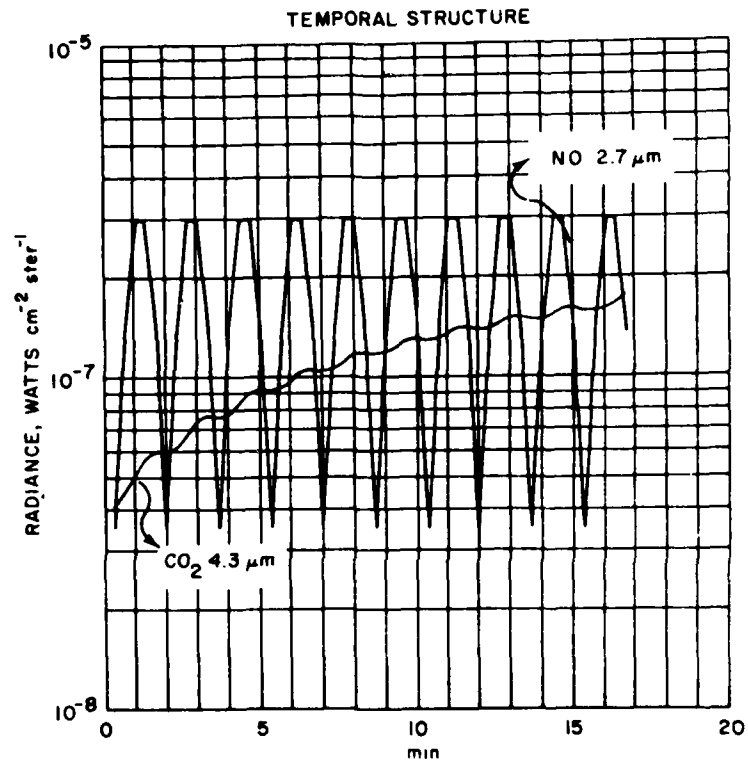


Figure 26. Temporal Dependence on Line-of-Sight Passing Directly Overhead TV Station at 110 km Tangent Altitude on the $0 \leq t \leq 16.63$ min Interval. Projected view direction is approximately 120° southeast of due magnetic north

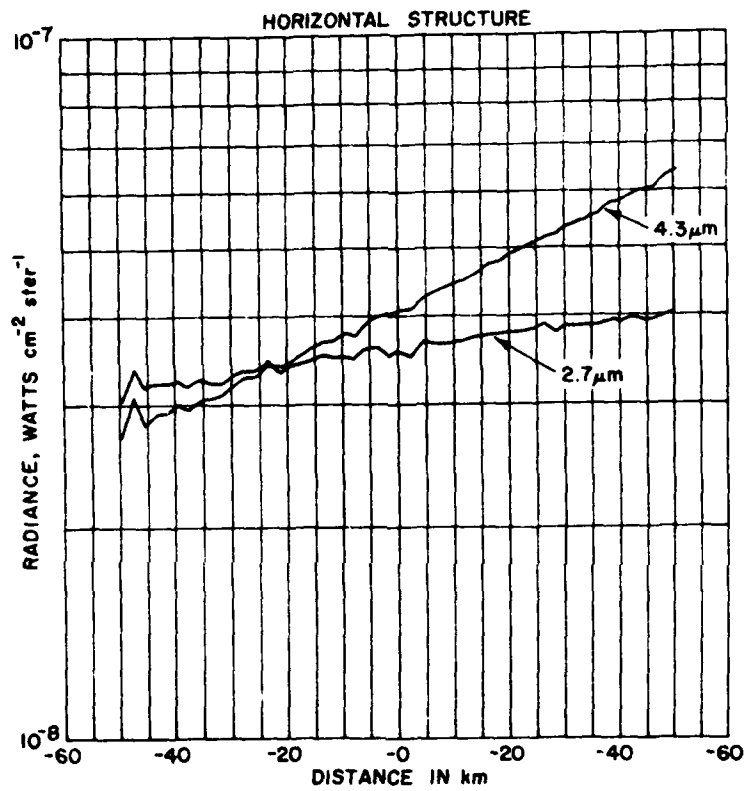


Figure 27. Horizontal Structure in Simulated Steady-State at $t = 0$, Based on Photometric Data Obtained 26 October 1978 by R. D. Sears⁵⁵

55. Sears, R. D. (1979) Private communication.

References

1. Siebert, M. (1954) Zur theorie der thermischen erregung gezeitenaitiger schwingung der erdatmosphäre. Z. Naturwissenschaften 41:446.
2. Sen, H.K. and White, M.L. (1955) Thermal and gravitational excitation of atmospheric oscillations, J. Geophys. Res. 60:483-485.
3. Chapman, S., and Lindzen, R.S. (1970) Atmospheric Tides, D. Reidel, Hingham, Mass.
4. Forbes, J.M. and Garrett, H.B. (1978) Solar diurnal tide in the thermosphere, J. Atmos. Sci. 35:148-208.
5. Forbes, J.M. and Geller, M.A. (1972) Lunar semidiurnal variation in OI (5577Å) nightglow, J. Geophys. Res. 77:2942-2947.
6. Petitdidier, M. and Teitelbaum, H. (1977) Lower thermosphere emissions and tides, Planet Space Sci. 25:711-721.
7. Harris, I. and Mayr, H.G. (1975) Diurnal variations in the thermosphere, J. Geophys. Res. 80:3925-3933.
8. Mayr, H.G. and Harris, I. (1977) Diurnal tide, composition, and winds, J. Geophys. Res. 82:2628-2640.
9. Forbes, J.M. (1978) Tidal variations in thermospheric O, O₂, N₂, Ar, He, and H, J. Geophys. Res. 83:3691-3698.
10. Forbes, J.M. and Marcos, F.A. (1979) Seasonal-latitudinal tidal structures of O, N₂, and total mass density in the thermosphere, J. Geophys. Res. 84:31-35.
11. Hines, C.O. (1960) Internal atmospheric gravity waves at ionospheric heights, Can. J. Phys. 38:1441-1481.
12. Georges, T.M. (1968) HF Doppler studies of traveling ionospheric disturbances, J. Atmos. Terr. Phys. 30:735.
13. Thome, G.D. (1968) Long-period waves generated in the polar ionosphere during the onset of magnetic storms, J. Geophys. Res. 73:6319-6336.
14. Dachs, J. (1968) Die helligkeiten des nachtllichen luftleuchtens wahrend des sommerflechen minimums nach messungen in Sudwestafrika, Beitr. Phys. d. Atmosphere 41:184-215.
15. Armstrong, E.B. (1975) The influence of a gravity wave on the airglow hydroxyl rotational temperature at night, J. Atmos. Terr. Phys. 37:1585-1592.
16. Silverman, S.M. (1962) Unusual fluctuations of 5577Å O I airglow emission intensity on October 28-29, 1961, Nature 195:481-482.
17. Okuda, M. (1962) A study of excitation process in niglet airglow, Sci. Rep. Tohoku Univ. 5th Ser. Geophysics, 14:9-26.
18. Press, F. and Harkrider, D.G. (1962) Propagation of acoustic-gravity waves in the atmosphere, J. Geophys. Res. 67:3889-3908.
19. Pfeffer, R.L. and Zarichny, J. (1963) Acoustic-gravity wave propagation in an atmosphere with two sound channels, Geophys. Pure and Appl. 55:175-199.
20. Harkrider, D.G. and Wells, F.J. (1968) Acoustic-Gravity Waves in the Atmosphere-Symposium Proceedings, T.M. Georges, (ed.) U.S. Government Printing Office, Washington, D.C., pp. 299-314.

21. Friedman, J. P. (1966) Propagation of internal gravity waves in a thermally stratified atmosphere, J. Geophys. Res. 71:1033-1054.
22. Reddy, C. A. (1969) Internal Gravity and Acoustic Waves, A Colloquium, NCAR-TN-43, pp. 229-240.
23. Tuan, T. F. (1976) Research in Gravity Waves and Airglow Phenomena, AFGL-TR-76-0296, AD A040 014.
24. Richmond, A. D. (1978) Gravity wave generation, propagation and dissipation in the thermosphere, J. Geophys. Res. 83:4131-4145.
25. Porter, H. S., Silverman, S. M. and Tuan, T. F. (1974) On the behavior of airglow under the influence of gravity waves, J. Geophys. Res. 79: 3827-3833.
26. Peterson, A. W. and Kieffaber, L. M. (1973) Infrared photography of OH airglow structures, Nature 242:321-323.
27. Kieffaber, L. H. and Peterson, A. W. (1978) Correlation studies of four submicron OH airglow bands during spacelab simulation, J. Atmos. Terr. Phys. 40:1339-1345.
28. Peterson, A. W. (1979) Airglow events visible to the naked eye, Applied Optics 18:3390-3393.
29. Chiu, Y. T. and Ching, B. K. (1978) The response of atmosphere and lower ionospheric layer structures to gravity waves, Geophys. Res. Lett. 5:539-542.
30. Hatfield, R., Tuan, T. F. and Silverman, S. M. (1981) On the effects of atmospheric gravity waves on profiles of H, O₃, and OH emission, J. Geophys. Res. 80:2429-2437.
31. Wienstock, J. (1978) Theory of the interaction of gravity waves with O₂(¹Σ) airglow, J. Geophys. Res. 83:5175-5185.
32. Hodges, R. R. (1967) Generation of turbulence in the upper atmosphere by internal gravity waves, J. Geophys. Res. 72:3455-3458.
33. Tuan, T. F., Hedinger, R., Silverman, S. M. and Okuda, M. (1979) On gravity wave induced Brunt-Vaisala oscillations, J. Geophys. Res. 84:393-398.
34. Philbrick, C. R., Noonan, J. P., Fletcher, E. T., Jr., Hanrahan, T., Salah, J. E., Blood, D. W., Olsen, R. O. and Kennedy, B. W. (1978) Atmospheric Properties From Measurements at Kwajalein Atoll on 5 April 1978, AFGL-TR-0195, AD A061 083.
35. Hines, C. O. (1974) The Upper Atmosphere in Motion, American Geophysical Union Monograph 18.
36. Davis, M. J. and Da Rosa, A. V. (1969) Traveling ionospheric disturbances originating in the auroral oval during polar substorms, J. Geophys. Res. 74:5721-5735.
37. Newton, G. P., Kasprzak, W. F., Curtis, S. A. and Pelz, D. J. (1975) Local time variation of equatorial thermospheric composition determined by the San Marco 3 Nace, J. Geophys. Res. 80:2289-2299.
38. Sharp, L. R., Hickman, D. R., Rice, C. J. and Straus, J. M. (1978) The altitude dependence of the local time variation of thermospheric density, Geophys. Res. Lett. 5:261-263.
39. Philbrick, C. R., Murphy, E. A., Zimmerman, S. P., Fletcher, E. J., Jr., and Olsen, R. O. (1980) Mesospheric density variability, Space Research XX:79-82.

40. Howlett, L. C., Baker, K. D., Megill, L. R., Shaw, A. W., and Pendleton, W. R. (1980) Measurement of a structured profile of atomic oxygen in the mesosphere and lower thermosphere, J. Geophys. Res. 85:1291-1298.
41. Keneshea, T. J., Zimmerman, S. P. and Philbrick, C. R. (1979) A dynamic model of the mesosphere and lower thermosphere, Planet. Space Sci. 27:385-401.
42. McIssac, J. P. (1980) Private communication.
43. Reber, C. A., Hedin, A. E., Pelz, D. T., Potter, W. E. and Brace, L. H. (1975) Phase and amplitude relationships of wave structure observed in the lower thermosphere, J. Geophys. Res. 80:4576-4580.
44. Potter, W. E., Kayser, D. C. and Mauersberger, K. (1976) Direct measurements of neutral wave characteristics in the thermosphere, J. Geophys. Res. 81:5002-5012.
45. Trinks, H., Mayr, H. G. and Philbrick, C. R. (1978a) Momentum source signatures in thermospheric neutral composition, J. Geophys. Res. 83:1641-1646.
46. Trinks, H., Offerman, D., von Zahn, U. and Steinhauer, C. (1978b) Neutral composition measurements between 90 and 220 km altitude by rocket-borne mass spectrometer, J. Geophys. Res. 83:2169-2176.
47. Philbrick, C. R., Faire, A. E., and Fryklund, D. H. (1978a) Measurements of Atmospheric Density at Kwajalein Atoll, 18 May 1977, AFGL-TR-0058, AD A054 784.
48. Philbrick, C. R. (1976) Recent satellite measurement of upper atmospheric composition, Space Research XVI:289-295.
49. Philbrick, C. R. (1980) Private communication.
50. Titus, J. and Anapol, M. (1979) Private communication.
51. Huffman, R. E., LeBlanc, F. J., Larrabee, J. C. and Paulsen, D. E. (1979) Satellite Atmospheric Radiance Measurements in the Vacuum Ultraviolet, AFGL-TR-79-0151, AD A078 628.
52. N. B. S. (1962) Auroral arcs in mid-latitudes, National Bureau of Standards Technical News Bulletin 46:42-46.
53. Rees, M. H. and Luckey, D. (1974) Auroral electron energy derived from ratio of spectroscopic emissions, J. Geophys. Res. 79:5181-5186.
54. Kumer, J. B. (1977) Further Evaluation of ICECAP Auroral 4.3 μ m Zenith Radiance, Haes Report No. 57 DNA 4260F.
55. Sears, R. D. (1979) Private communication.

6. Summary and Recommendations

In this review of atmospheric variability and its effect on the variability of atmospheric infrared radiation, certain important problems are evident. The most important problem is the basic lack of measurements concerning the variability of the infrared radiance from the upper atmosphere. Such measurements are highly desirable and should be made at the earliest opportunity. Until these measurements are made the prediction of the atmospheric infrared radiation must rely on numerical codes such as the High Altitude Infrared Radiance Model described in Chapter 2. This model is well established and predictions made using it are in general agreement with the limited measurements that have been performed. However, the calculations do not include the effects of atmospheric variability. This must be included in future predictions as the capability of most systems of interest is limited principally by variations in the radiance that appear as false signals.

The models that describe the long-term variations in the atmospheric properties, which are the necessary input to codes that predict atmospheric radiation, are discussed in Chapter 3. The predictions of these models are in satisfactory agreement with measurements for the long-term variations; however, the models do not attempt to follow the short-term variations such as would be seen in frame-to-frame viewing. In particular, the Cole-Kantor low altitude model and the J77 model seem quite satisfactory for the prediction of the long-term variability. However, a problem of how to join these models near the homopause remains and must be examined further before satisfactory predictions of the radiance can be

made. The joining of the properties of these two models is currently under study. As both of these models describe only average or mean conditions over long periods of time, the most serious problems that arise in the use of disjoint models is in the calculation of spatially integrated radiance values and the interpretation of the calculated results of radiance when the limb passes through that transition region.

A second problem in the application of the models arises in prediction of the long-term variability of the minor species that are the major contributors to the infrared radiation. These predictions are based principally on theoretical models of atmospheric behavior and a limited number of measurements. However, these models are questionable for the minor species and must be examined in greater detail. Preliminary predictions of long term variability of the infrared radiation that are presented in Chapter 4 show the degree to which the limb radiance varies with altitude. The application of these results would change the effective limb altitude of a system that makes measurements near the horizon.

Data do exist on the long-term variability of minor species but at present they have not been fully analyzed. The quantity of data is still not sufficient to allow the minor species to be modeled to the degree that the major components of the atmosphere are modeled. At the lower altitudes these densities are best determined from rocket flights that should be continued in order to collect the amount of data of the time and space that is required. At higher altitudes satellite data are available and are being analyzed. However, most of the satellite data was obtained at altitudes above those where the principle radiation is emitted; thus, the total amount of data is limited. Under certain conditions, means other than direct sampling, such as radar returns and optical measurements, are available and should be pursued. Theoretical models that describe the chemistry and transport are also available and can be used under certain circumstances.

Another serious problem is the degree of the short-term temporal variability that would affect the frame-to-frame operation of staring measurement systems and the small-scale spatial variability that would affect the operation of scanning measurements. The available data concerning species concentrations are discussed in Chapter 5 and preliminary conclusions as the expected degree of the variability presented. There are data, such as the AL-C, -D, -E, and S3-1 satellite measurements, that should be analyzed further. The preliminary results of this analysis were used to construct a simplified model of the CO₂ radiance as discussed in Chapter 5 and applied to the calculation of a spatially integrated power spectral density for analyses of certain systems. It must be emphasized that the data presently available concerning the short-term variability are those on the species concentration and not on the infrared radiance variability. Thus, data on the short-term variability of the infrared radiance is very important before the

predictions of the radiance from species concentration can be fully accepted. These predictions do rely on basic knowledge of the processes that lead to infrared radiation. This study must be pursued and the results folded into the predictive models. Of course, this process requires measurements to be made of both the source and the emitted radiation, but not simultaneously for all cases.

Again, in the determination of the short-term variability many types of measurements can be used. The most useful source of data on the atmospheric constituents are measurements of species concentrations of the infrared emitters on a spatial and temporal scale that overlaps with system measurement parameters. Spatial dimensions are presently adequate and, as more data are available from satellite and rocket flights, *satisfactory models should be forthcoming*. Temporal measurements for time-scales of interest must be made from fixed platforms (such as the earth, balloons, and possibly, the shuttle) using inferential data such as radar returns or optical measurements. Such optical measurements can be made at wavelengths other than those of current system interest. Incoherent radar returns can also yield the atmospheric temperature that is a crucial parameter in the prediction of the infrared radiance.

For naturally disturbed atmospheric conditions, such as an aurora, coordinated measurements are available and more are being planned. These measurements involve both data on the energy input and the resulting radiation, as well as measurements that can be used to infer local conditions, such as electron densities, within the radiation source region. In Chapter 5 a method of using some of these data to predict the spatial and temporal dependence of the limb radiance at 2.7 and 4.3 μm is discussed.

This summary and recommendations of possible measurements must be recognized as being based on incomplete information. As new measurements are made and their results added to our knowledge of atmospheric radiances, new routes of investigation may be discovered.